Design Optimization for Active Twist Rotor Blades

by

Ji Won Mok

A dissertation submitted in partial fulfillment
of the requirements for the degree of
Doctor of Philosophy
(Aerospace Engineering)
in The University of Michigan
2010

Doctoral Committee:

Professor Carlos E. S. Cesnik, Chair
Associate Professor Bodgan I. Epureanu
Professor Peretz P. Friedmann
Professor Wei Shyy

Every story has an end.

To my family

ACKNOWLEDGMENTS

The completion of the dissertation has been a long journey. When a new graduate student comes, one of the advices that I give is that "Life goes on, though you are a graduate student, and it might not be a short one." Yes, mine also didn't stand still, and prolonged way longer than expected. Much happened and changed. I knew that many have questioned whether I would finish my dissertation. I, also, barring losing confidence so many times I've lost count, getting writer's block just as many times, take time-off, start new program, beginning/ending relationship, getting sick, moving, computers crashing, work as much as possible and pure frustration. I even doubted myself and almost gave up, but was not able to run away because of all the support and encouragement I was given. I just had to do it. Now, I have to confess that it was the people around me who made this possible.

First of all, I would like to thank Professor Cesnik for his endless endurance, support and belief through all these years. He was not only a supervisor, but also a mentor, supporter and teacher, indeed. I must be one of the luckiest students who were able to have him as one's supervisor. I cannot imagine myself being here without his guidance and encouragement. There are some times that the word "thank you" would not be enough, and this is the very moment, but I cannot find any better words. I also deeply appreciate the time, dedication and valuable advices from the rest of my thesis committee, Prof. Friedmann, Prof. Shyy and Prof. Epureanu. I would also like to thank Mr. Matthew Wilbur for his technical suggestions and for providing CAMRAD II loads results. Thanks to the staff at the University of Michigan, Margaret Fillion, Denise Phelps, and Dave McLean for their help, support and hugs.

I also like to express my gratitude to our group members in the Active Aeroelasticity and Structures Research Laboratory: Prof. SangJoon Shin, Anish Parikh and Dr. Jorge A. Morillo for their help on this project; Dr. Rafael Palacios, magical angel and big bro, for his help with UM/VABS; Lab siblings, Ruchir Bhatnagar, Smith Thepvongs, and Dr.Weihua Su; Dr. Ajay Raghavan, Dr. Ryan Park, Major Andy Chiang, Dr. Christopher Shearer, Dr. Andy Klesh, Major Wong Kah Mun, Xong Sing Yap, Matthias Wilke, Dr. Satish Chimakurthi, Dr. Ken Salas, and Devesh Kumar.

I am so sorry that it is not possible to list everyone, but I cannot help to mention the friends here in Ann Arbor who shared the up and down times with me, especially HaeJin, Wooseok, HyonCheol, KyungJin, HaeWon, InSang, Jaeung, JinHyung, ChanDeok, JiHyun, YongJun, Minhye, Eunji, ChangKwon and YoungChang. Special thanks to Kit. Also to all the other friends who have never stopped to believe in me though we were not able to share the moments here. Lastly and mostly, I would give all the thanks to my parent who are still taking care of this old little daughter and my cute little brother who is now getting older with me.

Financial support for my graduate studies came in part from the Oliphant, Mr.and Mrs. Milo E., Fellowship. This thesis was supported by NASA Langley Research Center under cooperative agreement NCC1-323 with Mr. Matthew L. Wilbur as technical monitor. This support is greatly appreciated.

This is a quite a memorable moment. There is a saying in Korea that goes like this: “There is no death without an excuse.” I would say, “There is no graduate student without a story.” Now, this story is about to end. There might be another story waiting out there. Anyhow, this story reached:

- The end

LIST OF CONTENTS

LIST OF FIGURES

LIST OF TABLES

LIST OF APPENDICES

ABSTRACT

This dissertation introduces the process of optimizing active twist rotor blades in the presence of embedded anisotropic piezo-composite actuators. Optimum design of active twist blades is a complex task, since it involves a rich design space with tightly coupled design variables. The study presents the development of an optimization framework for active helicopter rotor blade cross-sectional design. This optimization framework allows for exploring a rich and highly nonlinear design space in order to optimize the active twist rotor blades. Different analytical components are combined in the framework: cross-sectional analysis (UM/VABS), an automated mesh generator, a beam solver (DYMORE), a three-dimensional local strain recovery module, and a gradient based optimizer within MATLAB. Through the mathematical optimization problem, the static twist actuation performance of a blade is maximized while satisfying a series of blade constraints. These constraints are associated with locations of the center of gravity and elastic axis, blade mass per unit span, fundamental rotating blade frequencies, and the blade strength based on local three-dimensional strain fields under worst loading conditions.

Through pre-processing, limitations of the proposed process have been studied. When limitations were detected, resolution strategies were proposed. These include mesh overlapping, element distortion, trailing edge tab modeling, electrode modeling and foam implementation of the mesh generator, and the initial point sensibility of the current optimization scheme.

Examples demonstrate the effectiveness of this process. Optimization studies were performed on the NASA/Army/MIT ATR blade case. Even though that design was built and shown significant impact in vibration reduction, the proposed optimization process showed that the design could be improved significantly. The second example, based on a model scale of the AH-64D Apache blade, emphasized the capability of this framework to explore the nonlinear design space of complex planform. Especially for this case, detailed design is carried out to make the actual blade manufacturable. The proposed optimization framework is shown to be an effective tool to design high authority active twist blades to reduce vibration in future helicopter rotor blades.

CHAPTER 1
INTRODUCTION

This chapter offers an introduction to the vibration reduction with actively controlled twist blade, starting with some background and basic concepts for helicopter vibrations. Then the related researches are reviewed; followed by a separate section about the active materials for active twist blades and the Active Twist Rotor (ATR) blade program. Lastly, the scope and the objectives of this dissertation are presented.

1.1 Background

Long before Leonardo Da Vinci drew the concept of a rotorcraft-like machine in 1483 (Figure 1.1), people had been fascinated by the idea of something flying in the manner of a rotorcraft. The ancient Chinese had a hand-spun toy that rose upward when revolved rapidly between hands (Figure 1.2).

Nowadays, the helicopter is used not only in the military but in various civilian fields such as search-and-rescue from hard-to-reach areas, off-shore transportation, medical evacuation, etc. However, it is not as widely used it should. There exist problems in rotorcraft that limit its usage, one of the most important being fuselage vibration. Since each rotor blade is a slender, flexible structure in a high unsteady flow, it undergoes elastic deformation and vibrate even in normal operating conditions. This vibration can affect performance, reliability, noise, fatigue on rotorcraft components and discomfort for passengers and, of course, increases cost.

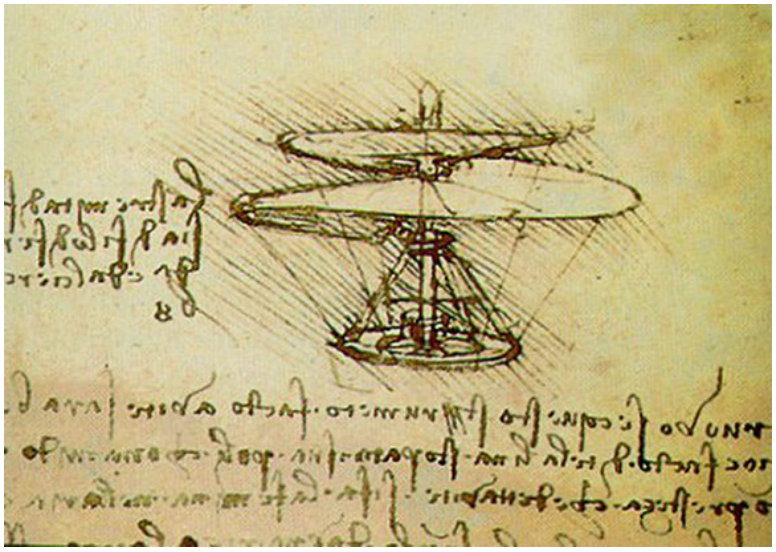

Figure 1.1. Da Vinci's flying machine concept, manuscript B, folio 83 v., Courtesy of Bibliotheca Ambrosia

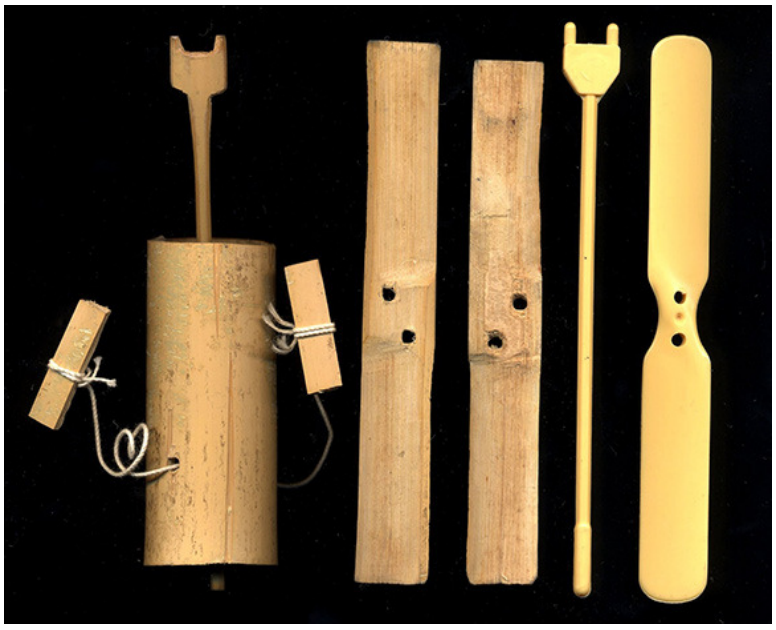

Figure 1.2. Chinese Bamboo Helicopters, circa 400 B.C. (Lemos 2007)

1.2 Helicopter vibration control

The primary source of many of the helicopter's problems is the complex unsteady aerodynamic environment which is generated near the rotor blades, mainly during forward flight (Hooper 1984). The helicopter develops an instantaneous asymmetry of the aerodynamic loads acting on the blades at different azimuth locations as it moves forward, and such asymmetry becomes more and more adverse as the forward-flight speed increases. Figure 1.3 shows a typical aerodynamic environment during forward flight. As a result of the flight velocity that adds differently according to the azimuth angle to the blade rotating speed, a high tip Mach number on the advancing side occurs, and blade stall affects the retreating side. A reverse flow region is also generated, inboard on the retreating side. Aerodynamic environment results in an instantaneous asymmetry of the aerodynamic loads acting among the blades at different azimuthal locations. Due to this, a vibratory response happens on a flexible blade structure, which makes the air loads more asymmetric, and this vibration propagates to the fuselage through the hub.

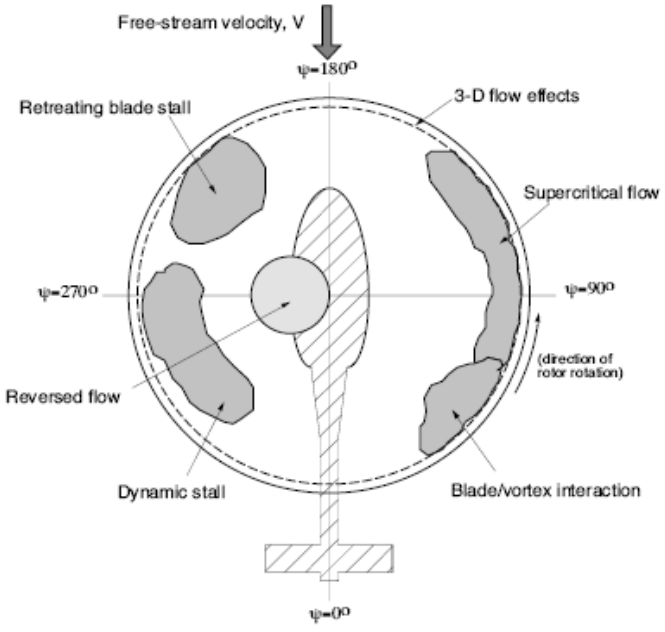

Figure 1.3. Aerodynamic environment in forward flight (Wilkie 1997)

Vibration control has been studied from the very early years of helicopter development. During the mid-1950s, development to reduce the vibration levels in the rotor led to designs that included chord-wise and span-wise placement of concentrated masses, or tuning masses.

The traditional vibration reduction technique was a passive approach, with vibration isolators and absorbers. Later, actively controlled vibration of helicopters emerged. This approach reduces vibrations at their source in the main rotor before they propagate into the fuselage. Higher Harmonic Control (HHC) is an active method implemented at the conventional swashplate in the non-rotating reference frame. The unsteady aerodynamic loads on the blades are redistributed by actively controlling the blade pitch angle at the root. Shaw et al. tested the closed loop control with fixed gain controller, and it showed good performance up to 25% of the desired service life for a full-scale production design (Shaw et al. 1989). An alternative actively controlled vibration approach is the Individual Blade Control (IBC). In this method, each blade is individually controlled in the rotating reference frame. This approach is more general and may overcome the limitations found in HHC with the conventional swashplate. The IBC concept has been implemented in such form as pitch control actuation at the blade root.

Improved from the IBC concept, on-blade control methods emerged. The idea is still controlling the blade individually but the control actuation occurs on each of the blades, instead of the pitch-link at the root. The most popular concepts for that are the active controlled flap (ACF) (Fulton and Ormiston 1998; Milgram and Chopra 1998; Friedmann et al. 2001) and the active twist rotor blades (Rodgers and Hagood 1998; Cesnik et al. 1999), both showing promising characteristics.

For conventional active control technology, the servo hydraulic actuator is commonly used. Unfortunately, it is not suitable ideal for the on-blade control due to the following limitations: multiple energy conversions, large number of parts, high vulnerability of the hydraulic pipe network and the limited frequency bandwidth. Active materials are introduced to overcome these limitations. The advantage of using active materials, particularly piezoelectric

materials, is a direct conversion from electrical to mechanical energy with high-frequency response. Electric energy is easier to transmit, and electric lines are much less vulnerable to damage than hydraulic pipes. Though piezo-electric active materials have large force and energy capabilities, induced strain actuators have a relatively small stroke where the displacement amplification mechanism is needed.

1.3 On-blade actuation concepts

The development of active twist rotor blades incorporating piezo-ceramic materials in order to enable an individual twist deformation of the rotor blades started in the early 1990s. The first attempt at designing active twist blades was presented by Barrett in his master thesis (Barrett 1990) using directionally placed piezo-electric crystals (Figure 1.4). Chen and Chopra updated this idea to introduce strain directly by embedding thin monolithic piezoelectric actuators under the fiber-glass skin of the blade as in Figure 1.5. They suggested to apply the strain at a 45° angle with respect to the blade axis for maximum actuation (Chen and Chopra 1996).

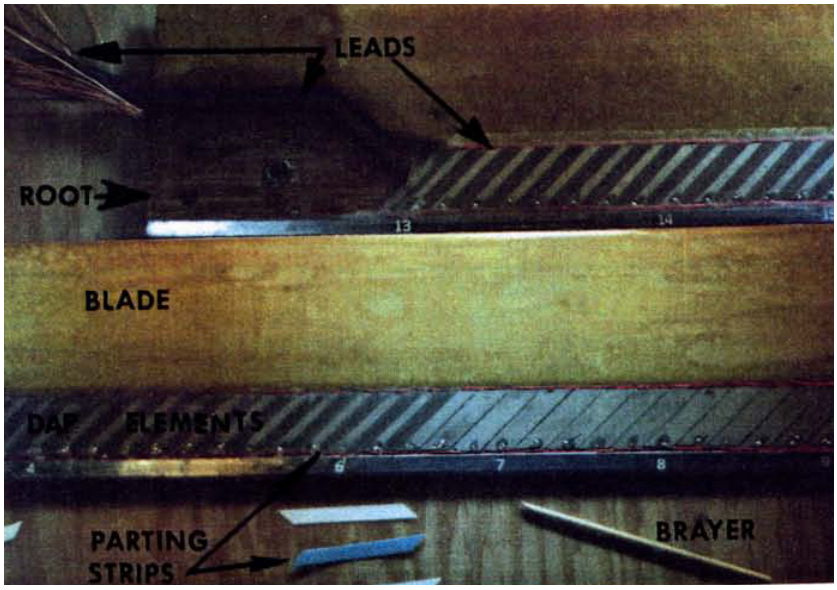

Figure 1.4. Arrangement of Directionally Attached Piezo-electic (DAP) actuator element on the blade prior to fiberglass application (Barrett 1990)

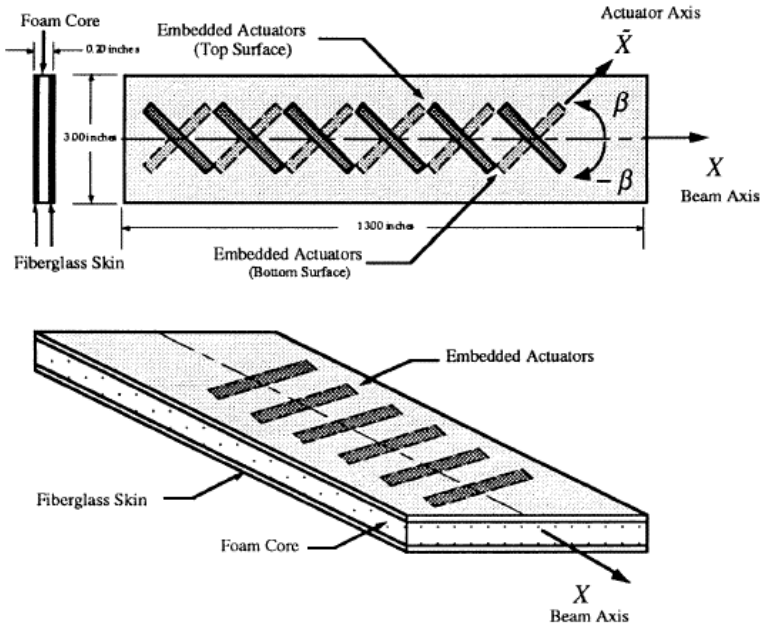

Figure 1.5. A beam specimen with embedded actuators (Chen and Chopra 1996)

In 1997, the NASA/Army/MIT ATR Program for the active twist rotor (ATR) blade started. The program focused on experimental and numerical demonstration of significant vibration reduction in a scaled rotor system using active fiber composite (AFC) composite in the active blades. Besides vibration, the study focused also on developing new analysis capabilities as well as closed-loop control, basic noise reduction capability, and blade tracking improvements. There was great improvement on understanding of the mechanism of the internal actuation, design of ATR systems, its potentials and limitation. As a follow on to it, the Advanced Active Twist Rotor (AATR) Program was launched in 2003, again led by the US Army VTD, carried by the University of Michigan and NASA Langley Research Center. In this program, the optimization of the ATR design would be pursed, including a more realistic reference blade and advanced blade properties with enhanced macro fiber composite (MFC) materials. Vibration and noise reduction would be pursed simultaneously. These programs are described in detail in Chapter 1.6.

In the United States, besides the ATR Program, another notable program called The Smart Rotor Project by the Defense Advanced Research Projects Agency (DARPA) addressed the active twist concept. This project was under the Smart Material and Structural Demonstration

Program (Sanders 2004), the second phase of the DARPA program which initiated in 1993 after DARPA realized the importance and impact of smart material technology in aerospace systems. The Boeing/MIT team introduced two concepts. One was the concept to use the trailing edge flap to induce the blade twist, and the other was to use embedded piezoelectric composite to twist the blade directly. They implemented these concepts on 1/6th Mach scale model of CH47D Chinook blade (Rodgers 1999; Prechtl 2000).

Other research groups are doing different research related to the active blade control. The Pennsylvania State University team suggested that the induced shear piezoelectric tube actuator, which is the torsional PZT actuator for ATR blades, to be used to twist the blades (Centolanza 2002). Prahlad and Chopra developed the methodology to model and explore the torsional actuator with shape memory alloy (SMA) actuators (Prahlad and Chopra 2007).

One of the most extensively explored approaches in this research area is the actively controlled flap (ACF). Friedmann and Millott demonstrated the potential of AFC for vibration reduction in helicopters in forward flight (Millott and Friedmann. 1994; Friedmann and Millott 1995). The ACF implements small partial-span trailing-edge flap either in the single flap or dual-flap configuration, as shown in Figure 1.6. Fulton and Ormiston presented the experimental results on the practical implementation of the ACF and its application to fundamental vibration reduction in the open-loop mode, on a two-bladed rotor. These results enabled to compare the simulation to the obtained experimental data (Fulton and Ormiston 1998). Through the papers about practical implantation of AFC, important problem has been noticed that the maximum flap deflections can reach 15 deg, which is larger than angles that can be achieved with active or smart materials-based actuation. In addition, practically the flap authority will have to be limited to 3–4 deg to avoid interfering with the handling qualities of the helicopter. Cribbs and Friedmann proposed new control method with limited flap deflections, 4 deg. This method showed that a hub vibration reduced as similar to the ones without limiting the flap deflections (Cribbs and Friedmann 2001). Additional studies on the single and dual ACF systems have been conducted. As expected, the dual-flap configuration showed better effectiveness in alleviating the vibration than the single-flap configuration (Depailler and Friedmann 2002). Milgram and Chopra performed the

parametric studies on vibration reduction using actively controlled flaps and showed that the flap system significantly reduced the fixed system 4/rev hub loads (Milgram and Chopra 1998).

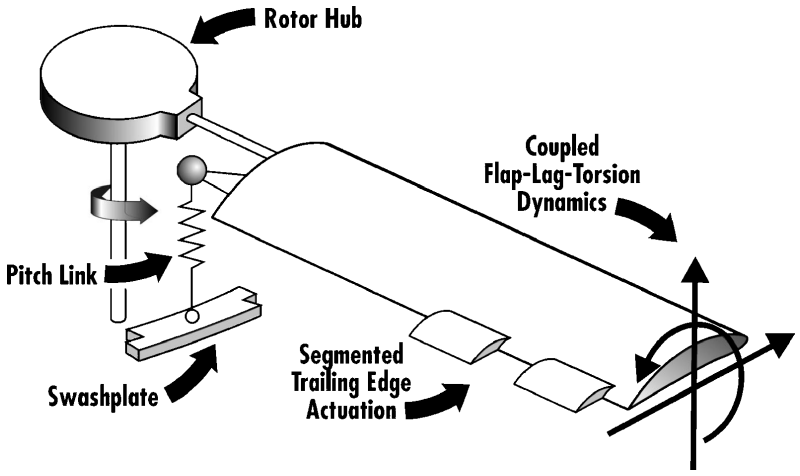

Figure 1.6. Single- or dual-ACF configuration used for vibration reduction (Friedmann 2004)

Meanwhile, from 1994 to 2001, the Japanese government agencies conducted experiments on the active flap using an electromagnetic actuator. The Japan Aerospace Exploration Agency (JAXA) has presented the effectiveness of the active flap control on BVI (Blade Vortex Interaction) noise reduction (Aoyama et al. 2006). They presented the evidence that the active flap control is as effective as IBC with a small control area, which is only 4.5% of IBC.

In Europe, DLR (German Aerospace Center) and ONERA (French National Aerospace Research Center) have also been jointly pursuing a similar project (Philippe 2003). They investigated the active flaps and active twist rotors and presented the potentials of each. Brockmann and Lammering in Germany developed a three-dimensional beam finite element for further investigation with anisotropic actuation in the rotating beam (Brockmann and Lammering 2006). DLR developed a detailed structural model on the basis of the BO105 model rotor blade, to predict the performance with respect to rotor-dynamics, stability, aerodynamics and acoustics. These rotor dynamic simulations showed a noise reduction of 3

dB for an active twist of 0.8° at the blade tip, and a power reduction of 2.3% at 87m/s with respect to the BO105 baseline rotor. Then a demonstrator blade with a rotor radius of 2m was designed and manufactured (Wierach et al. 2005). DLR also presented the evidence that the active twist blades with MFCs can generate sufficient twist deformation under full centrifugal loads at different higher harmonic excitations. It is also shown that the tip twist for the 5/rev and 6/rev excitation can be increased when a segmented actuation is used (Monner et al. 2008). Hoffmann et al. presented two simulation models for active twist by prescribing the twist angle and the twist moment based on the modal shape function, and validated with whirl tower test data. Both models were unable to predict the control frequencies above the first natural frequency in torsion (Hoffmann et al. 2009). Collaborative research has been pursed in Latvia, Italy and Germany under the FRIENDCOPTER (Integration of technologies in support of a passenger and environmentally friendly helicopter) project. They reinforced the known fact that the temperature analogy to model the piezo-electric effect of MFC actuators on the helicopter blade can be used. They focused on the phenomenon that, after the application of electric stress, piezo-fibers are deformed in such a way as if they were exposed to heating or cooling. The vector of coefficients of thermal expansion is then deduced from the piezo-electric deformations (Kovalovs et al. 2007; Glukhikh et al. 2008).

More comprehensive and thorough reviews of trends of the active material actuation for the rotor blade control have been steadily carried out at corresponding periods (Friedmann 1977; Friedmann 1987; Friedmann 1990; Friedmann 1991; Friedmann and Millott 1995; Friedmann 1999; Chopra 2000; Chopra 2002; Friedmann and Hodges 2003; Friedmann 2004; Ganguli 2004).

1.4 Rotor blade design optimization

There is a notable amount of research on helicopter rotor blade design optimization (Friedmann 1991; Celi 1999; Ganguli 2004), although basically none in the area of active twist rotor blades. One of the pioneering works in this field dates back to 1984, when Friedmann and Shanthakumaran (Friedmann and Shanthakumaran 1984) approached the

problem of minimize vibration with aeroelastic stability constraints, where a hingeless rotor blade (based on BO105 blade) cross section was modeled with thin-walled rectangular box sections at each blade station.

When solving an optimization problem, the sensitivity method is one of the most critical aspects for computational cost. The analytical method is efficient but not always applicable to structural optimization, though finite difference scheme is capable of dealing the problems that are not able to be expressed analytically but at computationally higher costs. Lim and Chopra developed a structural optimization analysis of a hingeless helicopter rotor with the objective of reducing oscillatory hub loads in forward flight (Lim and Chopra 1991). They used sensitivity derivatives with a direct analytical approach and it resulted in an 80% reduction in total CPU time required to obtain an optimum solution when compared with a commonly used finite-difference approach. It optimized the design to reduce hub loads by 25-77% for the generic blade, and 30-50% for the box-beam blade relative to the baseline performance. Friedmann and coworkers (Friedmann et al. 1992) developed the optimization capability for aeroelastic tailoring of composite rotor blades. They introduced the sensitivity based on the combination of the partial derivatives (analytical approach) with a finite difference scheme and showed the capability of this semi-analytical approach to reduce the computational time considerably. Pape and Beaumier presented an optimization procedure for helicopter rotor aerodynamic performance in hover condition (Pape and Beaumier 2005). The CONMIN, a gradient-based method that minimizes a function under constraints, is used as a numerical optimizer. This optimizer is then coupled to a 3D Navier–Stokes CFD solver. Validations and applications are presented with different blade shape parameters (twist, chord, sweep and anhedral distribution). Then the efficiency and the robustness of the method are tested for more complex applications.

There were also experimental efforts to support the verification of optimization results. Davis and Wellert (Davis and Wellert 1991) used modal bases optimization to improve aeromechanical stability and rotor vibratory response. The reliability of the optimization criteria has been experimentally validated by comparing experimental results from baseline

and optimized rotors. Young and Tarzanin (Young and Tarzanin 1993) performed a Mach-scaled wind tunnel test to validate a four-bladed low vibration rotor design for two different rotors as above - One for the reference rotor, similar to a scaled Model 360 and for the low vibration rotor designed by analytical optimization procedure. The test showed the 4/rev vertical hub load and moments reduction for the optimized low vibration rotor.The research extended its footage to the optimization on the active blade design. Viswamurthy and Ganguli studied the effect of the multiple active trailing edge flaps for vibration reduction in a helicopter rotor using an optimization approach (Viswamurthy and Ganguli 2004). When only the vibration reduction is considered, the gradient-based optimization example showed that four active trailing edge flaps at the blade tip with at higher harmonic actuations reduced the vibration about 72% in forward flight. By the tradeoff studies between vibration reduction and control deflections for one, two and four active trailing edge flaps, using four trailing edge flaps at the blade tip (outer 20%) was optimal for reducing vibration with low control angle deflections which requires low power. More recently, Glaz et al. (Glaz et al. 2006) showed the effectiveness of surrogate modeling of helicopter vibrations, and the use of the surrogates for optimization of helicopter vibration. Glaz then extended that study to what he calls a "passive/active approach" (Glaz 2008). He demonstrated that the efficient global optimization algorithm showed better performance than the conventional surrogate based optimization techniques for vibration reduction at low speed forward flight. Then Actively Controlled Flap was introduced to further reduce vibration and noise, and enhance performance. This active/passive design showed 68 – 91 % reductions in vibration and a 2.3 - 2.7 dB decrease in the maximum noise level. In Europe, DLR proposed a new concept for individual blade control: the Active Trailing Edge (ATE) which has a similar effect as in trailing edge flaps (Grohmann et al. 2008). Detailed aero-servo-elastic optimization and sensitivity studies have been presented. The aero-servo-elastic optimization of the ATE actuator is based on an evolutionary algorithm. It has been demonstrated that the thickness of piezo-ceramic layers is a key parameter for optimization. They showed similar performance for reduction of vibration as did the previously developed trailing edge servo flap.

1.5 Active materials for active twist rotor blades

The active materials, that are also commonly called smart materials, have one or more

properties that change by a controllable external input, such as stress, temperature, pH (acidity), electric or magnetic fields, and moisture. There are a number of types of active materials, some of which are already commonly used. Shape memory alloy might be the most popular one whose deformation is induced and recovered through temperature changes. Electrorheological (ER) and magnetorheological (MR) materials are fluids, which can experience a dramatic change in their viscosity when in the presence of an electric or magnetic field, respectively. Piezo-electric materials produce a voltage when mechanical stress is applied and vice versa. Since it changes a structural property (stress) by a relatively easily controllable input (electric field), it is a very strong candidate for structural control application. There are basically two types of piezoelectric materials. One is piezo-ceramic (PZT) and the other is piezo-film (PVDF). They are already widely used in practice. For example, inside a microphone, a piezo-film translates the variation of air pressure from sound to electrical signals. PVDF is commonly used as a sensor. It cannot produce significant force but is flexible enough to be placed on curved surfaces. On the other hand, PZT is used as an actuator due to its relatively high strength. In short, PZT has strength without flexibility and PVDF has flexibility without strength.

The active twist rotor blade actuator requires certain characteristics. First, it needs to be flexible enough to be incorporated into the curved shape of the blade. It is also expected to have enough structural integrity to withstand the pressure applied during blade fabrication and the external loads during blade operation. It must have high strain-inducing capabilities in an appropriately applied electric field and anisotropy of the actuation is required so that tailoring in the blade design may be possible. Thus, it can be said that, in an active twist rotor blade, the materials need to be strong like piezoelectric ceramics but also flexible like the film.

To solve this conflict, the active fiber composite (AFC) was developed (Bent et al. 1995). AFC is a conformable anisotropic actuator, which can be integrated into a passive structure. The AFC actuator is made with the inter-digitated electrode poling and piezoelectric fibers embedded in an epoxy matrix. Figure 1.7 shows the lay-out of the AFC actuator. This approach produces a high performance piezoelectric actuator laminate with both strength and

flexibility. Basic material characterization and the concept of an integral twist-actuated rotor blade was investigated during the DARPA/Boeing/MIT integral actuated blade program (Bent and Hagood 1997).

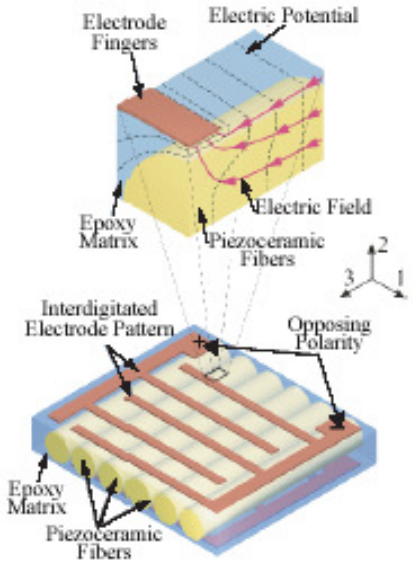

Figure 1.7. Sketch of Active Fiber Composite (Wickramasinghe and Hagood 2004)

More recently, the macro fiber composite (MFC) has been developed at NASA Langley based on the same idea as the AFC, using the piezoelectric fibers under inter-digitated electrodes. It is composed of a rectangular cross-section, with unidirectional piezo-ceramic fibers that are embedded into a thermosetting polymer matrix and sandwiched between Kapton sheets layered with copper inter-digitated electrodes. The fiber sheets are formed from monolithic piezo-ceramic wafers and conventional computer controlled wafer-dicing methods. The fabrication process is shown in Figure 1.8. They suggested adapting to accommodate any piezo-ceramic material, dielectric film, electrode geometry, or matrix adhesive, depending on the intended application, since the manufacturing process was uniform and repeatable. Total cost for the baseline MFC device has proven to be as low as approximately $120 (2000 US dollars) apiece at a "laboratory scale" (Wilkie et al. 2000), and due to the ease of automation of manufacturing process, it can be reduced further by mass production. Tests were performed to present the evidence of the capability and endurance of the MFC. It produced large directional in-plane strains; around 2000με under a 4000V peak-

to-peak applied voltage and endured up to 90 million electrical cycles without any reductions in free-strain performance. Figure 1.9 shows a MFC actuator manufactured at NASA Langley (Wilkie et al. 2000). In short, while the piezo-ceramic fibers in AFC are extruded, the piezoelectric fibers in MFC are manufactured from dicing low-cost monolithic piezo-ceramic wafers. Thus, it retains beneficial features of the AFC with a lower fabrication cost. This actuator was tested for its characteristics (Williams et al. 2004; Williams et al. 2006) and it has been considered for use in many aerospace applications.

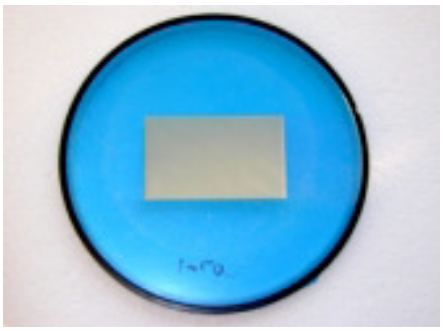

a) 3.375 x 2.25 x 0.007 inch piezoceramic wafer on polymer film

b) Computer-controlled dicing saw used for cutting wafers.

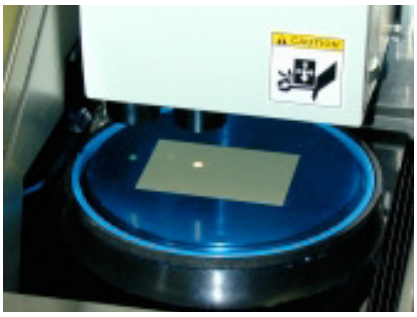

c) Piezo-ceramic wafer and polymer film frame positioning for cutting.

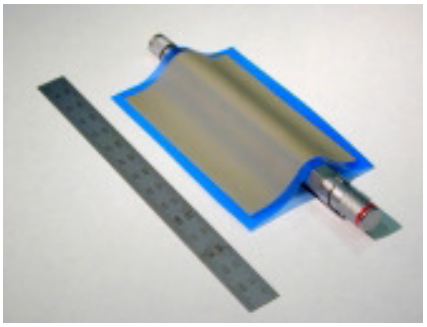

d) Sheet of piezo-ceramic fibers, after cropping from excess polymer film

Figure 1.8. Fabrication of MFC Actuator (Wilkie et al. 2000)

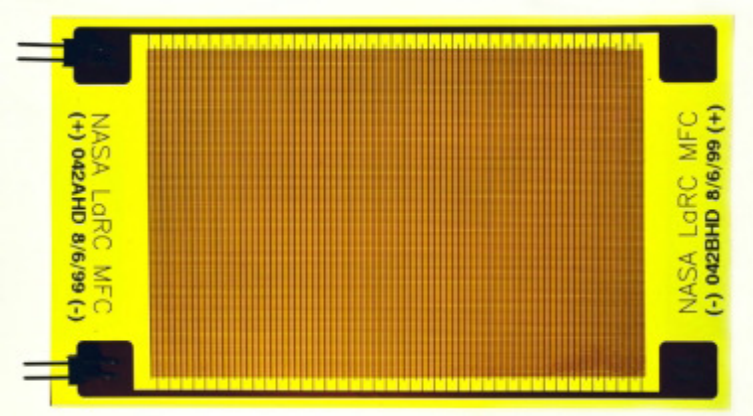

Figure 1.9. MFC Actuator (Wilkie et al. 2000)

1.6 Active twist rotor (ATR) project

In order to reduce high vibration levels, integral twist actuation of the rotor blades has been proposed, which would have several potential benefits over other methodologies. As having the blade using this design maintains a smooth and continuous surface along the blade, so ATR blades do not interfere with aerodynamics as much as other methods. By controlling the twist of each rotor blade individually, local changes to the vibratory loads are induced. This results in a reduction of the vibrations transmitted to the fuselage through the rotor hub. With the development of the AFC, the NASA/Army/MIT active twist rotor program was launched in 1997 (Cesnik et al. 1999). In the ATR program, analysis and design methodologies were developed for active blades with embedded piezo-composite actuators (Cesnik and Shin 2001).

An ATR prototype blade was designed and fabricated for bench/hover testing (Cesnik et al. 1999; Shin and Cesnik 1999; Wilkie et al. 1999; Cesnik et al. 2001). The test-bed for the ATR blade is shown in Figure 1.10, and the final blade is presented in Figure 1.11. Following these studies, a set of active blades was manufactured and wind tunnel tested in forward flight (Wilbur et al. 2002). The open-loop (Wilbur et al. 2001; Wilbur et al. 2001) and closed-loop controls (Bernhard and Wong 2003; Shin et al. 2005) in the forward flight test showed significant authority and was successfully tested in Langley's Transonic Dynamics

Tunnel (Cesnik et al. 1999). The blade design was explored with several design variables based on an existing passive blade. Design variables such as the number of active layers, length of the active region in the chord-wise direction, and the location of the active layers that are inserted in the cross section, were varied. The other blade design parameters were kept in an appropriate range to maintain characteristics similar to the baseline blade. The design that showed the largest static twist actuation was selected for the final design. Different studies also showed numerical and experimental evidence that varying the distribution of passive and active materials in the cross section can improve the blade twist actuation authority (Cesnik and Shin 2001; Cesnik et al. 2003). The basic acoustic feature of ATR on noise reduction also was studied (Booth and Wilbur 2004). Shin continued his work on ATR blades (Shin and Cesnik 2007; Shin et al. 2007; Shin et al. 2008).

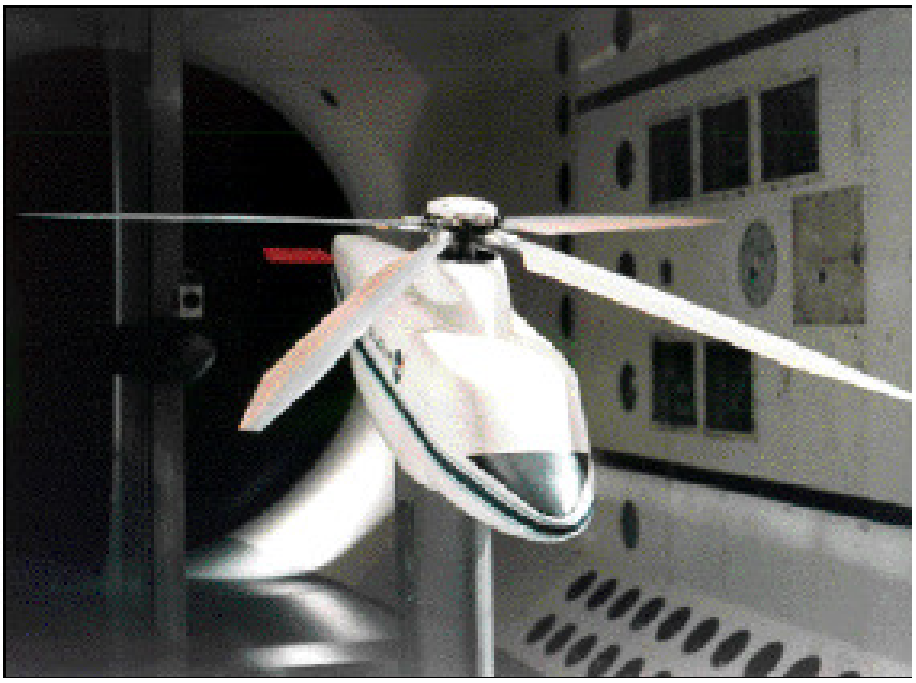

Figure 1.10. Aeroelastic Rotor Experimental System (ARES) testbed in Langley Transonic Dynamics Tunnel (TDT) (Cesnik et al. 1999)

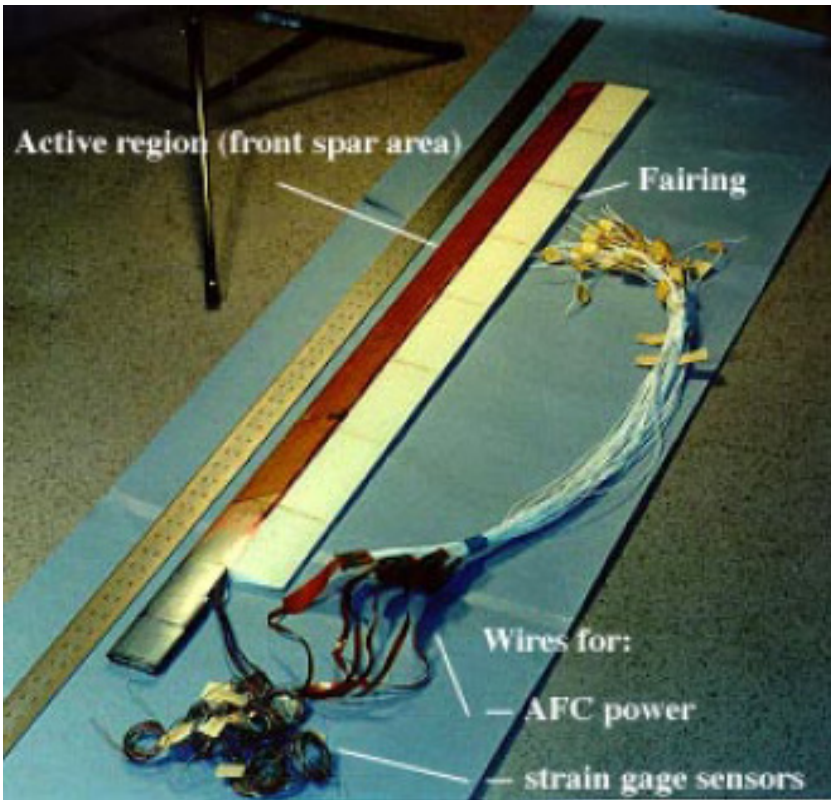

Figure 1.11. Final ATR-I prototype blade (Cesnik et al. 1999)

Encouraged by the results of this first phase, a new phase for the active twist rotor, the Advanced Active Twist Rotor (AATR), was launched with the introduction of MFC in 2003. As mentioned earlier, MFC is similar to AFC with the advantage in manufacturing and corresponding costs. The objective of the original ATR program was to prove the feasibility of an active-twist concept. It used a basic model (a rectangular blade planform with a NACA 0012 airfoil) for which several studies existed. The ATR performance was studied with carefully chosen design variables. In spite of remarkable results, the manual iterative design was not only time consuming but also was unable to guarantee the optimum result. It relied on the designer's understanding and experience of the existing blades. However, due to the complexity of the ATR blade, its performance did not follow conventional expectations, as shown by Cesnik and Shin (Cesnik and Shin 2001).

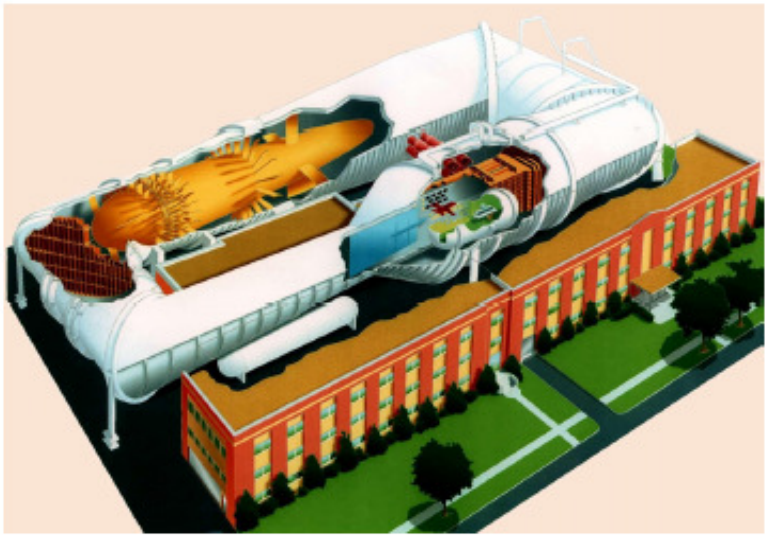

Figure 1.12. The Langley Transonic Dynamics Tunnel

The goal of the AATR design is to exploit current trends in blade design, such as advanced blade tip geometry and high performance airfoils, as well as an optimized structural design, in order to increase active-twist blade response while improving the passive (unactuated) performance of the rotor (Cesnik et al. 2004; Cesnik et al. 2005). Recently, a parametric study for an Advanced ATR was conducted by the U.S. Army Vehicle Technology Directorate at NASA Langley Research Center (Sekula 2005). They performed an analytical study to determine the impact of blade structural properties on active-twist performance. The chosen parameters were blade torsional, flap-wise, and lag-wise stiffness; section mass; torsional inertia; center of gravity; and elastic axis location. The effect of those parameters on rotor power requirements, blade loads, and vibratory hub loads were studied.

1.7 Objectives and orgarnization of this dissertation

As one can see from the discussions presented above, the process to optimize active twist blades is very complex. It adds to the already rich design space of traditional (passive) helicopter blades with tightly coupled design variables and constraints. It seems natural to invoke the principles of mathematical optimization to enable a reliable way to explore the design space. This dissertation has the objective to develop an optimization design framework for active twist helicopter blades with anisotropic piezo-composite materials (e.g.,

AFC and/or MFC) embedded in the composite construction for twist actuation. This framework needs to incorporate appropriate analyses tools into an effective optimizer while ensuring the required data flow among those tools. This is also to be done in a way to achieve low computational expense and stable optimization process. Finally, this dissertation will explore different ATR designs and their dependency on design parameters/variables to better understand the drivers for high-authority active twist blades. This is done through the numerical exploration of the large and complex design space which can take one much further than the manual iterative design approach followed up to now.

This dissertation is structured so that Chapter II introduces the new framework to optimize the design of active twist rotor blades with embedded active actuators. The mathematical statement of the optimization problem is presented and the descriptions for each component of the framework followed in detail. Chapter III presents numerical studies using the proposed optimization approach on active twist blades. The first part of that chapter demonstrates the capabilities of this optimization framework with the NASA/Army/MIT ATR blade. The optimization cases based on this blade are performed with different sets of design variables and constraints. Then a more realistic problem based on a model-scale blade of the AH-64D Apache helicopter is used to show further capabilities of the proposed optimization framework. Prior to perform the optimization, further capabilities and limitations of the code are studied and addressed. Then the optimization cases with different constraints and different set of design variables are performed and the results are studied in detail. One of the designs is selected and refined for later manufacturing. In Chapter IV, the main contributions of this thesis are summarized and future possible directions of research are suggested.

CHAPTER 2
FRAMEWORK AND METHODOLOGY OF ATR OPTIMIZATION

This chapter introduces the proposed framework to optimize the design of an active twist rotor blade with embedded piezo-composite actuators. The chapter begins with the mathematical statement of the optimization problem. Then the proposed framework for ATR optimization is shown with a flowchart. The descriptions for each component of the framework follow.

2.1 Optimization problem setup

The optimum blade design can be obtained by adjusting the design variables within the physical or design required constraints. These variables and constraints are discussed in detail below.

Mathematically, an optimization problem generally is stated as follows: Extremize the desirable objective function *f*, according to the set of design variables *x* within certain limits, while satisfying nonlinear constraints *g*. That is,

$$max\, f(x) \tag{2.1}$$

subject to:

$$g(x) \le 0 \tag{2.2}$$

$$x_l \le x \le x_u . \tag{2.3}$$

where x_l is the lower limit and xu the upper limit of the set x. For the ATR blade optimization, the objective function *f* is the active twist induced by the embedded actuators. Even though the vibration reduction is not directly connected or linearly dependent to the

twist actuation authority, it is known that vibration level reduces in proportion to the increase of the twist actuation authority in the reasonable range.

The main design variables introduced in this optimization problem are:

- The thickness and lamination angle of each ply in the cross-section layup. The material properties used in each ply, however, must be chosen in advance;
- The starting and ending locations of the active region along the cross-section;
- The chord-wise location of the spar (web) wall;
- The length of the spar web extensions;
- Two discrete ballast weights with their masses and chord-wise locations;

These variables may be introduced at different blade radii, and they may be linked within a given span-wise region or among different regions of the blade. In setting up this problem, the blade planform is subdivided into four regions of predetermined length. Each region may have a different airfoil. The most outboard region represents the blade tip, and its cross-sectional layup may be linked with the one from the neighboring inboard region. The blade planform includes pre-twist and tip droop/sweep, in order to model modern helicopter blade configurations. Figure 2.1 shows an illustration of active cross section showing (a) initial layup configuration and (b) some of the design variables.

Due to manufacturing constraints, the chord-wise location of the spar web should be considered a single design variable along the blade radius. If more parameters needed to be linked because of practical manufacturing considerations, they could have been accommodated as well. Finally, the permissible range of each design variable type is also imposed based on practical considerations.

The following set of constraints ($g(x)$) is implemented in the proposed framework:

- Chord-wise location of the cross-sectional center of gravity;
- Chord-wise location of the cross-sectional elastic axis;

- Blade mass per unit span (for correct Lock number);
- Blade fundamental rotating frequencies (for desirable blade dynamics);
- Maximum allowable blade local strain under the worst-case loading condition (associated with the ultimate strength of the constituent materials).

Besides these, additional constraints may be added to better pose the problem and make it more realistic (*see Chapter 3.1*). Also, fatigue life is only considered indirectly by keeping the dynamic strain levels below a practical threshold.

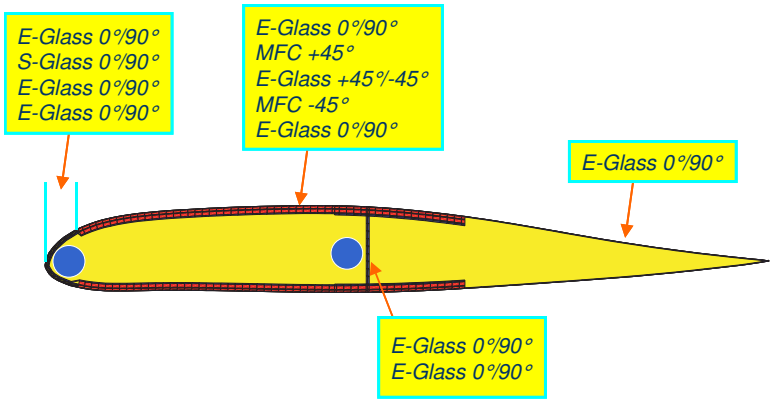

(a)

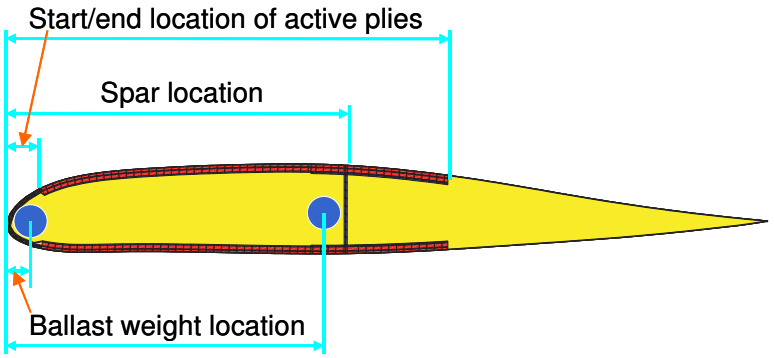

(b)

Figure 2.1. Illustration of active cross section showing
(a) initial layup configuration, and (b) some of its design variables

2.2 Optimization framework

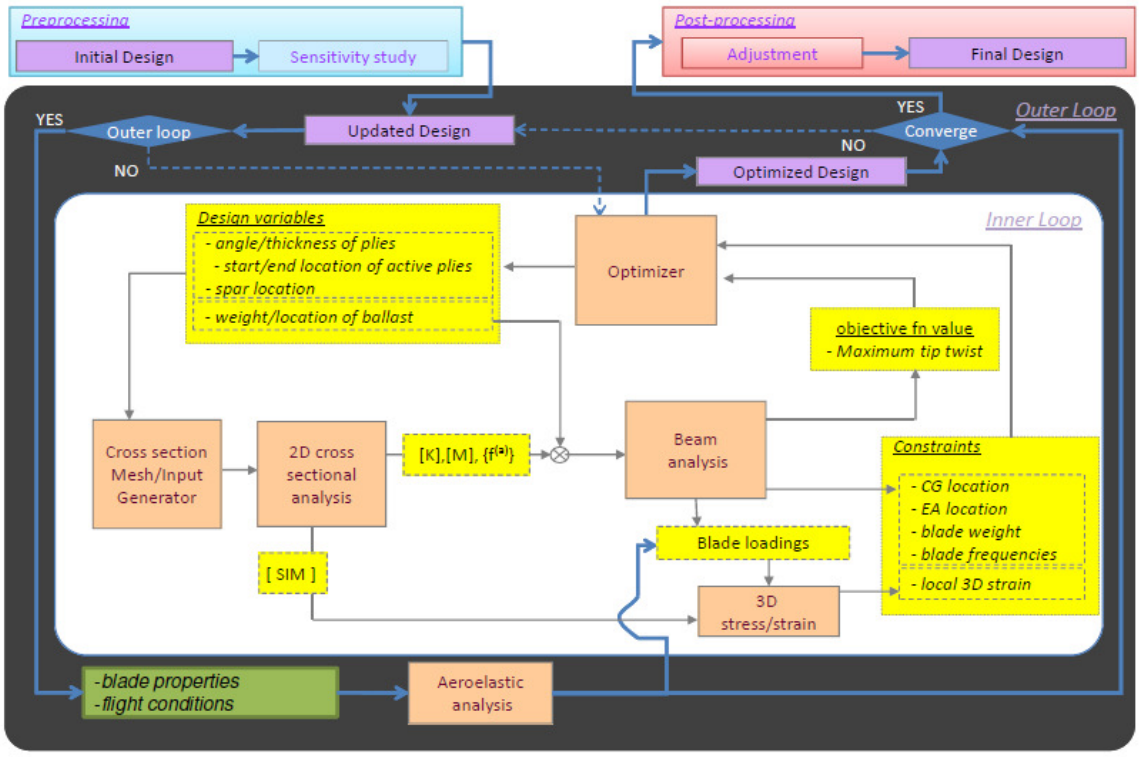

Figure 2.2. Flow chart of the design optimization framework
(light grey area indicates inner loop while deeper shaded area is outer loop)

The proposed optimization framework is schematically described in Figure 2.2. Note that the framework is composed of a two-level nested loop. The aeroelastic analysis is usually computationally expensive and this is a very important factor in numerical optimization. So for the inner loop, the maximum loads (two bending moments, torsion moment, two shear forces, and axial force) for different flight conditions for pre-determined points along the blade radius and azimuthal stations are kept constant. This is based on the assumption that the structural design changes along the optimization process would not have much effect on the worst loads on the blade. The inner loop undergoes several optimization cycles before the design comes to the upper loop. Loads are recalculated and the process resumes until the worst loads converge. Besides the two-nested optimization loops, pre-processing of the model in preparation for the optimization and post-processing/analysis of the optimized design at the very end are also part of the overall design process.

2.2.1 Pre-processing

To insure a smooth start for the optimization process, a reasonable baseline design is expected. This is especially important for the optimization scheme that is adopted in this framework. The baseline does not need to be feasible, but the constraints should not be strongly violated. This can be achieved by using an initial design based on an existing blade or previous designer's experience. Also, the optimization framework can be used to guide the design through few multidisciplinary analysis cycles and provide valuable information to the designer to adjust the blade parameter before it goes to the next phase of the process.

The initial set of constraints must be chosen from the available set (see Section 2.1). Some of the design parameters are fixed, including the length of the blade and airfoil type along the blade. Others need to be initialized (e.g., layup stacking sequences along the blades, set of materials) and may be varied during the optimization (e.g., ply angles, ply thicknesses, spar web location, etc.).

Before the optimization process actually starts, potential problems are addressed in this phase of the framework so to increase the likelihood of a smooth optimization run. The limitation and the sensitivity of the solution are explored including, but not limited to, the quality of the mesh used for every cross section sampled along the blade radius (particularly due to mesh robustness when ply thickness becomes too small), the range of ply angles and materials used as part of the seed laminate, sensitivity and robustness of the optimization scheme on initial condition, etc.

2.2.2 Outer loop

As mentioned above, the aeroelastic load analysis is being brought out from the detail laminate optimization (inner loop) cycle. Based on the initial (baseline) design, sets of loads are calculated associated with different flight conditions (advance ratio, altitude, maneuvers). These loads are represented in the form of rotating blade loads: two bending moments,

torsional moment, two shear forces, and the axial force, and they are typically given at several blade radial stations and azimuthal positions. From all these load cases, for a given blade station a critical load component is identified by scanning all azimuthal angles. At that point, along with the critical load component, all the remaining components of the load case are kept to form an entry on the critical loading set. This is done for all six load components at a given radial station and then repeated for all radial positions along the blade and for all flight conditions being considered. The critical loading set is then passed to the inner loop for structural sizing. Once the inner loop optimization cycle is completed, a new set of blade parameters are received by the outer loop from which new aeroelastic load analyses are performed. This process continues until the blade design and critical load set converge, at which point the design is considered ready for the post-processing phase. This separation of the aeroelastic analysis from the structural optimization process (inner loop), reduces the computational cost remarkably without affecting the structural design significantly. In this dissertation, the aeroelastic load analysis was performed using CAMRAD II by NASA Langley.

2.2.3 Inner loop

(1) Optimization scheme

The inner loop optimization code is developed on the MATLAB planform, due to its capability of adopting/combining other codes and easy of use. Moreover, MATLAB provides optimization solutions in its framework. and "fmincon" was chosen from its optimization toolbox. The "fmincon" function minimizes a constrained nonlinear multivariable problem. A gradient-based constrained optimization scheme is desirable due to its flexibility to deal with large, nonlinear problems. The "medium scale" option is used, which is associated with a sequential quadratic programming method. For each iteration, the function solves a quadratic programming sub-problem, which improves convergence (Hafka and Gurdal 1992). The gradients of the objective function and the constraints are provided from finite differentiation (implemented in the framework). The BFGS (Broyden-Fletcher-Goldfarb-Shanno) method (Fletcher and Powell 1963), a well-known quasi-Newtonian algorithm for unconstrained optimization, is applied to this method. Three kinds of termination criteria

have been used: maximum number of iterations, tolerance on the design variables, and tolerance on the objective function value. When one of these termination criteria is satisfied, the optimization loop will end. In case the result indicates that the solution still needs further iterations, with different constraints, the optimization can be restarted from the point where it stopped previously. This restart feature enables using the history of prior optimization and reduces the computational cost.

Since the objective function of this problem is highly nonlinear, and since the design hyperspace is very complex, it is possible for "fmincon" to fall into a local extremum, leading to a sub-optimal solution. Therefore, it is necessary to run the optimization to completion, starting from different initial points. Furthermore, when the problem is infeasible, "fmincon" attempts to reduce the distance to the most violated constraint boundary. To simplify this step and add robustness to the procedure, it is recommended to start with a feasible initial point if possible.

(2) **2-D Cross sectional analysis**

UM/VABS (Cesnik and Palacios 2003) is a finite-element based analysis of active cross sections with arbitrary geometry and material distributions. UM/VABS (University of Michigan–Variational-Asymptotic Beam Section analysis) can compute the cross-sectional elastic, inertial, thermal, and electric characteristics of active anisotropic beams of arbitrary cross-sectional shape, including the effects of initial twist and curvature. In this optimization process, UM/VABS provides cross-sectional stiffness, inertia and actuation forces/moments values to be used in the one-dimensional (beam) modeling of the blade. It also calculates the locations of the center of gravity and elastic axis, the blade mass per unit span, and the static active twist rate (in a given cross section). UM/VABS input has a NASTRAN-based format. It also has a Timoshenko-like beam option and this gives the 6×6 stiffness matrix as output based on extension, transverse shear in two directions, twist, and bending curvature in two directions, accordingly. The 6×6 inertia matrix is based on 3 displacements and 3 rotations. Further explanation and mathematical background can be found in (Palacios Nieto 2005).

Since UM/VABS would be included in the optimization process, it is crucial to have an

automated mesh generator that can take a few parametric inputs and generate the needed mesh. This is accomplished with a MATLAB-based mesh generator specially developed for UM/VABS. To create a general airfoil wetted surface, pairs of coordinate points defining the contour of the airfoil must be supplied. Contour equations have been implemented for the NACA four- and five-digit series airfoils. Otherwise, the contour can be supplied from a lookup table. From the wetted surface, layers of given (composite) material are defined in order to create the stacking sequence needed for the internal structural configuration.

Materials are defined for every passive and active layer. Using a look-up table, their properties are loaded for each layer. Although UM/VABS can deal with any type of internal cross-sectional geometry, the mesh generator is limited to modeling walls and webs only (no foam or honeycomb filling, for example). The inertial effects associated with the ballast masses are added directly to the inertia matrix generated in UM/VABS:

Mass moment of inertia matrix is defined as follows.

$$\mathrm{M} = \begin{bmatrix} \overline{m} & -\overline{m\tilde{\xi}} \\ \overline{m\tilde{\xi}} & \bar{i} \end{bmatrix} \tag{2.4}$$

When implement the effect of the ballast weight Mp to the mass matrix, it should be considered that the output reference axes is parallel to the principal area axes in the UM/VABS setup for the Timoshenko-like model where the shear effects estimated using linear finite-section modes. α represents the output reference axis angle with respect to the original axis; β_p , Point mass location angle with respect to the original axis which is $\tan^{-1}(P^o_{x3} / P^o_{x2})$; and θ_p, the point mass location angle with respect to the output axis which is $(\beta_p - \alpha)$.

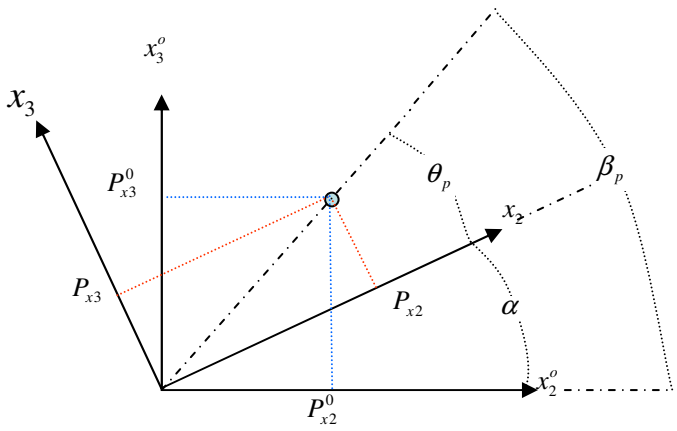

Figure 2.3. Point mass with respect to the original and the output axes

(P_{x2}^o, P_{x3}^o) is the point mass location defined on the original axis $X = [x_1^o, x_2^o, x_3^o]$, while (P_{x2}, P_{x3}) is the point mass location defined on the output axis $X = [x_1, x_2, x_3]$ (Eq.(2.5)).

$$P_{x2} = \sqrt{(P_{x2}^o)^2 + (P_{x3}^o)^2}\cos\theta_p,\ P_{x3} = \sqrt{(P_{x2}^o)^2 + (P_{x3}^o)^2}\sin\theta_p \tag{2.5}$$

The corresponding mass matrix components are as below. The first terms of $\overline{m}, \overline{m\tilde{\xi}}, \bar{i}$ are given by UM/VABS before implementing the ballast weight, while the second terms are the modification due to the ballast weight.

$$\overline{m} = \iint_{A(x_1)} \begin{bmatrix} \rho & 0 & 0 \\ 0 & \rho & 0 \\ 0 & 0 & \rho \end{bmatrix} dx_2 dx_3 + \sum \begin{bmatrix} M_p & 0 & 0 \\ 0 & M_p & 0 \\ 0 & 0 & M_p \end{bmatrix}$$

$$\overline{m\tilde{\xi}} = \iint_{A(x_1)} \begin{bmatrix} 0 & -\rho x_3 & \rho x_2 \\ \rho x_3 & 0 & 0 \\ -\rho x_2 & 0 & 0 \end{bmatrix} dx_2 dx_3 + \sum \begin{bmatrix} 0 & -M_p P_{x3} & M_p P_{x2} \\ M_p P_{x3} & 0 & 0 \\ -M_p P_{x2} & 0 & 0 \end{bmatrix} \tag{2.6}$$

$$\bar{i} = \iint_{A(x_1)} \begin{bmatrix} \rho(x_2^2 + x_3^2) & 0 & 0 \\ 0 & \rho x_3^2 & -\rho x_2 x_3 \\ 0 & -\rho x_2 x_3 & \rho x_2^2 \end{bmatrix} dx_2 dx_3 + \sum \begin{bmatrix} M_p(P_{x2}^2 + P_{x3}^2) & 0 & 0 \\ 0 & M_p(P_{x3})^2 & -M_p P_{x3} P_{x2} \\ 0 & -M_p P_{x3} P_{x2} & M_p(P_{x2})^2 \end{bmatrix}$$

Similarly, the center of gravity is also presented on the output axis.

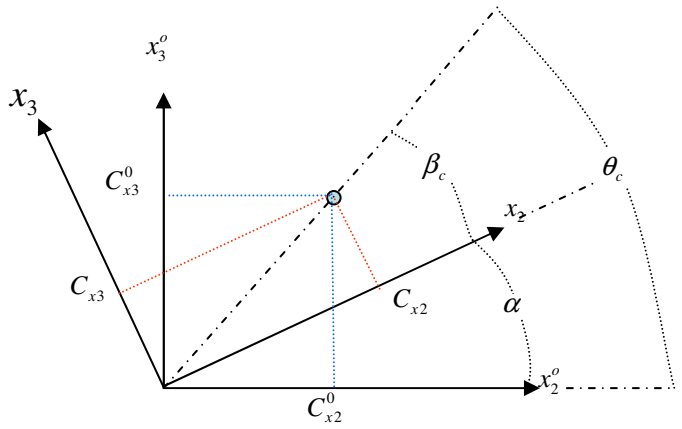

Figure 2.4. Center of gravity with respect to the original and the output axes

α is the output reference axis angle with respect to the original axis; β, the center of gravity angle with respect to the output axis which is $\tan^{-1}(C_{x3}/C_{x2})$; and θ, the center of gravity angle with respect to the original axis axis which is $(\alpha+\beta)$. (C_{x2}, C_{x3}), the center of gravity on the output axis, and (C_{x2}^o, C_{x3}^o), the center of gravity defined on the original axis, are calculated as in Eq.(2.7).

$$
\begin{aligned}
(C_{x2}, C_{x3}) &= \left(\overline{m\tilde{\xi}}_{13}/\overline{m}_{11}, -\overline{m\tilde{\xi}}_{12}/\overline{m}_{11}\right) \\
C_{x2}^o = \sqrt{(C_{x2})^2+(C_{x3})^2}\cos\theta\,&,\; C_{x3}^o = \sqrt{(C_{x2})^2+(C_{x3})^2}\sin\theta
\end{aligned}
\tag{2.7}
$$

Practically, the adjustment of the mass per unit length ($\hat{m}$), the center of gravity ($\hat{x}_{CG}$), and the mass moment of inertia ($\hat{I}_{zz}, \hat{I}_{zz}$) are done as in Eq.(2.8).

$$
\begin{aligned}
\hat{m} &= \overline{m}_{11} + \sum M_p \\
\hat{x}_{CG} &= \frac{(\overline{m\tilde{\xi}}_{13} + \sum M_p (P_{x2}^o \cos\theta + P_{x3}^o \sin\theta))}{(\overline{m}_{11} + \sum M_p)} \\
\hat{I}_{zz} &= \bar{i}_{33} + \sum M_p (P_{x2})^2,\; \hat{I}_{xx} = \bar{i}_{22} + \hat{I}_{zz}
\end{aligned}
\tag{2.8}
$$

It is assumed that the ballast masses do not contribute to the stiffness of the cross section. This is justifiable particularly in the wind tunnel model where the utilization of span-wise segmented insert of tungsten rods results in negligible change in blade stiffness.

(3) 1-D Beam analysis

Another important component of this design framework is the one-dimensional beam analysis. The analysis is conducted in DYMORE (Bauchau 1998), a multi-body dynamics code developed by Bauchau and co-workers (Bauchau 2008). DYMORE solves a geometric exact nonlinear beam problem and provides the blade's natural frequencies during normal rotating conditions. For the span-wise blade stations that correspond to a constant airfoil section, the cross-sectional analysis results obtained from UM/VABS are passed on to DYMORE. The effect of the ballast weights were modeled as point masses. At the short transitional stations between those blade regions, cross-sectional properties are assumed to be linearly varying with blade radius.

Centrifugal loads are considered and calculated in DYMORE and the worst loading case is adjusted accordingly. Though the worst loading case already considered the centrifugal loads, since the mass of the blade and the distribution differs within the optimization process, this approach gives more robustness to the design.

(4) 3-D Stress/strain recovery

At given blade structural properties and loads, internal local 3-D strain and stress fields are computed. In the current implementation, worst-case sectional blade loads associated with flap bending, chord-wise bending, and torsion come from the outer loop. The loading analysis is done by CAMRAD II (Johnson 1992-1997) on the baseline designs. As described above, the centrifugal forces are calculated within DYMORE and combined to the set of those given loads. Although adding them up may be at best a conservative estimate, it tremendously simplifies the design process. These loads can be evaluated off line with DYMORE or another aeroelastic code for an intermediate blade configuration These loads are then used with the strain influence marix (UM/VABS) to recover the composite layer's local three dimensional strain components at every cross-section point everywhere along the blade. The maximum strain criterion is applied for each of the components of the strain and compared to the allowable strains of the local constituent material.

2.2.1 Post-processing

After the optimization is completed, the design may still need to be refined to ensure the blade can be manufactured and/or additional constraints (not taken into account during the optimization) can be accommodated. The following processes were developed for this final phase of design: First, modify the optimized design to be manufacturable. Commercial or off-the-shelf materials are introduced for some components. For example, the ballast masses made of tungsten rod will have specific diameter that is available commercially and must fit within the available volume (without changing blade c.g. location). Detailed modeling is also needed to accommodate current composite manufacturing practices such as ply-drop at the end of the inner layer overlap. Then, based on that modified design, a re-analysis is required to verify the feasibility of the modified design, and final run through the optimization loop may be required to satisfy the constraints and re-evaluate the objective function. Final detail strain analysis is performed for blade integrity, concluding the design.

CHAPTER 3
NUMERICAL EXAMPLES

This chapter presents the numerical studies on ATR blades. First, to demonstrate the capabilities of this optimization framework, the NASA/Army/MIT ATR blade, referred here as ATR-I blade, was chosen as a reference case. The characteristics of this reference blade are presented. The optimization cases of ATR-I show the design can be improved without violating the original constraints. Then a more realistic model based on the AH64 Apache model blade is chosen to show further capabilities of this optimization process. Prior to performing the optimization, further capabilities and limitations of the code are studied. Then the optimization cases with different constraints and different sets of design variables are performed and studied in detail.

3.1 ATR-I blade design

The NASA/Army/MIT ATR blade (ATR-I blade) wind tunnel model has been well studied and characterized over the years, and it has the geometry and non-dimensional characteristics that are representative of a generic production helicopter blade. The original requirements for the ATR-I blade came from an existing passive blade used by NASA Langley. This ATR-I blade was designed to be tested in a heavy gas (R134a) medium. The design employed a total of 24 active fiber composite (AFC) actuators placed on the front D-spar only, and distributed at six stations along the blade span. The ATR-I final design was determined by manual iteration in which parameters were varied in search of maximum static twist actuation. The original ATR-I design was successfully manufactured and tested (Shin et al. 2005), thus it serves as a good reference case for this optimization exercise.

3.1.1 ATR-I baseline characteristics

Figure 3.1 shows the ATR-I blade in planform and its cross section. The airfoil is a NACA 0012 and the material properties of the passive composite pre-pregs and the AFC plies used in the blade are summarized in Table 3.1. As mentioned above, the original requirements for the ATR-I blade came from an existing passive blade and Table 3.2 summarizes the general dimension and shape characteristics of this passive blade. Table 3.3 shows main geometric and structural characteristics of the ATR-I prototype blade.

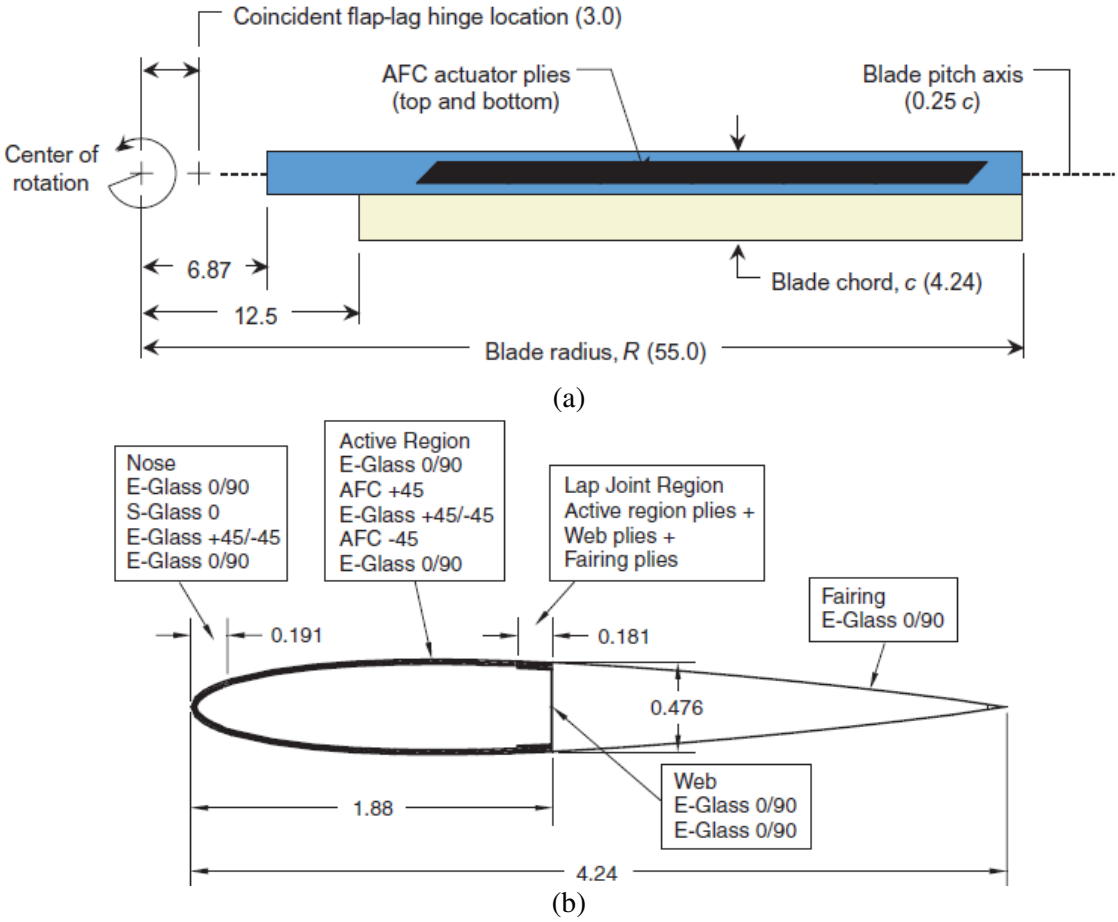

Figure 3.1. (a) Planform and (b) cross section of the NASA/Army/MIT ATR-I blade (unit: inches) (Shin et al. 2000)

Table 3.1. Material properties of the constituents in the ATR-I blades

	E-Glass fabric pre-preg	EA9628 adhesive	Rohacell foam spar	Rohacell foam fairing
Thickness (μm)	114.3	101.6	–	–
Density (kg/m^3)	1716.0	1163.0	75	35
E_L (Gpa)	19.3	2.38	0.0896	0.035
G_{LT} (Gpa)	4.14	0.69	0.0296	0.0138

	S-glass uni-tape pre-preg	Flexible circuit	Front ballast weight (tungsten)	Strain gage wire
Dimension	Thickness (μm) 203.2	Width (mm) 6.604	Diameter (mm) 4.7625	Diameter (mm) 40×0.381
Density (kg/m3)	1799	3044	19100	8900
E_L (Gpa)	48.2	–	–	–
G_{LT} (Gpa)	5.7	–	–	–

Table 3.2. General target requirements for reference blade (considering heavy gas test medium)

Rotor type	Fully articulated
Number of blades, *b*	4
Blade chord, *c*	10.77 cm
Blade radius, *R*	1.397 m
Solidity, *bc/R*	0.0982
Airfoil section	NACA 0012
Blade pretwist	-10° (linear from 0*R* to tip)
Hinge offset	7.62 cm
Root cutout	31.75 cm
Pitch axis	25% chord
Elastic axis	25% chord
Center of gravity	25% chord
Lock number	9.0
1st torsional frequency	0.6
Tip Mach number	< 5/rev
Centrifugal loading at tip	738.5 *g*
Rotor speed	687.5 rpm
Rotor overspeed	756 rpm

Table 3.3. Characteristics of the ATR-I blade

Rotor type	Fully articulated
Number of blades, b	4
Blade chord, c	10.77 cm
Blade radius, R	1.397 m
Solidity, bc/R	0.0982
Airfoil section	NACA 0012
Blade pretwist	-10°
Hinge offset	7.62 cm
Root cutout	31.75 cm
Pitch axis	25% chord
Elastic axis	19.6% chord
Center of gravity	23.2% chord
Lock number	9.0
Tip Mach number	0.6
Centrifugal loading at tip	738.5 g
Rotor speed	687.5 rpm
Rotor overspeed	756 rpm
Mass per unit span (kg/m)	0.710
EA (N)	1.787×10^{6}
GJ (N-m^2)	3.143×10^{1}
EI_{flap} (N-m^2)	4.419×10^{1}
EI_{lag} (N-m^2)	1.153×10^{3}
Section torsional inertia (kg-m2/m)	3.810×10^{-4}
1st torsion frequency @ 687.5 rpm	6.97/rev
Twist actuation @ 0 rpm (deg/m)	1.25

3.1.2 Optimization of ATR-I blade

The ATR-I design depicted in Figure 3.1 is used as a reference design for the first set of case studies using the proposed optimization framework. The twist actuation rate, which is the objective function value, is measured with respect to this reference design.

The following cases show that the original ATR-I design can be improved by optimization and reinforce the need to introduce a numerical optimization when designing active twist rotors.

(1) Blade optimization with similar characteristics from ATR-I baseline case

Case A1

The objective of this case is to determine the internal cross-section configuration of the numerically optimized blade such that its characteristics are very similar to the ATR-I reference blade. The goal is to maximize the twist actuation while keeping the airfoil, ply-thicknesses and ply-angles fixed. The design variables are the start/end of the active regions, the length of the web extension, ballast weights and their locations, and the spar location. These eight design variables and their initial values corresponding to the ATR-I baseline blade are presented in Table 3.5. The constraints in Table 3.4 are set to insure the ATR-I reference blade design is a feasible solution, while allowing the blade parameters some room to adjust. The constraints for the center of gravity and the elastic axis are set to be near 25% chord, to indirectly insure blade aeroelastic stability. Also, it is desirable that the blade's first torsional frequency be lower than 5.0/rev at the nominal rotating condition, a feature found in most modern rotors. For this case, however, it was set to < 8/rev to facilitate obtaining a feasible initial design, whose torsional frequency started at 6.3/rev. The weight of the blade is expected to be similar to the baseline passive blade, and its upper limit was set accordingly. Finally, a safety factor of 1.5 is applied to the most critical design loading case in the strain constraints.

Table 3.4. Constraints and bounds for Case A1

Center of gravity (CG)	$0.2c < CG < 0.28c$
Elastic axis (EA)	$0.17c < EA < 0.25c$
Blade mass / length (kg/m)	$0.656 < m < 0.72$
1^{st} torsional frequency (1T)	1T < 8/rev
Local Strain in the worst loading case	1.5xMax strain < ultimate strength of original constituent material
Ply thickness	$0.5 < t_k < 5.0$
Web extension	$0.05c < web_{ext} < 0.1c$
Active region	$0.0455c < AFC_{loc} < 0.85c$
Spar location	$0.1c < Spar_{loc} < 0.85c$

Table 3.5.Initial values of the design variables for Case A1

Active start	0.0455c
Active end	0.45c
Web extension	0.05c
Ballast weight mass	(0.23, 0.215)
Ballast weight location	(0.027c, 0.432c)
Spar location	00.4438c

The upper plot of Figure 3.2(a) shows the convergence history of the normalized objective function and various normalized blade parameters: locations of the center of gravity and elastic axis, blade mass per unit length, first torsional frequency, and the maximum strain. The objective function is normalized with respect to the ATR-I reference tip twist actuation. The shaded area of the lower plot of Figure 3.2(a) represents the feasible range of these parameters. The convergence history of the spar location, length of the web extension, position of the front and rear ballast weights, and the start/end of the active regions are shown as functions of the chord-wise position in the airfoil in Figure 3.2(b).

In only two iterations the maximum normalized tip twist reaches 1.19, an increase of approximately 20% over the ATR-I reference blade. The start and end chord-wise location of the active region is pushed to its limits. It suggests the need for more active material in the cross section. The elastic axis location, first torsional frequency and the maximum strain are the driving constraints in this case. The spar location is pushed back by approximately 5% to 0.49c and the elastic axis relocates to 0.19c. The resulting length of the web extension is 5% of the chord. The front ballast mass is aligned with the beginning of the active region, while the rear ballast mass ends up in front of the front web extension, near 0.418c, placing the center of gravity at 0.238c. The 1st torsional frequency is at on 6.06/rev near its upper limit. The maximum strain, the in-plane shear strain of the AFC ply, goes to the maximum allowable, 6800 με. These results are summarized in Table 3.6 and compared with the ATR-I baseline blade.

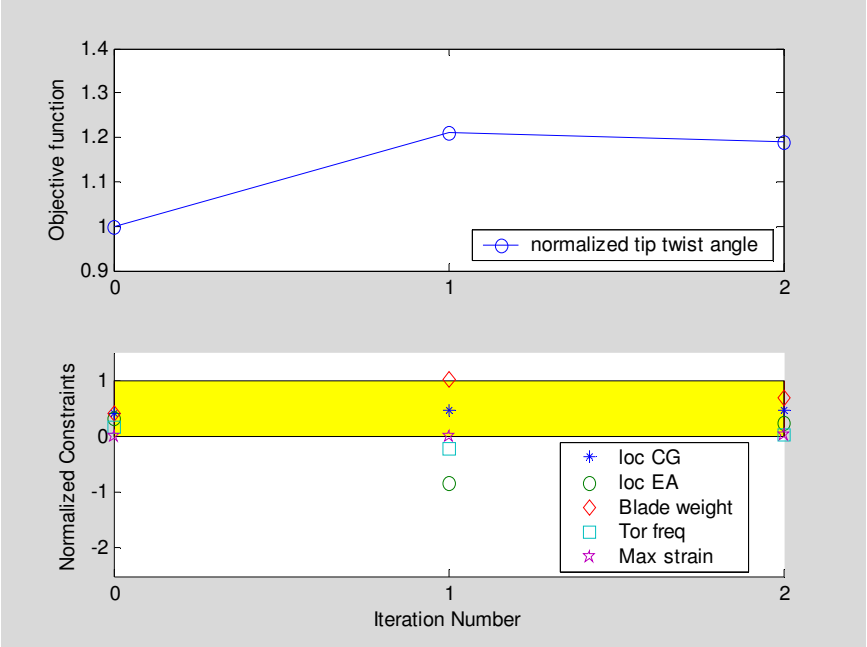

(a)

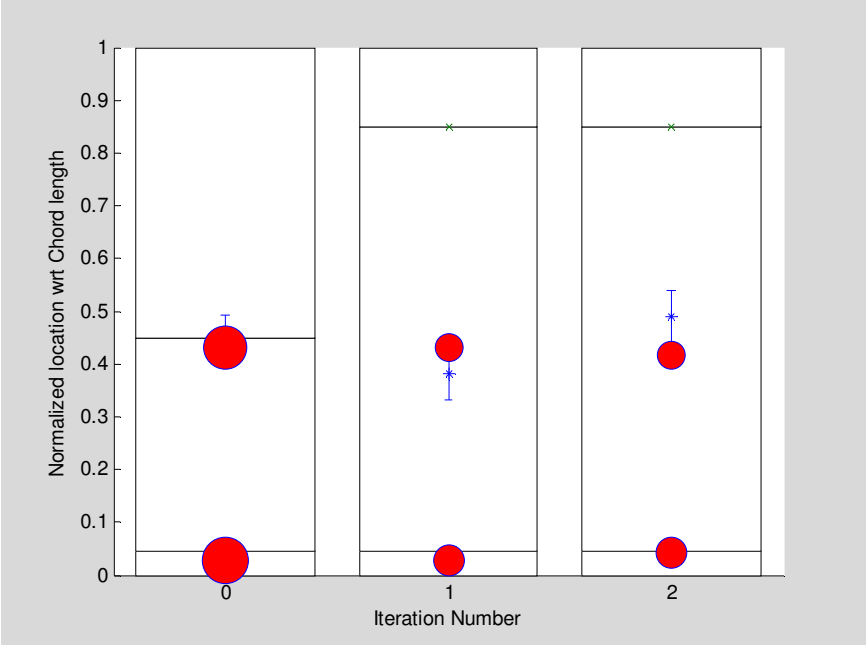

(b)

Figure 3.2. Case A1 Optimization History

(a) Objective function convergence history (top) and normalized blade parameters (bottom), and corresponding (b) spar location (*), web extension (|), front and rear ballast weights (•), and start and end of the active region (- x -), all normalized by chord length. The size of (•) are drawn according to their mass.

Table 3.6. Reference and optimization results for Case A1

	ATR-I baseline blade	Case A1
Active layer properties	AFC	AFC
Normalized tip twist	1	1.19
CG location (%c)	23.20	24.00
EA location (%c)	19.62	19.00
Blade mass/length (kg/m)	0.7103	0.70
1^{st} torsional frequency (1/rev)	6.32	6.06
Strain in 1.5 worst loading case – shear (με)	6327	6732

(2) **Blade optimization to improve characteristics from ATR-I baseline model**

As mentioned in Case A1, the original ATR-I blade design does not satisfy some of the given requirements (see Table 3.2 and Table 3.3). For example, the blade's first torsional frequency should be lower than 5.0/rev at the nominal rotating condition. It was also desired for the ATR-I blade to have both the center of gravity and the elastic axis located at the quarter chord (indirect rotor stability considerations). Thus, a new design is desired that satisfies those constraints while providing a higher twist actuation authority than the baseline case. The following cases were chosen for optimization under different conditions.

Case A2: The same set of design variables as Case A1, for a total of eight variables, but is subject to the constraints defined in Table 3.7. This case is used to analyze the effect the constraint on the elastic axis location has on the optimized design for the cross-section. Therefore, two different sub cases are defined. In Case A2(a) the elastic axis is forced to be located between the leading edge and the quarter cord reference line, similar to Case A1. In Case A2(b), the elastic axis is allowed to move a distance of 0.03c from the quarter cord reference line. This was done to explore the sensitivity of the optimized solution to the initial value for the elastic axis (approxing from the right versus from the left of the targeted 25% chord).

Case A3: A Complete set of possible design variables for a section is used, totaling 29 design variables[1]. The "ply-thickness" used here is actually the multiple of the nominal pre-preg ply-thickness. Although the ply-thickness is a discrete value, which is a multiple of an integer, it is considered a continuous value. Due to the optimization scheme used, all design variables are treated as continuous.

Case A4: Only and all the 12 ply angles constitute the set of design variables. They are angle of plies for outer E-glass, S-glass at nose, 1st AFC on top, 1st AFC on bottom, E-glass between 1st top and bottom AFC plies at nose, 2nd AFC on top, 2nd AFC on bottom, E-glass between 2nd top and bottom AFC plies at nose, web-extension on top, web-extension on bottom, 1st spar-web rib, 2nd spar-web rib .

The new sets of constraints are shown in Table 3.7. Table 3.8 contains the initial values for the different design variables used in each of these cases.

Table 3.7. Constraints for cases with characteristics improved from the ATR-I baseline case

	Case A2(a)	Case A2(b), Case A3 and Case A4
Center of gravity (CG)	$0.2c < CG < 0.28c$	
Elastic axis (EA)	$0.17c < EA < 0.25c$	$0.22c < EA < 0.28c$
Blade mass / length (kg/m)	$0.656 < m < 0.72$	
1st torsional frequency (1T)	1T < 5/rev	
Local Strain in the worst loading case	1.5xMax strain < ultimate strength of original constituent material	
Spar location	$0.1c < Spar_{loc} < 0.85c$	

[1] A given "layer" in the cross section corresponds to a ply of constant thickness (required from a finite-element meshing point of view). Since a "layer" can be made of different materials each having their own ply angle, one may have a larger number of design variables associated with ply angles than with ply thicknesses in a given cross section.

Table 3.8. Initial design values of Case A2, A3 and A4

	Case A2(a), (b)	Case A3	Case A4
All ply-thickness	1.0	1.0	1.0
Ply Angles (degrees)	N/A	N/A	[0 / 0 / +30 / -30 / +45 / -30 / +30 / 0 /0 / 0 / 0 / 0][2]
Active start	0.0456c	0.0456c	0.05c
Active end	0.85c	0.85c	0.85c
Web extension	0.05c	0.05c	0.05c
Ballast weight mass	(0.186, 0.105)	(0.186, 0.105)	(0.1765, 0.0863)
Ballast weight location	(0.022c, 0.85c)	(0.022c, 0.85c)	(0.0c, 0.918c)
Spar location	0.2c, 0.634c	0.634c	0.609c

Case A2

Figure 3.3(a) and Figure 3.4(a) show the convergence history of the normalized objective function and the normalized blade parameters for Case A2(a) with the two different initial values for the spar location of 0.2c and 0.634c, respectively. Similar to Figure 3.2, the shaded area represents the feasible range of these parameters. The only constraint that is not within the feasible range is the location of the elastic axis. The convergence history of the spar location, the length of the web extension, the position of the front and rear ballast weights, and the start/end of the active regions are shown as functions of the chord-wise position in the airfoil in Figure 3.3(b) and Figure 3.4(b), and summarized in Table 3.9. Since the only active constraint violated is the elastic axis location, the spar location is the most effective variable that can be changed in order to place it within the feasible range.

For this Case A2(a), the final location of the spar depends on its initial value. By giving the spar location an initial value (0.20c) close to its lower bound (0.10c), then its final position is

[2] [outer E-glass, S-glass at nose/ 1st AFC on top/ 1st AFC on bottom/ E-glass between 1st top and bottom AFC plies at nose/ 2nd AFC on top/ 2nd AFC on bottom/ E-glass between 2nd top and bottom AFC plies at nose/ web-extension on top/ web-extension on bottom/ 1st spar-web rib/ 2nd spar-web rib]

0.465c; the elastic axis is located on its lower bound, 0.17c, and the first torsional frequency is 4.66/rev. On the other hand, by using an initial value (0.634c) closer to the upper bound (0.85c), the spar location converges to 0.58c with the elastic axis on its upper bound, 0.25c, and the first torsional frequency at 5.0/rev. Similar twist actuation is obtained in both cases. This equivalence is associated with two competing effects. First, the optimizer adds active material in the frontal area of the airfoil section because that gives higher twist actuation per unit of added active material than if the active material is added in the rear. For a given length of the active region, this can be achieved by moving the spar web to the rear. On the other hand, by moving the web to the front, the optimizer is effectively increasing the enclosed area of the rear part of the airfoil, therefore increasing the net induced active twist moment. These two results are the limiting points of these two cases for maximum twist.

Table 3.9 Optimized values for Case A2(a)

Spar location Initial Condition	0.2c	0.634c
Active start	0.0455c	
Active end	0.85c	
Web extension	0.05c	
Ballast masses (kg)	(0.175,0.095)	(0.169,0.096)
Ballast mass location	(0.02c, 0.85c)	
Spar location	0.465c	0.58c
Elastic axis	0.17c	0.25c
Center of gravity	0.28c	0.28c
Torsional Frequency	4.66	5.0
Normalized twist actuation	1.19	1.19
Strain in 1.5 worst loading case – shear (με)	6773	6800

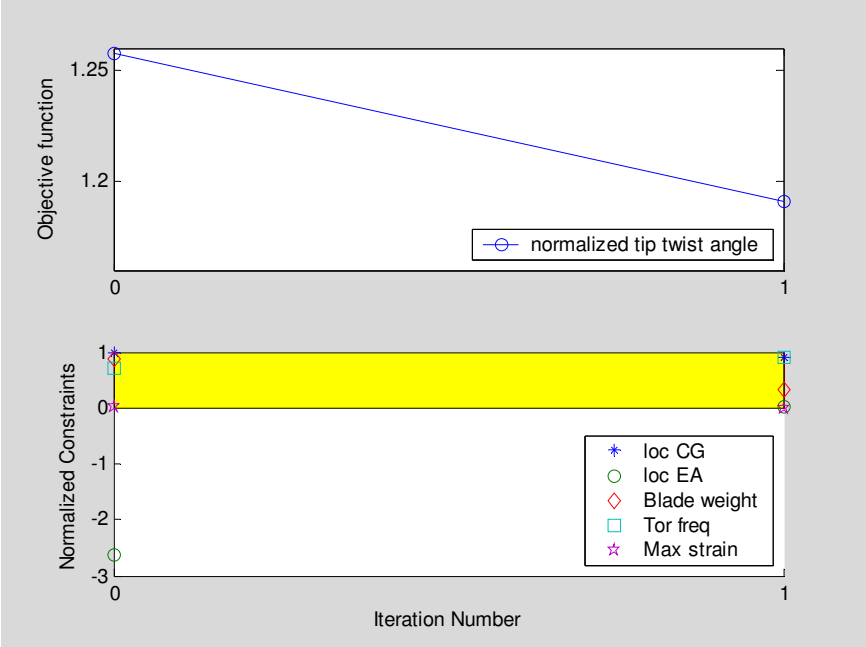

(a)

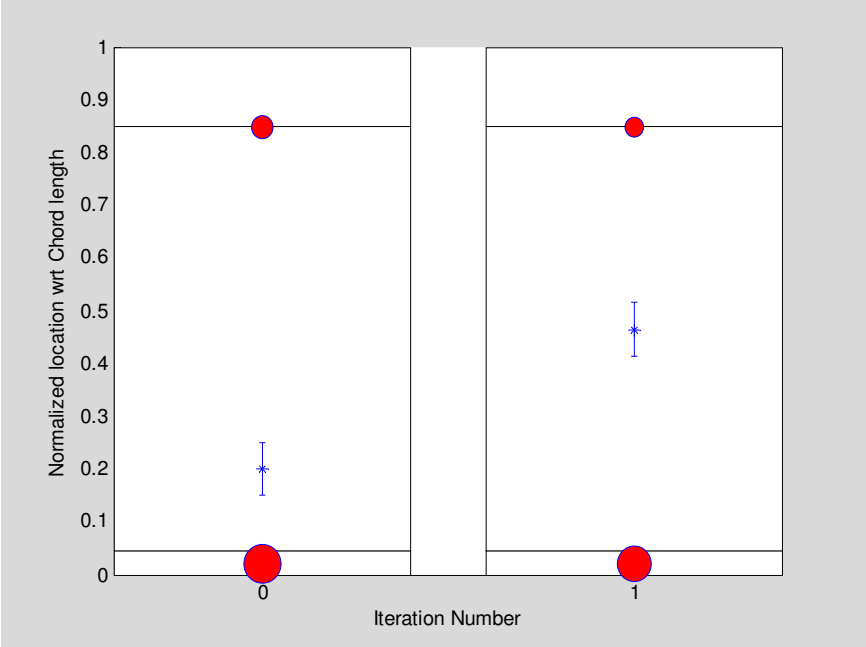

(b)

Figure 3.3. Case A2(a) optimization history for initial spar location at 0.2c.

(a) Objective function convergence history (top) and normalized blade parameters (bottom), and corresponding (b) spar location (*), web extension (|), front and rear ballast weights (•), and start and end of active region (- x -), all normalized by chord length

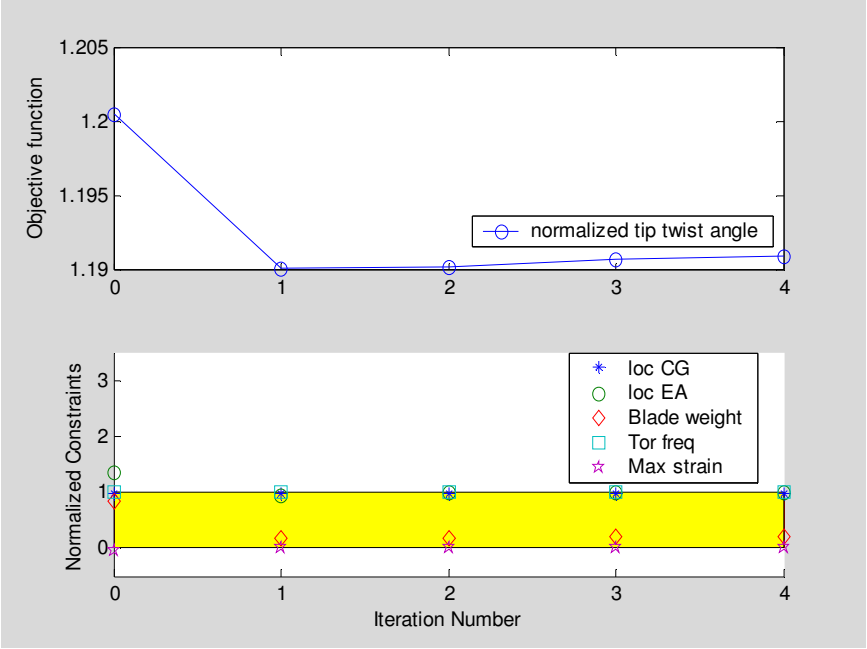

(a)

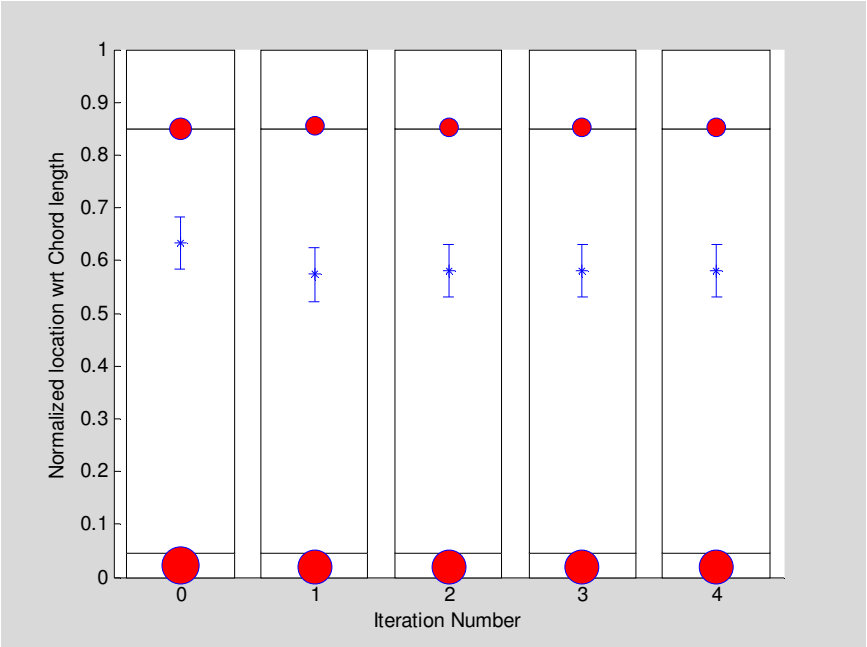

(b)

Figure 3.4. Case A2(a) optimization history for initial spar location at 0.634c.

(a) Objective function convergence history (top) and normalized blade parameters (bottom), and corresponding (b) spar location (*), web extension (|), front and rear ballast weights (•), and start and end of active region (- x -), all normalized by chord length

Figure 3.5 and Figure 3.6 show the result for Case A2(b) with the same initial values for the spar location as in Figure 3.3 and Figure 3.4, respectively. The optimized solution is summarized in Table 3.10. In this Case A2(b), the spar location (0.635c), the location of the elastic axis (0.28c), the torsional frequency (5.0 /rev), and the normalized twist actuation (1.2) are not sensitive to the initial value of the spar location, unlike Case A2(a). The effect of allowing the elastic axis move to the right of the quarter cord reference line is to allow the spar to move further back toward the trailing edge. When comparing the optimized result for Case A2(a) with an initial spar location at 0.634c and the solution for Case A2(b), it is observed that the elastic axis location and torsional frequency have practically the same values. Nevertheless, the twist actuation in Case A2(b) is slightly higher (1%) than in Case A2(a). Moving the spar further toward the trailing edge, increases the amount of active material placed on the front area of the cross-section, therefore an improvement in twist actuation is obtained.

Table 3.10. Optimized values for Case A2(b) for both initial conditions of spar location

Active start	0.0455c
Active end	0.85c
Web extension	0.05c
Ballast masses (kg)	0.163, 0.099
Ballast mass location	0.001c, 0.868c
Spar location	0.635c
Elastic axis	0.28c
Center of gravity	0.28c
Torsional Frequency	5.0
Normalized twist actuation	1.2
Strain in 1.5 worst loading case – shear (με)	6800

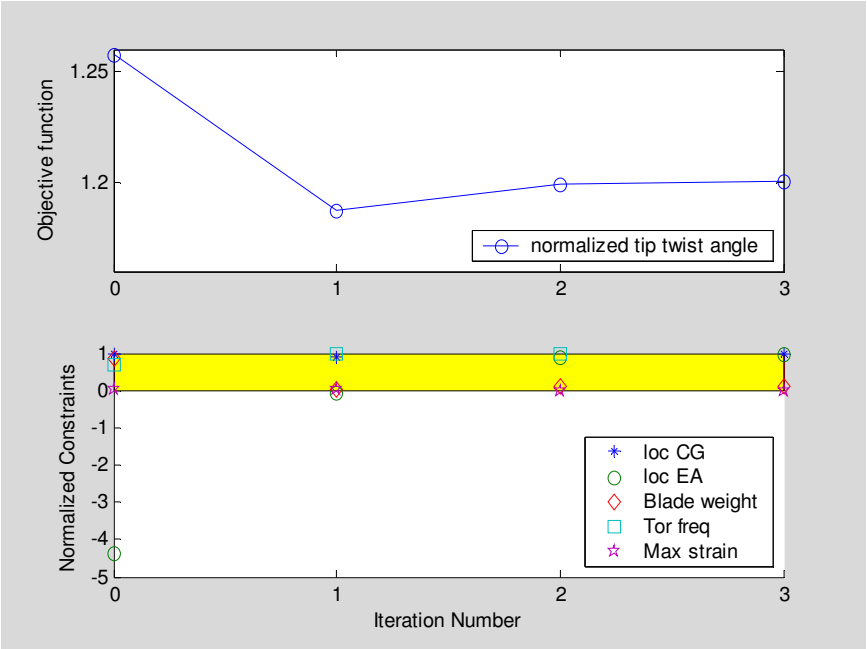

(a)

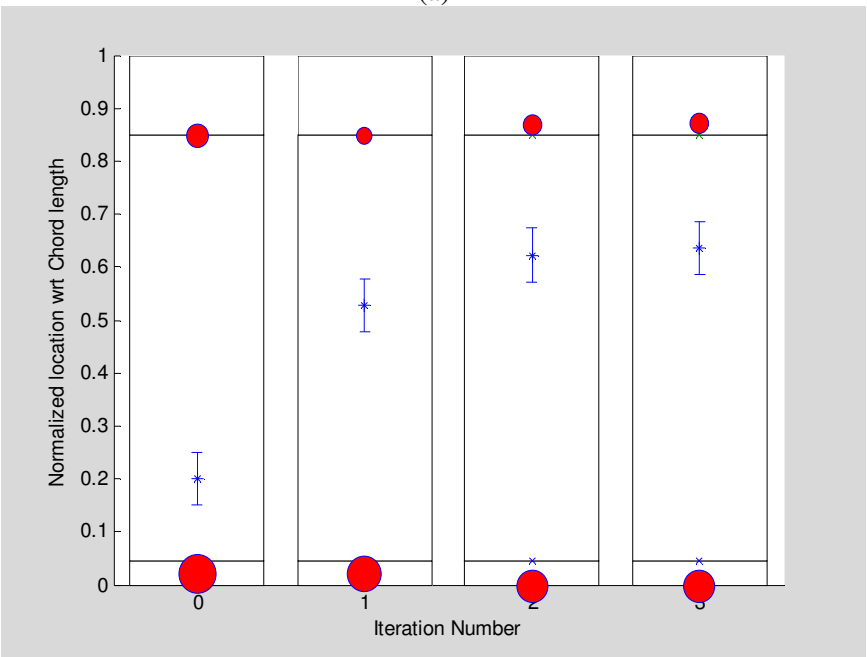

(b)

Figure 3.5. Case A2(b) optimization history for initial spar location at 0.2c.

(a) Objective function convergence history (top) and normalized blade parameters (bottom), and corresponding (b) spar location (*), web extension (|), front and rear ballast weights (•), and start and end of active region (- x -), all normalized by chord length

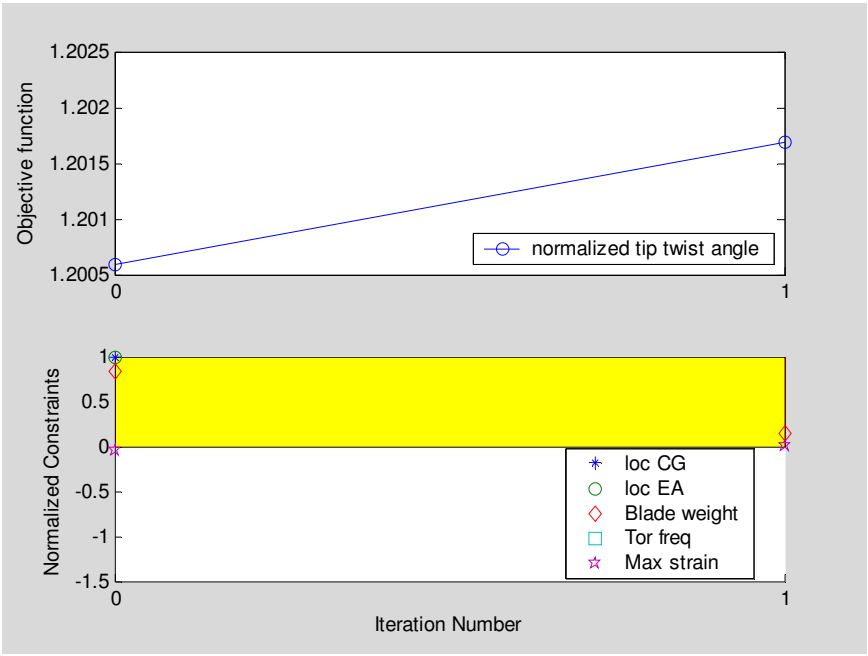

(a)

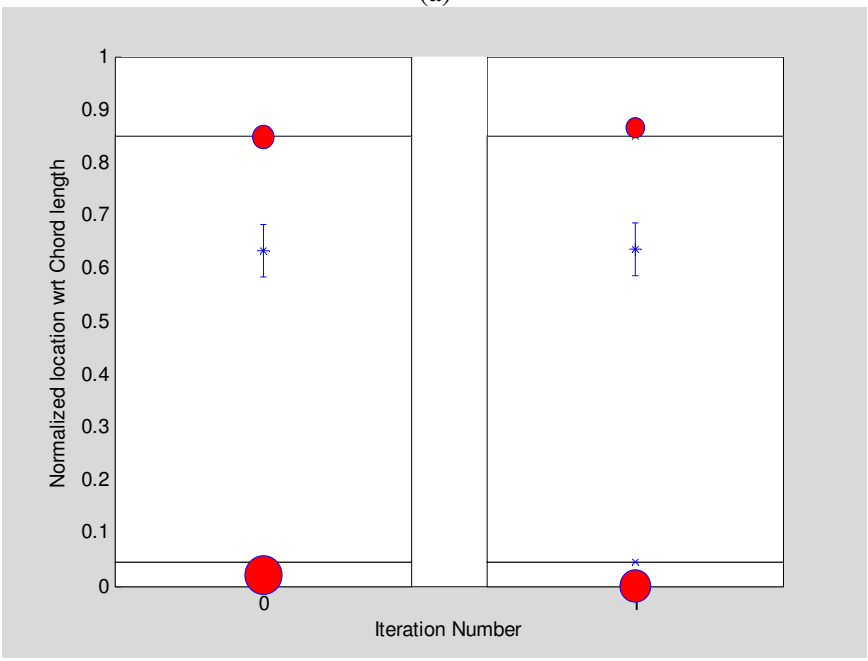

(b)

Figure 3.6. Case A2(b) optimization history for initial spar location at 0.634c.
(a) Objective function convergence history (top) and normalized blade parameters (bottom), and corresponding (b) spar location (*), web extension (|), front and rear ballast weights (•), and start and end of active region (- x -), all normalized by chord length

CASE A3

Figure 3.7 shows the convergence history of the normalized objective function and various normalized blade parameters for Case A3, as well as the convergence history of the spar location, the length of the web extension, the position of the front and rear ballast weights, and the start/end of the active regions as functions of the chord-wise position in the airfoil. The 1st torsional frequency was the most difficult variable to keep within the required bounds. The optimal spar location ended up being set at 0.747c, and the active region extends to its limits. Case A3 took 30 iterations to meet the convergence criteria. Although it seems to be already converged around 15 iterations according to Figure 3.7, it is noticed that the variables are still slightly changing in Figure 3.8, and one of the (maybe-too-tight) convergence criteria took longer to be met.

Figure 3.8(a) shows the evolution of the ply-thicknesses over 30 iterations. The thickness of the outer active composite ply increases to 78% above the nominal ply-thickness while that of the outer and web E-glass plies decreases to half of the nominal ply-thickness. Since 0.5 is a lower bound for the thickness design variable, this indicates that the optimizer is trying to eliminate some of the plies in favor of others. Also, since the outer active plies have a bigger effect in twist than the inner ones, even though both of these plies are increased over the nominal thickness, the optimizer is allowing the outer ply to increase more than the inner one. The increment in nominal thickness is bound by the blade mass/length constraint which reaches its upper limit. Adding passive material on the nose region increases torsional stiffness as well as twist actuation. Adding passive material on the active material region results in a reduction of the twist actuation.

Figure 3.8(b) shows the ply angle variation during the optimization process. Although the set of design variables includes all the ply angles, it only shows the ply angles of the active material plies, the passive ply between active plies, and nose plies. Ply angles for outer E-glass, web and web extension are not shown since they remained at 0^o. Active ply angles converge to [$+49^o$/-52^o] instead of $\pm 45^o$, the ply angles for the active material that would theoretically produce maximum twist actuation. The lack of sensitivity around the optimum point at $\pm 45^o$ for the active plies does not allow the optimizer to reach that global minimum.

The ply angle for the nose moves to –9° and the spar moves to 0.747c, further back than in Case A2(b). This decreases the stiffness and compensates for the material lost at the web, and helps the elastic axis stay within the prescribed boundaries.

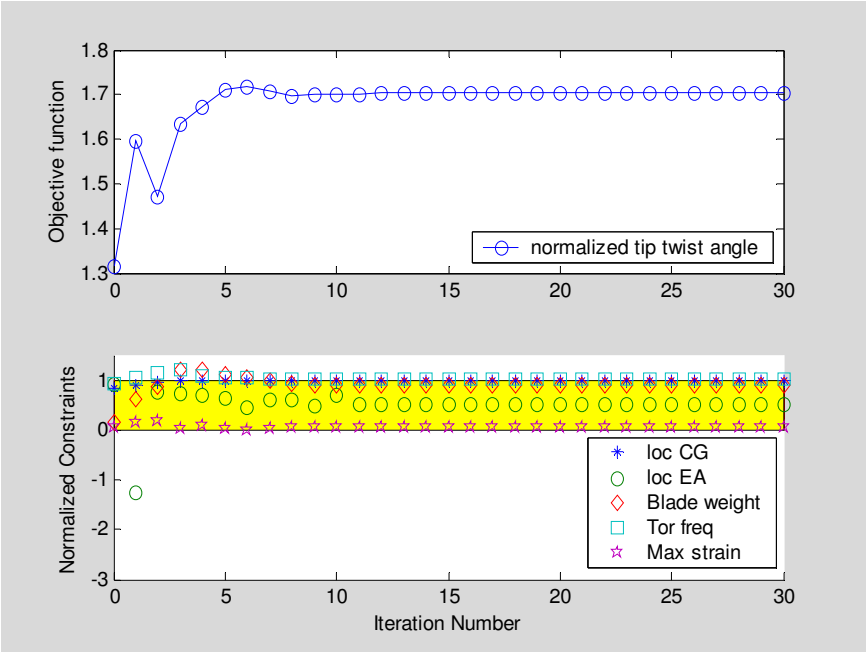

(a)

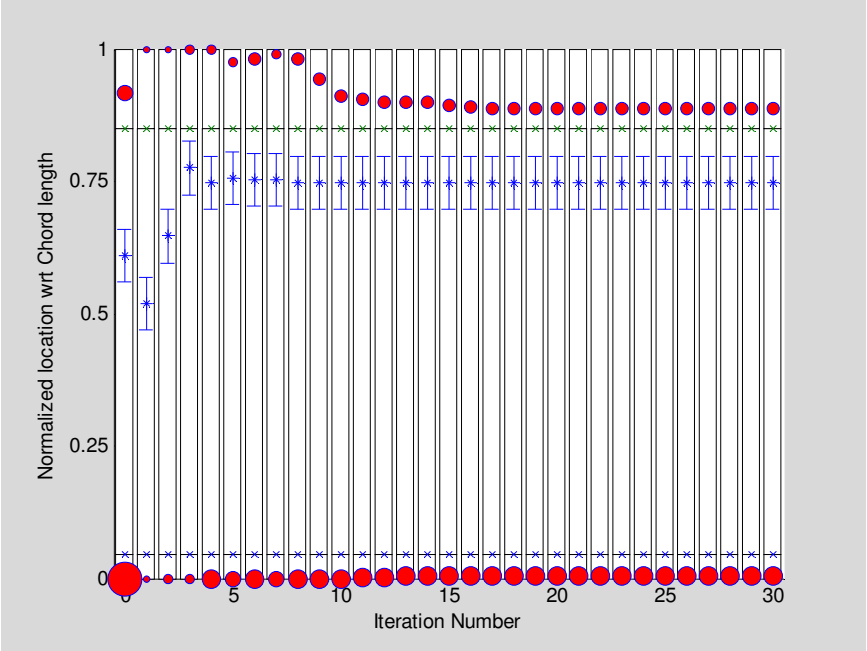

(b)

Figure 3.7. Case A3 optimization history

(a) Objective function convergence history (top) and normalized blade parameters (bottom), and corresponding (b) spar location (*), web extension (|), front and rear ballast weights (•), and start and end of active region (- x -), all normalized by chord length

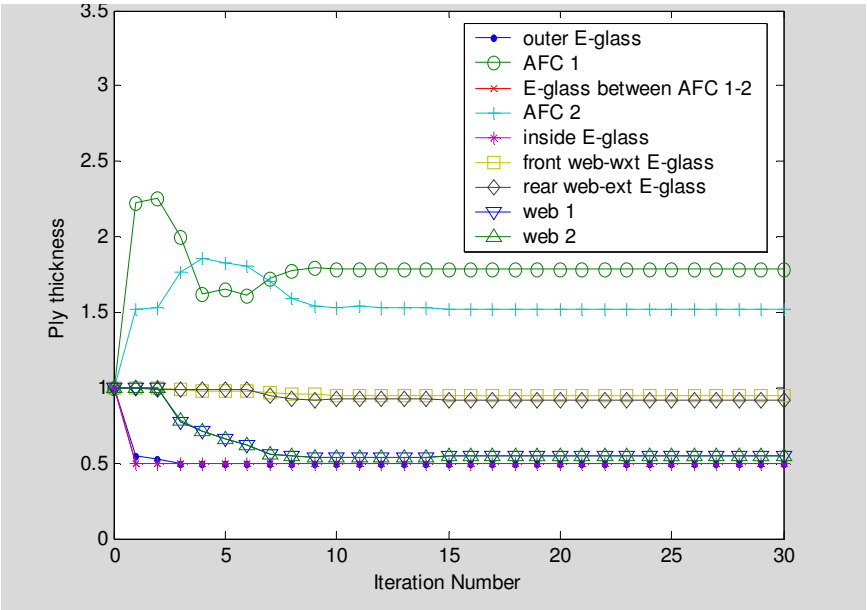

(a)

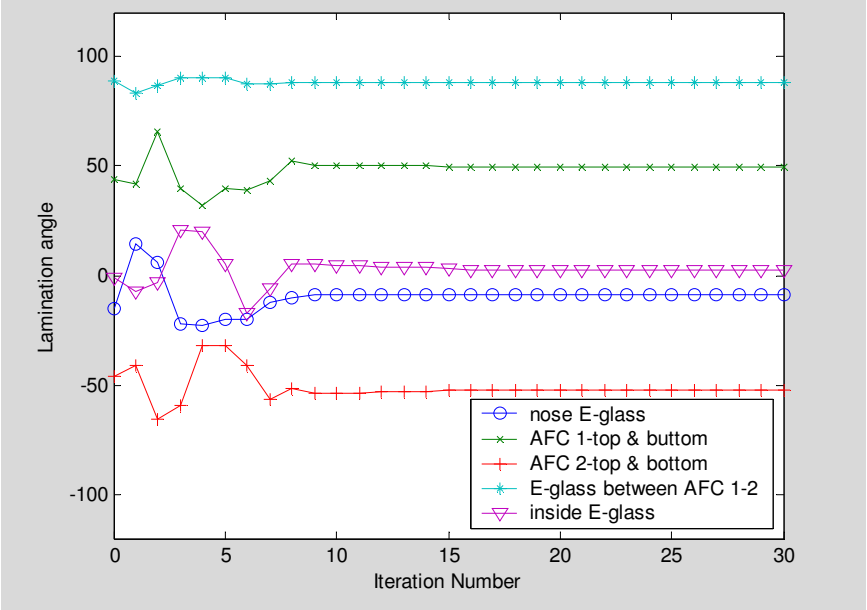

(b)

Figure 3.8. Evolution of Case A3 (a) ply-thickness and (b) ply angles evolution

CASE A4

This case took 11 iterations to converge (Figure 3.9(a)); the normalized twist actuation obtained is 31% higher than the baseline case. Similar to Case A2(b), but now with the complete set of ply angles included among the design variables, Figure 3.9(b) shows the convergence of ply angles for the active plies, the passive ply between active plies, and the nose plies.

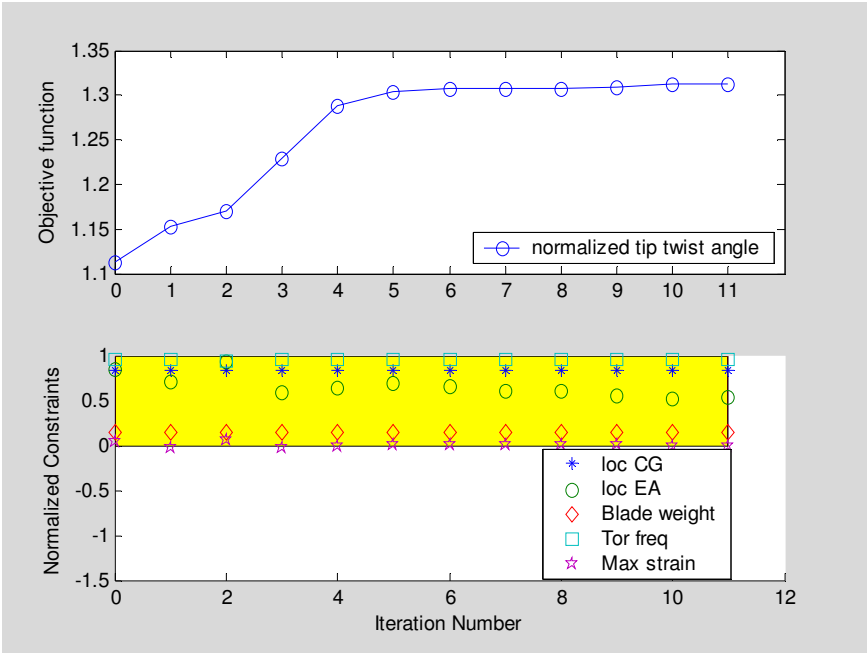

(a)

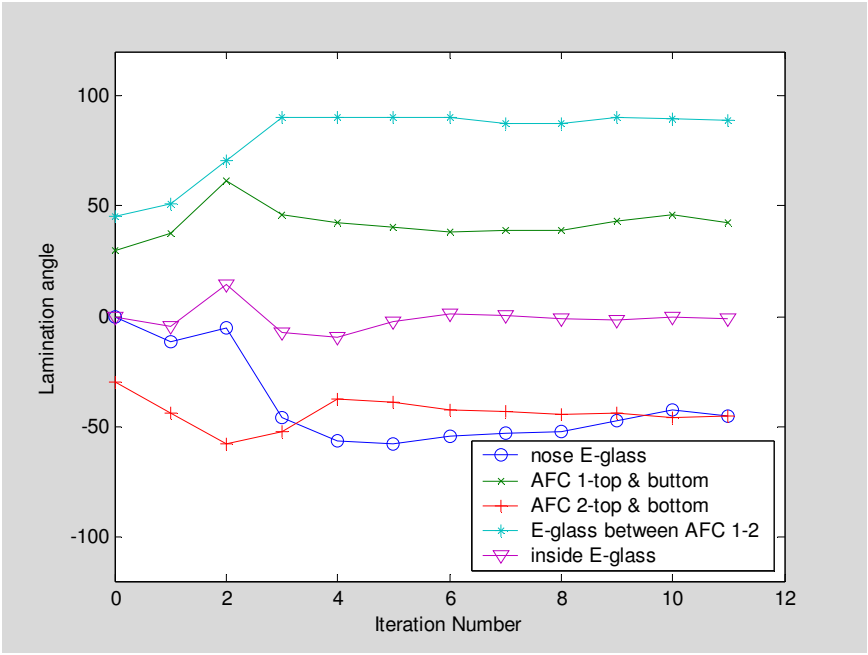

(b)

Figure 3.9. Case A4 optimization history

(a) Objective function convergence history (top) and normalized blade parameters (bottom), and corresponding (b) Evolution of ply angles

The ply angle from the active material ply converges to approximately ± 45˚ as well. The nose E-glass ply angle moves slightly away from 0˚ toward –9˚. These changes adjusted the torsional stiffness of the blade (resulting 1st torsional frequency is 4.89/rev) and the elastic axis location moved toward the leading edge to 0.252c. The final design does not show higher active twist authority than Case A3, but it is still higher than Case A2.

(3) Comparison of ATR-I blade optimization cases

The results obtained by designing the cross section using the optimization framework are summarized in Table 3.11. These cases demonstrate that even though the constraints are tighter than in Case A1, better designs than the original ATR-I reference blade can still be obtained. Case A2 shows that the new constraints can be accommodated by the same set of design variables as in Case A1 and provides very similar twist actuation performance. Case A3 showed the highest twist actuation authority. It can be expected since Case A3 has more design variables than others, which translates into a larger design space. Even though Case A3 presents the highest twist actuation, this optimum solution is not practical. The optimized ply-thicknesses are not integer quantities. As explained previously, the ply-thicknesses should be a multiple of the nominal ply-thickness. Allowing an adjustment on the ply angles provided an extra 11% increase in the twist authority from Case A2.

Table 3.11. Optimized results for Cases 2, 3 and 4

	Case A2(a)	Case A3	Case A4
Tip twist (deg)	1.19	1.70	1.31
Spar location	0.58c	0.74c	0.60c
CG location (%c)	0.28c	0.28c	0.27c
EA location (%c)	0.25c	0.25c	0.25c
Blade mass/length (kg/m)	0.675	0.71	0.676
1^{st} torsional frequency (1/rev)	4.66	5.0	4.83
Maximum strain - shear (με)	6800	6628	6800

3.1.3 Summary of ATR-I design optimization

The developed framework is exemplified in the NASA/Army/MIT ATR-I blade case. The examples showed that the twist performance of the original ATR-I blade, which was already successfully manufactured and tested, could be enhanced to at least 20% higher actuation performance when designed with the suggested optimization framework. During this numerical study, the following six phenomena were noticed.

The constraint of the elastic axis position has an important effect on the position of the spar web in the cross section. By allowing the elastic axis to be located between the quarter cord and the trailing edge, the web would locate further back toward the trailing edge than if the elastic axis is forced to be between the leading edge and the quarter chord point.

The maximum strain occurred near the point of discontinuity in the layup thickness between the active region and the nose region in the cross section. However, adding a passive ply in the nose reduced the stress concentration that arose from that discontinuity. By adding passive material in the nose, the actuation authority of the blade increased.

Instead of using one single most critical component of the strains, it was better to have three separate constraints associated with the maximum strain of two normal and one in-plane shear components. This avoids discontinuity in the constraint, reducing the problem's nonlinear characteristics. Also, by considering three components, the resulting strain/stress may be better distributed in the cross section.

As expected, including ply angles in the design variables made it more difficult for the optimizer to converge than in the case in which the spar location, ballast masses and location, web extension, and start and end position for the active material are used as design variables.

The optimization process was very sensitive to the initial values of the design variables. This

sensitivity was expected for the nonlinear nature of the problem and the gradient-based optimization scheme. The optimizer converged much faster to a local optimum with a feasible initial condition. As explained in Chapter 2 , 'fmincon' is used as an optimization tool provided by MATLAB. It minimizes an objective function with a constrained nonlinear multivariable problem. The problem of optimizing an active twist rotor is a nonlinear one and solutions may fall at local minima. The testing cases showed this phenomenon actually is observed, especially when the initial condition is not within the feasible region. The problem here arises due to the complexity of this design; it is not easy to find the feasible initial condition by changing design variables using experience derived from earlier designs. The approach used here is to run the optimization cases for short iterations with these infeasible initial points and find the feasible points through this optimization process. For future reference, it may be worth to use an alternative optimization scheme that is not dependent on the feasibility of the initial condition.

3.2 ATR-A blade design optimization

In this section, the developed methodology is applied to a more complex problem, the ATR-A. It is given the designation as ATR-A since the blade geometry and properties are generally representative of 21% scale model of the AH-64D Apache helicopter (Figure 3.10) blade.

Figure 3.10. Army AH-64 Apache helicopter DoD photo by Petty Officer 3rd Class Shawn Hussong, U.S. Navy. (Released)

This ATR-A example shows the framework's ability to deal with a more complex model, including different types of airfoil and the swept-droop-twist tip blade geometry. As mentioned earlier, for the ATR-A, MFC has been introduced instead of AFC. MFC has introduced integrated electrodes so the electric feed of the active plies can be implemented inside the skin layup. In comparison with ATR-I, when AFCs were used and the electric feed was constraint to run along the spar web, this new feature adds additional freedom to the design space. To handle these complexities, additional steps are introduced beyond the optimization itself. Besides the two nested optimization loops, special pre-processing of the model and at the end, post-processing/analysis of the optimized design were introduced. These steps address the added complexity of a modern blade and the demands of the manufacturability of one's design.

3.2.1 ATR-A baseline characteristics

The blade geometry is representative of a 21% scale model of the AH-64D Apache blade; however, unlike the actual blade, for ATR-A blade, VR-18 airfoils are used across the entire radius with an articulated root (instead of hingeless). The blade design has a planform with a 20° swept tip beginning at 0.943R, as presented in Figure 3.11. Blade twist is -9° linear. A 0.04c trailing-edge tab is used that is deflected up 3° (Figure 3.12). The blade chord length is 4.410 inches (0.112 m). Other blade properties are presented in Table 3.12. No offsets of the chord-wise center-of-gravity from the blade quarter-chord are necessary during the preliminary design; however, an additional leading edge mass is considered for balancing the inertial properties of the swept tip prior to final design acceptance. The blade feathering-axis is considered coincident with the blade quarter-chord.

Table 3.12. ATR-A blade target properties

	r/R	Mass		x_{CG}		I_θ		EI_{flap}		EI_{chord}		GJ	
		sl/ft	kg/m	inches wrt c/4	% c	sl-ft ($\times 10^{-4}$)	Kg-m ($\times 10^{-4}$)	lb-ft2	N-m2	lb-ft2	N-m2	lb-ft2	N-m2
Main	0.227 ~0.847	0.0187	0.890	0.0705	26.20	1.46	6.49	157.6	65.13	8369	34659	166.8	68.69
	0.847 ~0.938	0.0318	1.522	-0.284	18.87	2.20	9.79	157.6	65.13	8369	3459	166.8	68.69
	0.938 ~0.943	0.0346	1.657	0.	25	1.46	6.49	157.6	65.13	8369	3459	166.8	68.69
Tip	0.943 ~0.965	0.0346	1.657	0.	25	1.46	6.49	157.6	65.13	8369	3459	166.8	68.69
	0.965 ~1.0	0.0133	0.637	0.	25	1.46	6.49	53.7	22.19	980	405	53.8	22.23

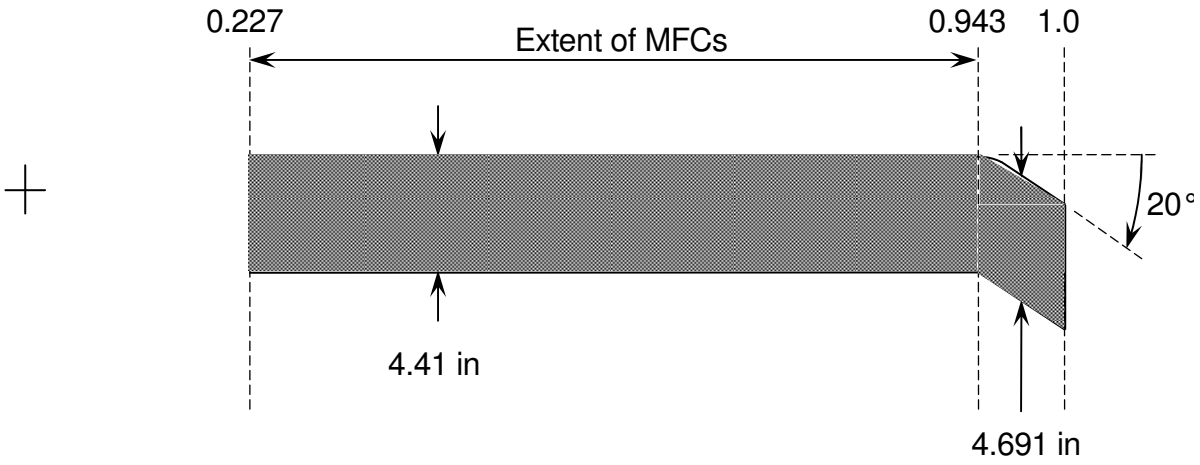

Figure 3.11. ATR-A model blade planform (R = 60.48 inches. Not to scale.)

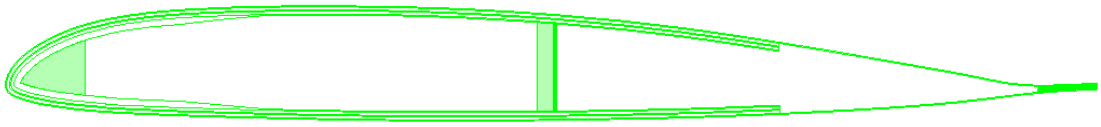

Figure 3.12. ATR-A Cross sectional view (VR18 with trailing edge tab)

For the ATR-A, Macro-Fiber Composite (MFC) actuators are placed from approximately 0.227R to 0.943R, with R = 60.48 inches (1.536 m). The stiffness and mass characteristics, initially used for the optimization studies are set as follows:

$$130 \text{ lb-ft}^2 \leq EI_{Flap} \leq 160 \text{ lb-ft}^2$$

$$5450 \text{ lb-ft}^2 \leq EI_{Lag} \leq 6600 \text{ lb-ft}^2$$

$$135 \text{ lb-ft}^2 \leq GJ \leq 160 \text{ lb-ft}^2$$

$$0.0165 \text{ sl/ft} \leq m \leq 0.0185 \text{ sl/ft}$$

$$0.13 \text{ -ft} \leq I_\theta \leq 0.00016 \text{ sl-ft}$$

3.2.2 Pre-processing: Needs and adjustments

(1) Mesh generator

Before starting on the full optimization process, the capabilities and limitations of the cross-section mesh generation need to be re-visited base on the additional geometric complexities of this case.

The finite element mesh for the composite plies is generated automatically with the code developed by Brown (Brown 2003). It creates the mesh based on geometric parameters such as the aspect ratio of elements, chord length, and nominal thickness of plies. It has great versatility; however, it also comes with some limitations. Since the code is already quite complex, revising it is not desirable. Instead, a series of steps to find ways to solve the limitations with the current code is proposed and described below. Some of the changes to overcome the limitations are done prior and/or outside the optimization cycle as adjusted designs, while other changes are integrated in the optimization process as new subroutines.

For the first case, the limitations are studied and an adjusted design is suggested to model the blade as close as possible. The effect of the adjusted model is compared with respect to the original one. When the effect is negligible, that design is considered throughout the process as an alternative model.

For the others, new subroutines to accommodate the changes were developed using MATLAB, and they were integrated in the optimization process along with the mesh-generator. These additions adjust some details on the modeling of the cross section that the mesh-generator is not able to change automatically. This approach is different from the one above since it happens within the code and make the design follows the model more closely, rather than accepting small difference between the model and the design. This approach also accommodates the changes without revising the mesh-generation itself as mentioned.

When applied to the optimization of more complex blade cross sections, five main limitations have been identified in generating the finite element mesh:

- Mesh overlapping
- Trailing edge tab modeling
- Element distortion
- Electrode modeling
- Foam implementation

In the following sections, these limitations and the approach to work around them are presented in more detail. Among those five limitations, the mesh overlapping, the element distortion, and the foam implementation uses the first approach to overcome the limitations, and the rest follows the second approach.

Mesh Overlapping

Even though the mesh generator is very versatile, in some cases it creates overlapped meshes that cause the UM/VABS to crash. This code failure usually involves overlapping at the nose (leading edge) region of the cross section when the innermost ply becomes thicker than double its nominal thickness (Figure 3.13).

The proposed approach is to introduce a small ply discontinuity at the edge of the nose where the overlapping occurs as shown in Figure 3.14. Analysis on example cases, one with discontinuity and one without, has been performed. When stiffness and inertia constants are compared, the change in the solution is negligible, indicating that the results are similar enough to allow the discontinuity without affecting the results of the optimization. Thus by using this approach, further code modification is not required.

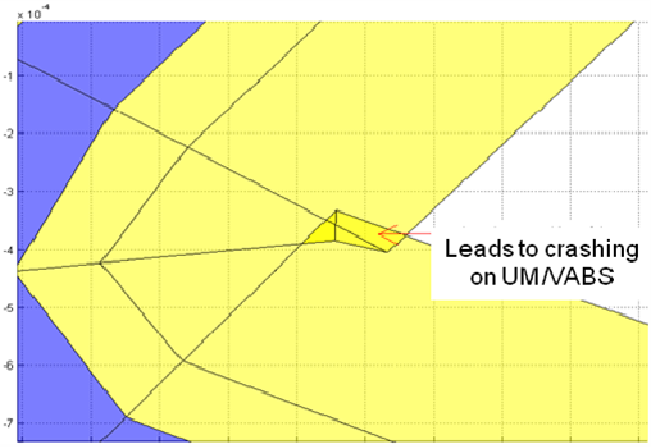

Figure 3.13. Element overlapping close-up

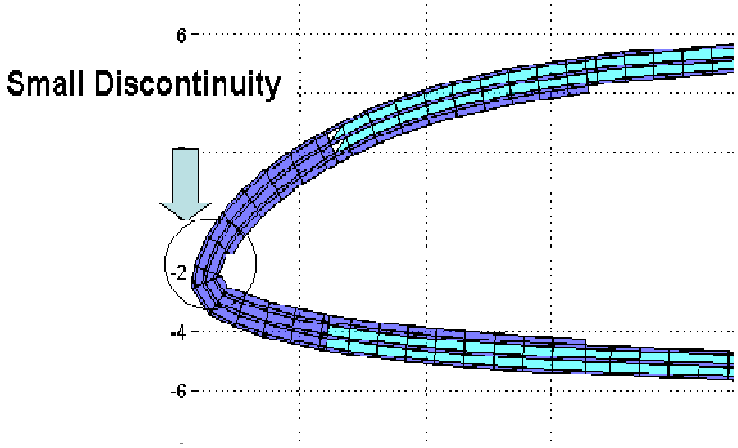

Figure 3.14. Discontinuity introduction at nose

Trailing edge tab modeling

The mesh-generator cannot accurately model the trailing edge of the ATR-A cross section which has a tab. The ATR-A cross section is based on the VR-018 airfoil, which has a trailing edge tab with a slope of 3°. To capture this feature within the code, the elements are re-generated for the trailing edge tab based on elements that the current mesh-generator produces. When the nodes at the start of the trailing edge and at the tip are given, a midpoint between them is generated. Based on these three points along the chord, new elements for the trailing-edge tab are generated that can capture the reflex tab in airfoils like the VR-18.

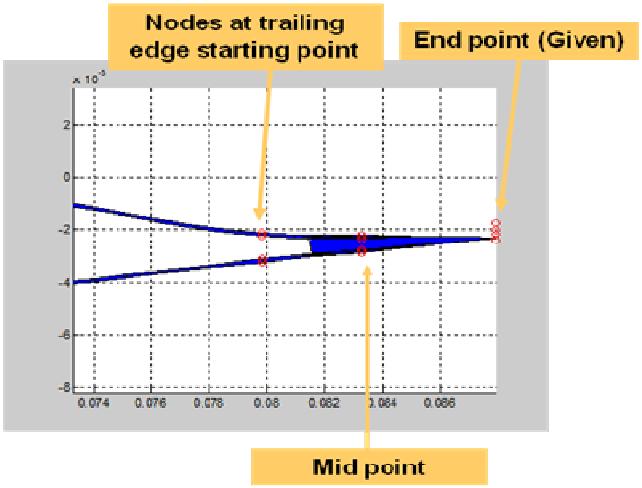

Figure 3.15. Trailing edge tab element modeling approach

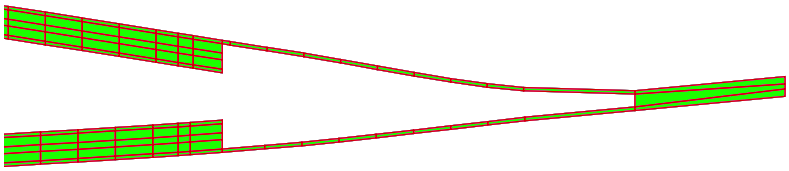

Figure 3.16. Modified model for trailing edge tab

Electrode Modeling

For the ATR-A concept, the electric feed of the adaptive plies is done through integrated electrodes running inside the skin layup (as opposed to along the spar web as in the ATR-I). The electrode thickness is smaller than that of MFC ply, and either E-glass or film adhesive is used to support it in the laminate (Figure 3.17). However, the mesh-generator cannot model the transition from a single ply to triple ply appropriately within a layer (Figure 3.18). To work around this limitation without modifying the mesh-generator, the characteristics of the triple ply are treated as a single ply (Figure 3.19), using classical lamination plate theory (Jones 1999) to substitute for the equivalent properties. This process is done outside and prior to the optimization process, and it is simply treated as another material in the cross section.

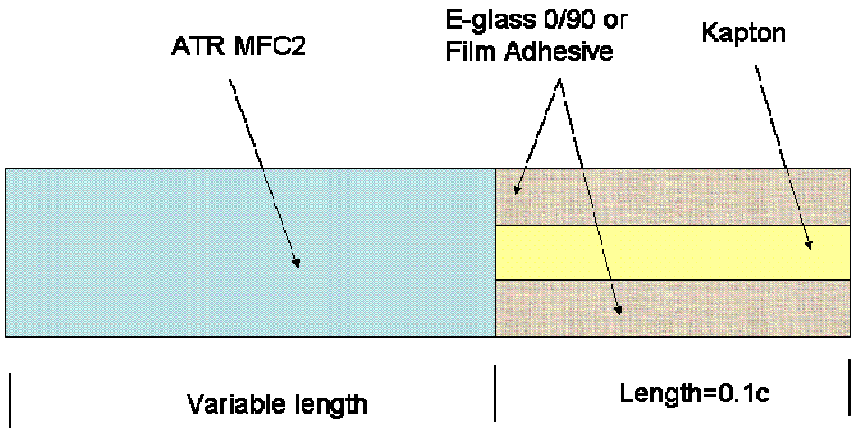

Figure 3.17. MFC unit electrode layup

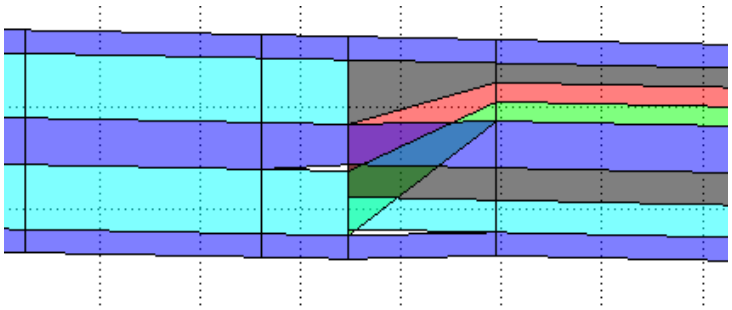

Figure 3.18. Inappropriate transition modeling

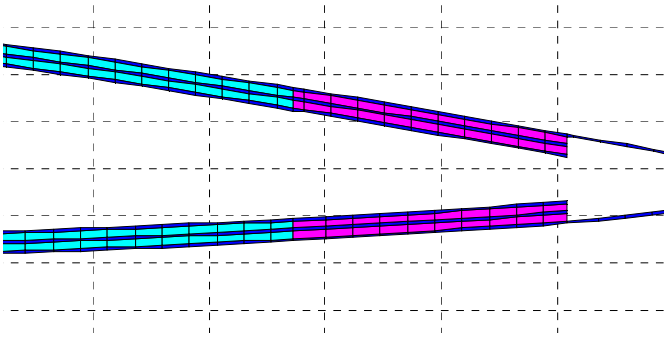

Figure 3.19. Single ply model for electrode (pink)

Distorted element

Another problem in the process of generating the mesh was the appearance of that unwanted triangular elements were observed at the beginning of the upper active plies. The mesh-generator is attempting to create a quadrilateral element, but because it makes the initial and last node coincident, it results in a triangle (Figure 3.20). The effect of this triangular element has been studied by comparing the case with triangular element and the case with that element modified.

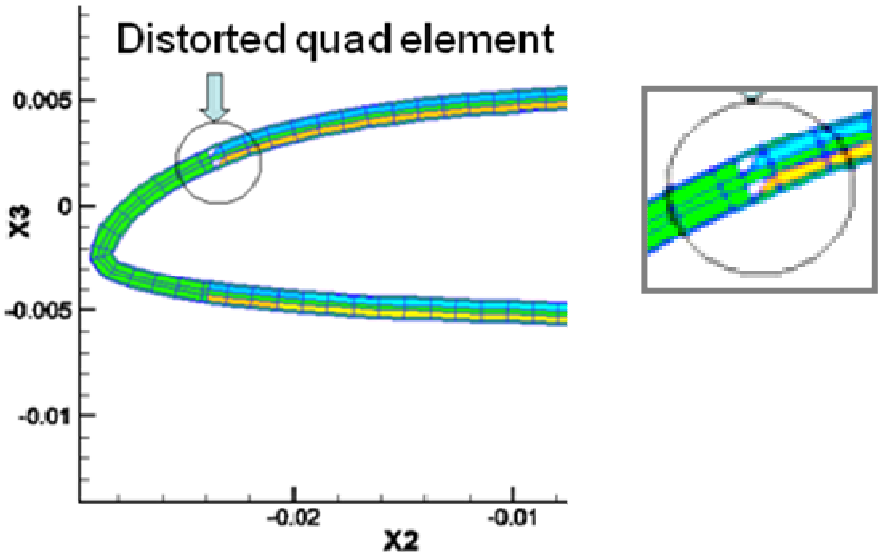

Figure 3.20. Distorted quad element from mesh generator

First, an optimization was run with triangular elements in the mesh. Then the triangular elements were changed to quadrilateral ones using by PATRAN (Figure 3.21) (MSCSoftware 2004), and the changed input file was fed to the optimizer for one cycle. Comparison of this result with the unchanged element model led to the conclusion that the presence of the triangular elements does not affect the solution and leaving the eventual element there is acceptable.

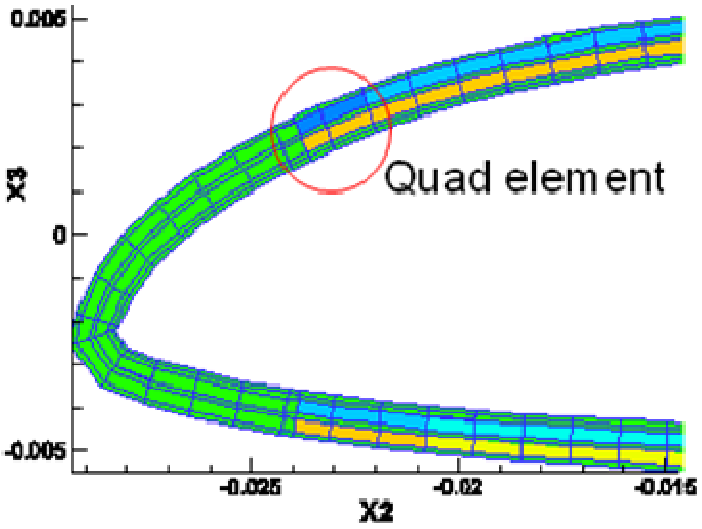

Figure 3.21. Corrected quad element by PATRAN

Foam implementation

The actual ATR-A blade has foam inside, which the mesh-generating code was not able to model. Changing the mesh generator to model the foam was beyond the scope of this study. But, since the foam could be added externally by using MSC.PATRAN, a study was conducted to assess its effect in the optimum design.

This analysis was performed as follows: (1) a complete optimization case was run; (2) the final UM/VABS file obtained from the optimization code was loaded in MSC.PATRAN, since UM/VABS's input file is compatible with MSC.NASTRAN file; (3) a mesh was created to included foam in the entire cross section; and (4) the file from MSC.PATRAN was loaded into the optimization code and a simple analysis (without iteration) was run to obtain new values of a affected blade properties, constraints, and objective function**.**

Figure 3.22 shows a case with one type of foam used for the entire cross section (E=36.0 MPa, υ=0.26, and ρ=35 kg/m^3) and the mesh elements on the nose region of the blade.

Table 3.13 shows the results of this analysis. It is observed that including the foam changes several properties save for the center of gravity location. For the type of foam included in this case, a significant change is observed in the location of the elastic axis: it moves from 0.255c

to 0.3342c (31.1%) and the 1st torsional frequency increases by 22.8%. The actuation angle and blade weight slightly increase by 2.8% and 3.4%, respectively. These relative changes were shown to be relatively constant for a given airfoil shape. From these results, changing the constraints for the location of the elastic axis and the 1st torsional frequency during the optimization process may be required, so when the foam is included the final value is within the required limits. In this way one indirectly takes into account the foam effects without having to model it during the optimization.

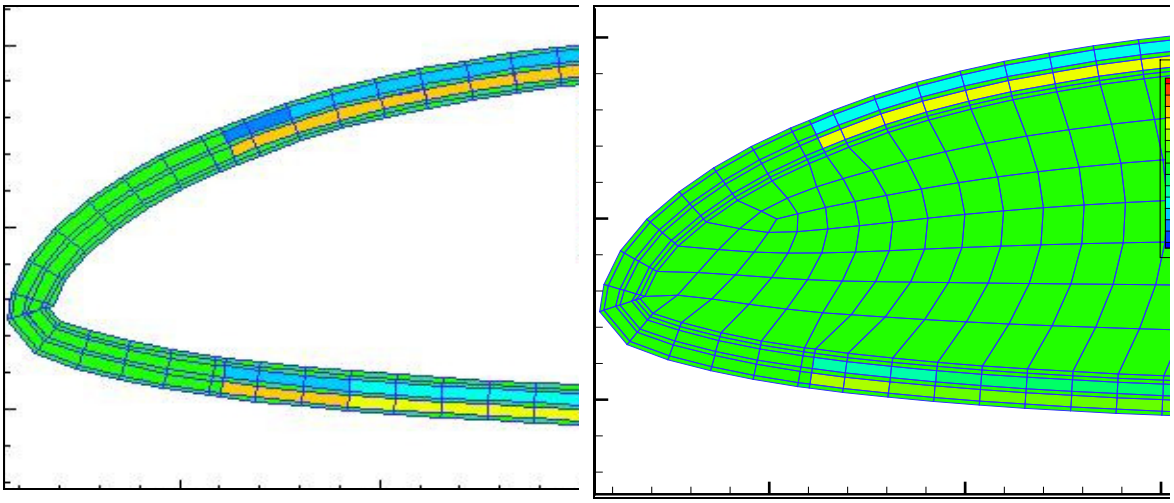

(a) (b)

Figure 3.22. Nose cross section mesh

(a) Without foam, and (b) With foam after modified in MSC.PATRAN.

Table 3.13.Effects of unmodeled foam in the design of the active cross section

	Without foam	With foam
Tip twist actuation (deg peak-to-peak)	3.57	3.67 (2.8%)
Blade mass / length (kg/m)	0.790	0.817 (3.4%)
Center of gravity (CG)	0.255c	0.255c
Elastic axis (EA)	0.255c	0.334 (31.1%)
1st torsional frequency (1/rev)	4.71	5.77 (22.5%)

(2) **Initial design adjustment**

At the very beginning, most of the design variables were selected based on the ATR-I blade. Although the blades are not the same, that provided an initial cross-sectional design for the brand new case. At this stage, the worst loading cases were also based on the ATR-I blade. Then several inner-loop analyses/optimization runs were performed and the variables and/or constraints also manually adjusted to find a more reasonable and feasible initial design. In spite of the problem being highly nonlinear, there are some variables whose effects on the blade characteristics are less difficult to anticipate. For example, the effect of the ballast mass and location to the center of gravity and the blade mass is straighfoward. On the other hand, the start location of the active region affects the maximum strain while the spar location moves the elastic axis—something not obvious. Once the initial design is adjusted and selected, the design is sent to the outer loop. Then the aeroelastic analysis is performed based on that design, and the worst loading is updated.

3.2.3 ATR-A blade optimization cases

The objective of this section is to study the application of the proposed optimization process to the more complex ATR-A rotor. The goal is to maximize the twist actuation while keeping the airfoil, ply-thickness and ply angles fixed. The constraints are set to ensure the blade design is a feasible solution, as summarized in Table 3.14. The seven design variables are the spar location, the magnitude and the location of two ballast masses, and the start/end of the active regions. Eight different cases are studied to find the best configurations and further study the effects of the parameters. The case descriptions are shown in Table 3.15. These seven design variables and their initial values, corresponding to the ATR-A baseline blade, are presented for each case in what follows.

Regarding the elastic axis, from the earlier studies discussed in section 3.2.2(1)0, it is known that the foam will move the elastic axis backward. Anticipating that, the elastic axis constraint is confined between 0.10c and 0.20c. After foam implementation, the elastic axis is

expected to move to near 0.25c, which is the desired location. The center of gravity is constrained between 0.20c and 0.26c, near the desired 0.25c. The maximum strain constraint is defined for each material for both normal and shear components. For example, the maximum shear strain of the MFC is given at 5500 με, which usually is the most critical constraint. Thus, any MFC layer would not experience a shear strain higher than 3670 με, which would be 5500 με considering the safety factor of 1.5.

Table 3.14. Constraints used for the ATR-A optimization study

Elastic axis (EA)	0.10c < EA< 0.20c
Center of gravity (CG)	0.20c < CG < 0.26c
Blade mass / length (kg/m)	0.79 < *m* < 0.87
1st torsional frequency (1T)	1T < 5/rev
Local Strain in the worst loading case	1.5xMax strain < ultimate strength of original constituent material
Ballast weight (kg/m)	0.0 <weight < 1.0
Active region	0.085 c< Loc<0.85c
Spar location	0.3c < $Spar_{loc}$ < 0.85c

During the optimization process, the following effects are noticed. As the spar location moves backward, the twist rate becomes higher since it increases the active region forward of the spar location. However, the change in the spar location also pushes the elastic axis backwards. To reduce the maximum shear strain, the starting location of the active region needs to go backwards to the upper bound, which will reduce the twist rate. Moving the end location of the active region backward increases the twist rate, but this does not have as much of an effect as moving the start of the active region forward. Unlike the ATR-I blade, a 45° lamination angle of passive ply between two active plies at the nose increases the shear strain. Blade weight and center of gravity constraints are preventing the active end from moving further backwards, which would increase the twist rate. From this, it is noticed once more that the optimization of active twist rotors is a very nonlinear and complex problem.

Based on these studies and the given requirements, the following cases were chosen and each studied through the optimization process. For all these cases, the nose reinforcement was introduced instead of the D-spar-like reinforcement used in ATR-I.

Table 3.15. ATR-A optimization cases

	No. of web plies	No. of extra plies at nose	Upper limit of spar location
Case T1(a)	3	3	0.85
Case T1(b)		5	0.85
Case T1(c)		3	0.45
Case T1(d)		5	0.45
Case T2(a)	2	3	0.85
Case T2(b)		5	0.85
Case T2(c)		3	0.45
Case T2(d)		5	0.45

CASE T1(a)

The goal for this case is to generate the initial (feasible) design that will be used for the other seven variants to follow. For this first case, the following conditions were applied:

- Design variables: Active start, active end, two ballast weights, spar location
- End of the nose reinforcement = Active start +0.1c
- **Three** plies are used for the nose reinforcement
- **Three** plies are used on the spar-web

Table 3.16. Case T1(a) Initial and optimized values

	Initial	Optimized
Active start	0.131c	0.170c
Active end	0.762c	0.767c
Ballast weight mass	(0.284, 0.00)	(0.310, 0.0000)
Ballast weight location	(0.022c, 0.576c)	(0.022c, 0.477c)
Spar location	0.578c	***0.479c***
Twist rate (deg/m)	2.70	2.27
1st torsional frequency (1/rev)	4.44	4.25
Blade mass / length (kg/m)	0.850	0.870
Max strain (μm/m)	**6180**	5500
Center of gravity (CG)	0.257c	0.260c
Elastic axis (EA)	**0.257c**	0.200c

Table 3.16 shows the critical blade characteristics related to the design variables and the constraints of the initial and the optimized designs. Figure 3.23 presents the optimization history of the objective function, active tip twist, and the normalized constraints (a), as well as the corresponding results for each iteration (b).

The initial design has violated two constraints: the location of the elastic axis and the maximum strain, which are shown in Figure 3.23(a) and in bold in the first column of Table 3.16. As a result, the spar location moved forward to satisfy the elastic axis constraint (shown in italic in the second column of Table 3.16). For maximum strain constraint violation, the start location of the active region moved backward, which decreased the active twist rate to 2.27 from 2.70, about 20%.

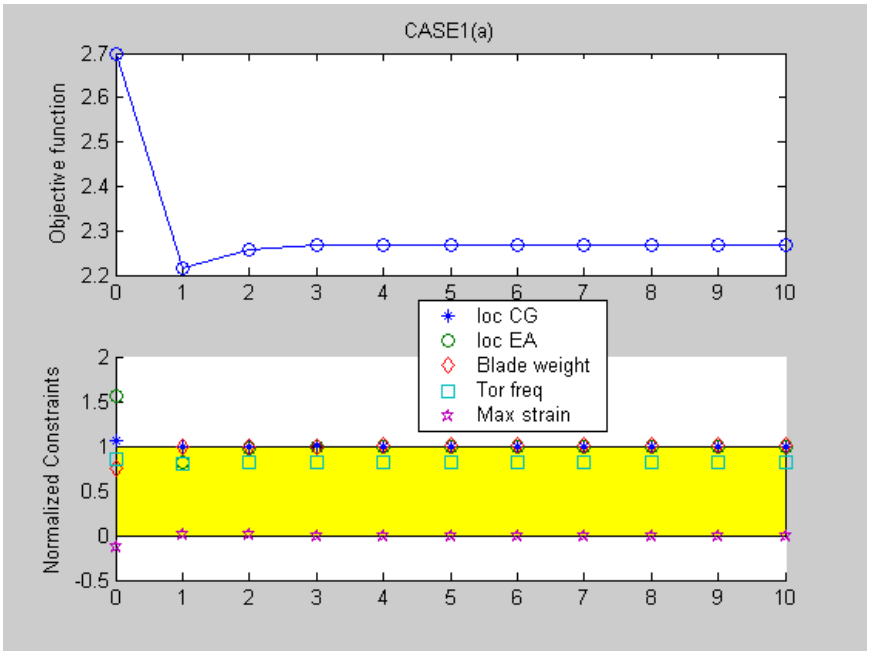

(a)

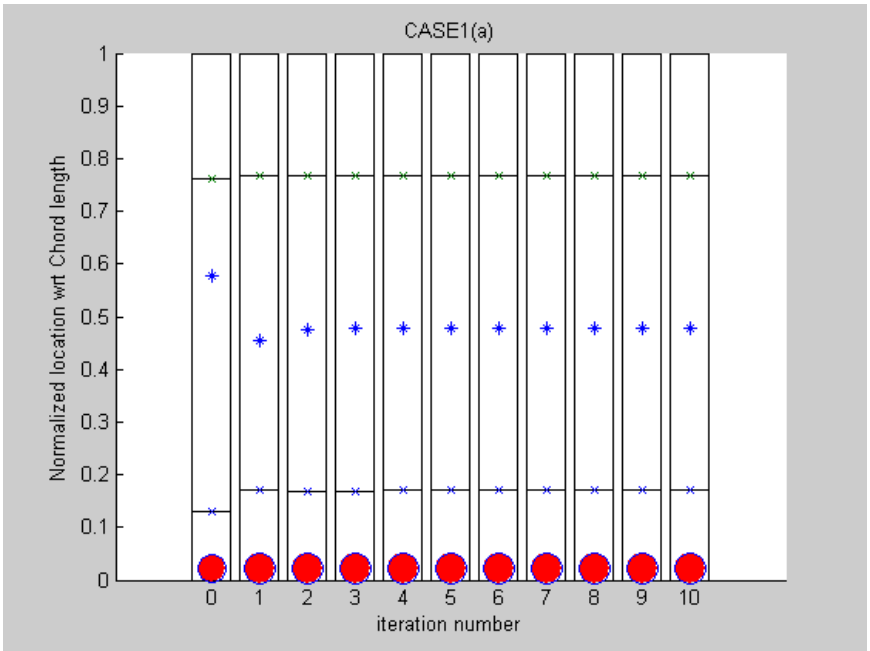

(b)

Figure 3.23. Case T1(a) Optimization history

(a) Objective function convergence history (top) and normalized blade parameters (bottom), corresponding (b) spar location (*), web extension (|), front and rear ballast weights (•), and start and end of active region (- x -), all normalized by chord length.

CASE T1(b)

Consider the follow characteristics of this case:

- Design variables: Active start, active end, two ballast weights, spar location
- End of the nose reinforcement= Active start +0.1c
- **Five** plies are used for the nose reinforcement
- Three plies are used on the spar-web

Table 3.17. Case T1(b) Initial and optimized values

	Initial	Optimized
Active start	0.131c	0.130c
Active end	0.762c	0.761c
Ballast weight mass	(0.284, 0.000)	(0.283, 0.000)
Ballast weight location	(0.022c, 0.576c)	(0.022c, 0.489c)
Spar location	0.578c	0.491c
Twist rate (deg/m)	2.68	2.53
1st torsional frequency (1/rev)	4.45	4.36
Blade mass / length (kg/m)	0.871	0.870
Max strain (μm/m)	**5490**	5500
Center of Gravity (CG)	0.260c	0.260c
Elastic axis (EA)	**0.239c**	**0.191c**

As studied earlier, the optimization scheme used here showed better performance when the initial design was a feasible one. When the initial design was not feasible, the code sometimes crashed or took a longer to converge to the optimal solution. To help loosen the maximum strain constraint violation of the initial design of Case T1(a), additional plies are applied to the nose reinforcement (5 plies). This also helped move the elastic axis forward. By reducing the violated constraints, the optimization only took two iterations to converge. As a result, the active twist rate decreased from 2.67 to 2.53, about 5.6%. This shows that the constraints can be satisfied, mostly by moving the spar location backward, without sacrificing the active twist rate significantly as when the start of the active region was moved backward as shown in Case T1(a).

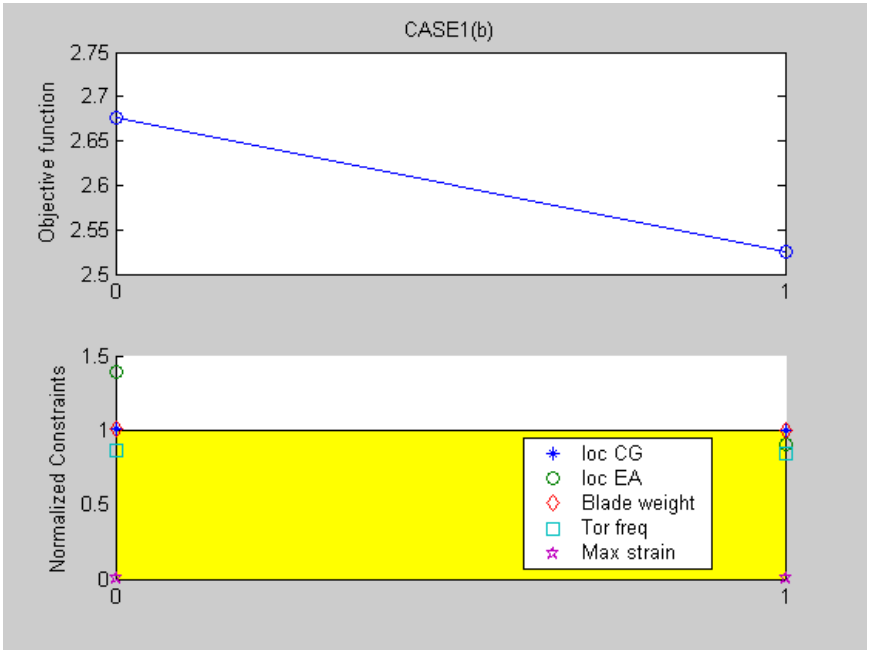

(a)

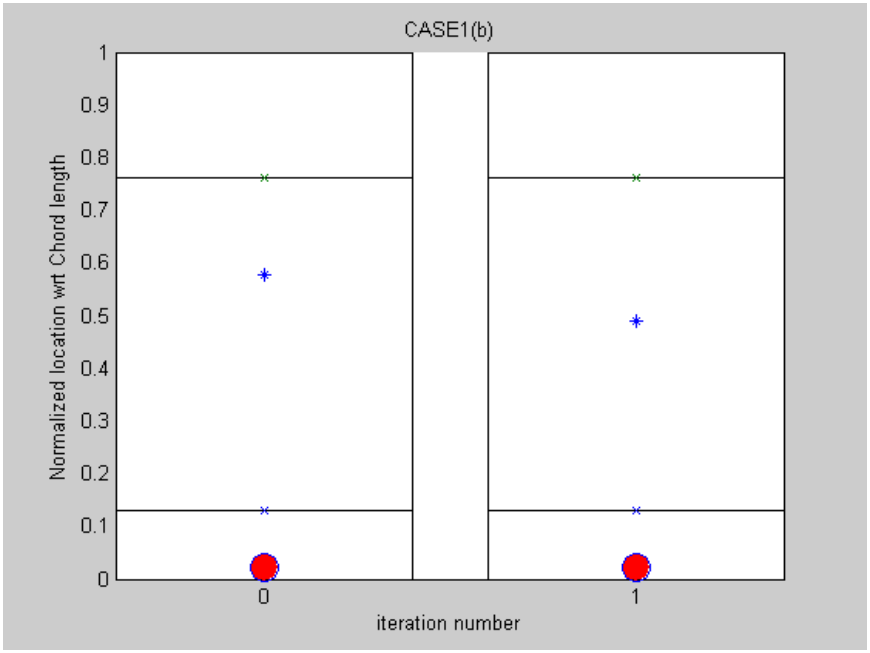

(b)

Figure 3.24. Case T1(b) Optimization history

(a) Objective function convergence history (top) and normalized blade parameters (bottom), corresponding (b) spar location (*), web extension (|), front and rear ballast weights (•), and start and end of active region (- x -), all normalized by chord length.

CASE T1(c)

Another variant of Case T1(a) is considered here with the following characteristics:

- Design variables: Active start, active end, two ballast weights, spar location
- End of the nose reinforcement= Active start +0.1c
- **Three** plies are used for the nose reinforcement
- Three plies are used on the spar-web
- Upper limit and initial point of spar location are now reduced to **0.45c**

Table 3.18. Case T1(c) Initial and optimized values

	Initial	Optimized
Active start	0.131c	**0.170c**
Active end	0.762c	0.766c
Ballast weight mass	(0.284, 0.00)	(0.310, 0.000)
Ballast weight location	(0.022c, 0.448c)	(0.022c, 0.448c)
Spar location	**0.450c**	0.450c
Twist rate (deg/m)	2.48	2.21
1st torsional frequency (1/rev)	4.24	4.19
Blade mass / length (kg/m)	0.851	0.870
Max strain	**6150**	5490
Center of gravity (CG)	0.263c	0.260c
Elastic axis (EA)	**0.176c**	0.179c

Similar to Case T1(b), one of the initial values that violates the constraints, in this case the elastic axis, was moved to a feasible point. To help loosen the elastic axis constraint violation at the initial design of Case T1(a), the upper limit and the initial location of the spar web were set to 0.45c. This located the initial elastic axis within the constraint but the maximum strain out of bound. To avoid this violation, the start location of the active region was backward and, as a result, the active twist rate has been reduced. This case also took only two iterations to converge.

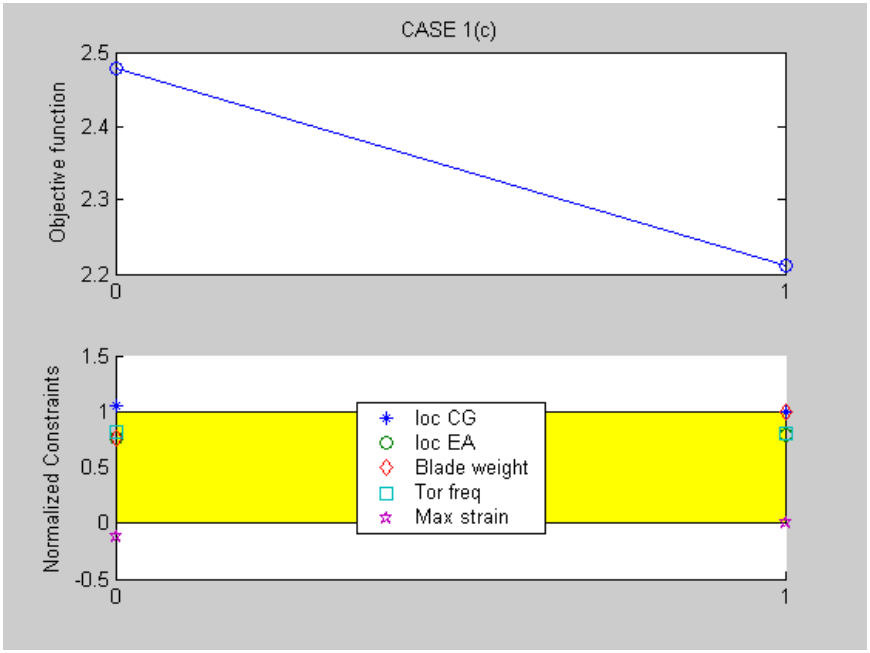

(a)

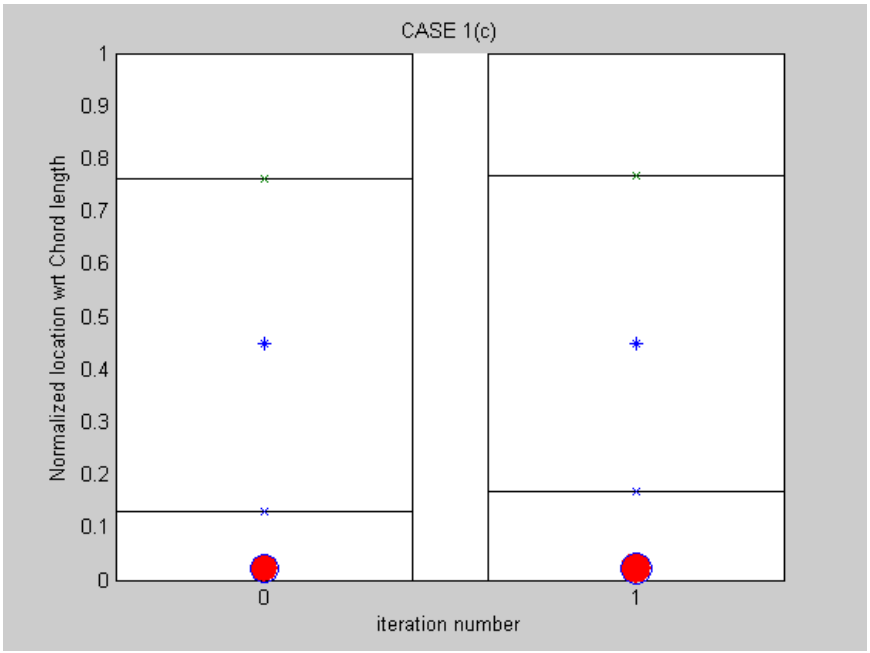

(b)

Figure 3.25. Case T1(c) Optimization history
(a) Objective function convergence history (top) and normalized blade parameters (bottom), corresponding (b) spar location (*), web extension (|), front and rear ballast weights (•), and start and end of active region (- x -), all normalized by chord length.

CASE T1(d)

Finally, the following is considered:

- Design variables: Active start, active end, two ballast weights, spar location
- End of the nose reinforcement = Active start +0.1c
- **Five** plies are used for nose reinforcement
- Three plies are used on the spar-web
- Upper limit and initial point of spar location are now reduced to **0.45c**

Table 3.19. Case T1(d) Initial and optimized values

	Initial	Optimized
Active start	0.130c	0.127c
Active end	0.761c	0.761c
Ballast weight mass	(0.283, 0.000)	(0.282, 0.000)
Ballast weight location	(0.022c, 0.448c)	(0.022c, 0.448c)
Spar location	**0.450c**	0.450c
Twist rate (deg/m)	2.46	2.47
1st torsional frequency (1/rev)	4.27	4.27
Blade mass / length (kg/m)	0.870	0.870
Max strain (μm/m)	**5475**	5498
Center of gravity (CG)	0.260c	0.260c
Elastic axis (EA)	**0.163c**	0.163c

This is a combination of Case T1(b), which has five plied at the nose reinforcement, and Case T1(c),which has a spar location at 0.45c, and there is no constraint violated at the initial point. The optimum design did not move far from the initial design and the active twist rate increased slightly to 2.470 from 2.455.

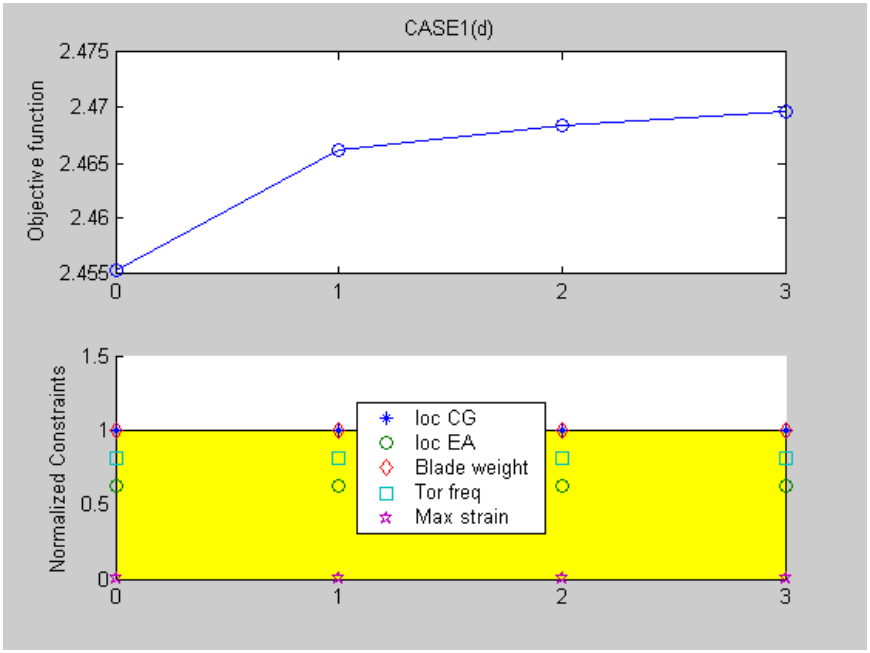

(a)

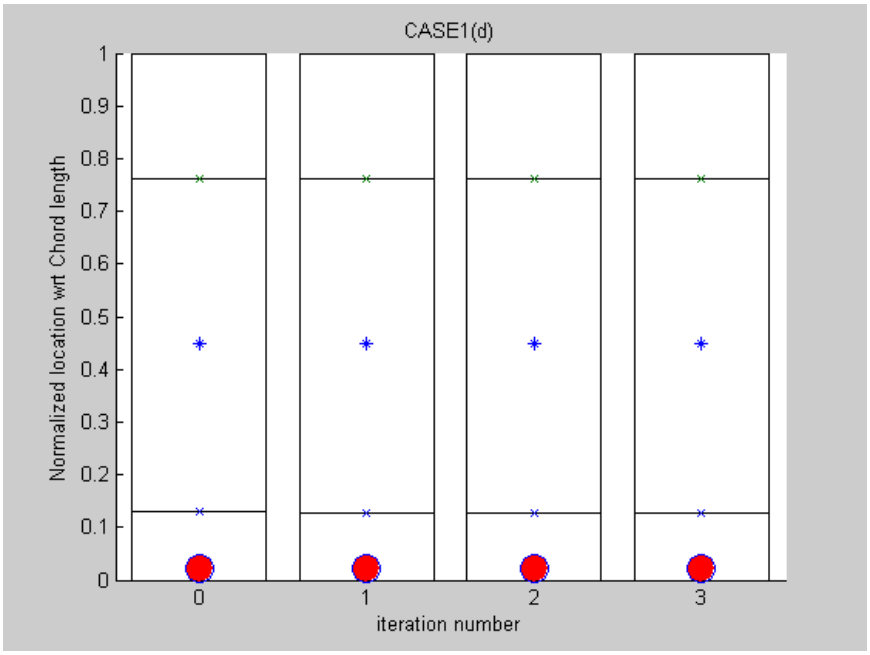

(b)

Figure 3.26. Case T1(d) Optimization history

(a) Objective function convergence history (top) and normalized blade parameters (bottom), corresponding (b) spar location (*), web extension (|), front and rear ballast weights (•), and start and end of active region (- x -), all normalized by chord length.

CASE T2(a)

This is a modified case from Case T1(a). This case serves as a baseline for the other variants of Case T2 to follow. For this second baseline case, the following conditions were applied:

- Design variables: Active start, active end, two ballast weights, spar location
- End of the nose reinforcement = Active start +0.1c
- Nose reinforcement with **triple** the thickness
- **Two** plies are used on the spar-web

Table 3.20. Case T2(a) Initial and optimized values

	Initial	Optimized
Active start	0.131c	0.173c
Active end	0.762c	0.768c
Ballast weight mass	(0.284, 0.000)	(0.311, 0.000)
Ballast weight location	(0.022c, 0.576c)	(0.022c, 0.540c)
Spar location	0.578c	0.542c
Twist rate (deg/m)	2.68	2.37
1st torsional frequency (1/rev)	4.41	4.33
Blade mass / length (kg/m)	0.849	0.870
Max strain (μm/m)	**6180**	5500
Center of gravity (CG)	0.263c	0.260c
Elastic axis (EA)	**0.217c**	0.200c

Here the plies on the spar-web have been reduced from three to two. It moves the elastic axis closer to the feasible range of the constraint by reducing the stiffness, but not enough to move into the feasible range. Adversely, this made the maximum strain constraint worse. As a result, when optimized, the start point of the active region moved backward to satisfy the maximum strain constraint. Moreover, the final active twist rate is 2.37, which is 4.4% greater than Case T1(a), 2.27, while all constraints are satisfied.

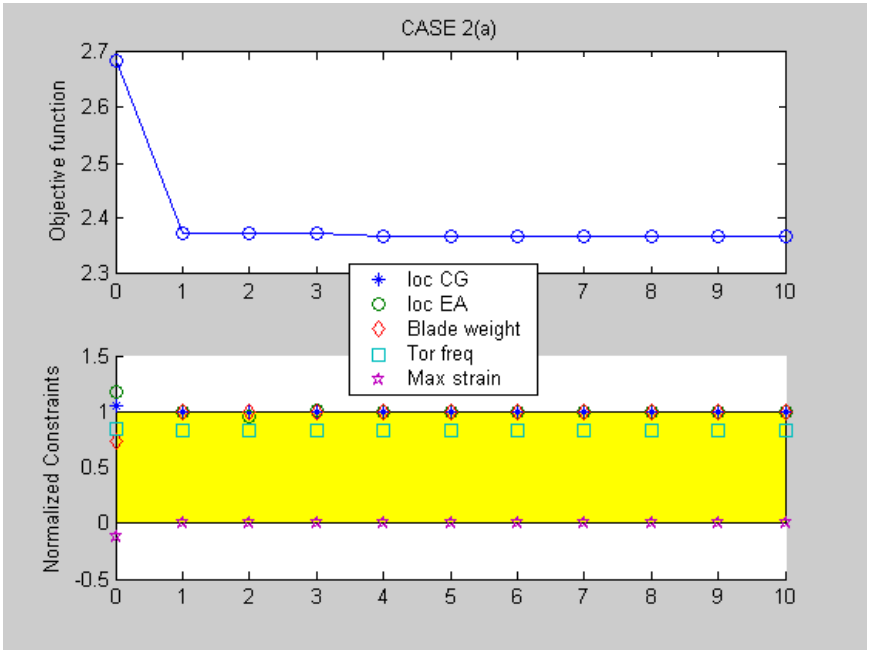

(a)

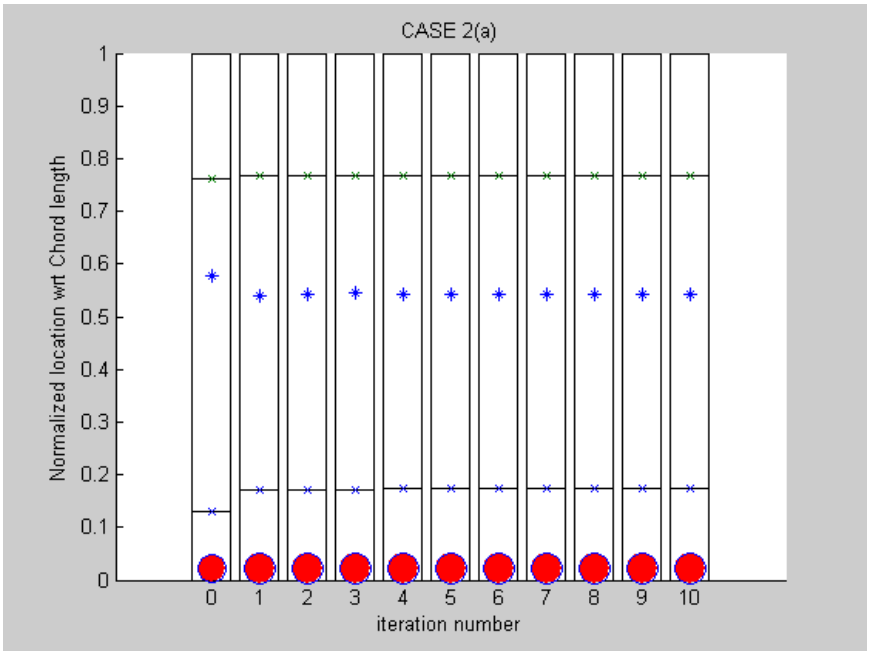

(b)

Figure 3.27. Case T2(a) Optimization history

(a) Objective function convergence history (top) and normalized blade parameters (bottom), corresponding (b) spar location (*), web extension (|), front and rear ballast weights (•), and start and end of active region (- x -), all normalized by chord length.

CASE T2(b)

Consider the following:

- Design variables: Active start, active end, two ballast weights, spar location
- End of the nose reinforcement = Active start +0.1c
- **Five** plies are used for the nose reinforcement
- **Two** plies are used on the spar-web

Table 3.21. Case T2(b) Initial and optimized values

	Initial	Optimized
Active start	0.131c	0.131c
Active end	0.762c	0.762c
Ballast weight mass	(0.284, 0.000)	(0.284, 0.000)
Ballast weight location	(0.022c, 0.576c)	(0.022c, 0.575c)
Spar location	0.578c	0.577c
Twist rate (deg/m)	2.66	2.66
1st torsional frequency (1/rev)	4.42	4.36
Blade mass / length (kg/m)	0.870	0.870
Max strain (μm/m)	**5500**	5500
Center of gravity (CG)	0.260c	0.260c
Elastic axis (EA)	**0.200c**	0.200c

This is a combination of Case T1(b) and Case T2(a). As in Case T1(b), two more plies are added to the nose reinforcement to meet the maximum strain constraint violation at the initial design of Case T2(a). This also helps to move the elastic axis forward to 0.2002c but slightly out of the upper limit, 0.20c. The optimization history shows a small "bump", but mostly the variables remain near their initial values and the elastic axis constraint is now satisfied.

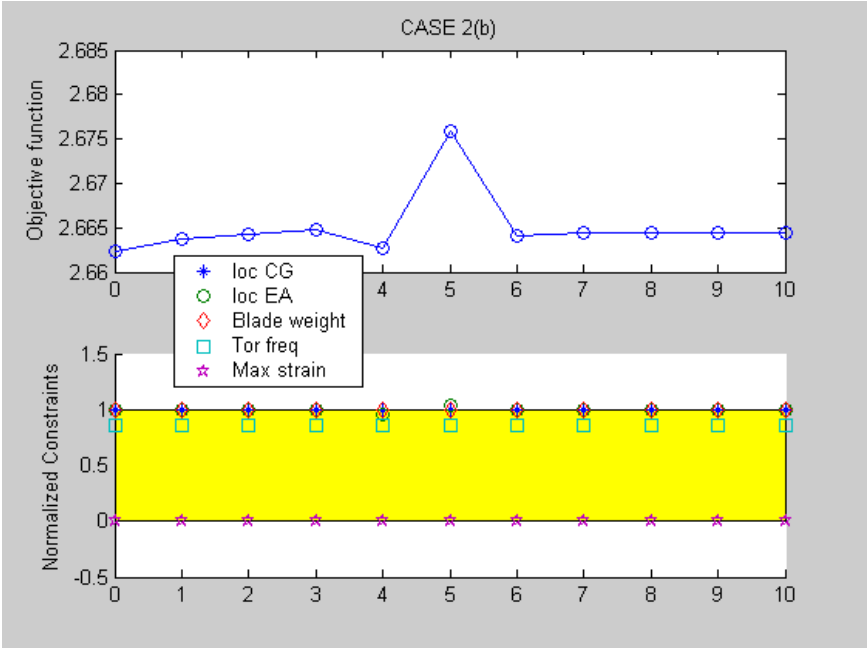

(a)

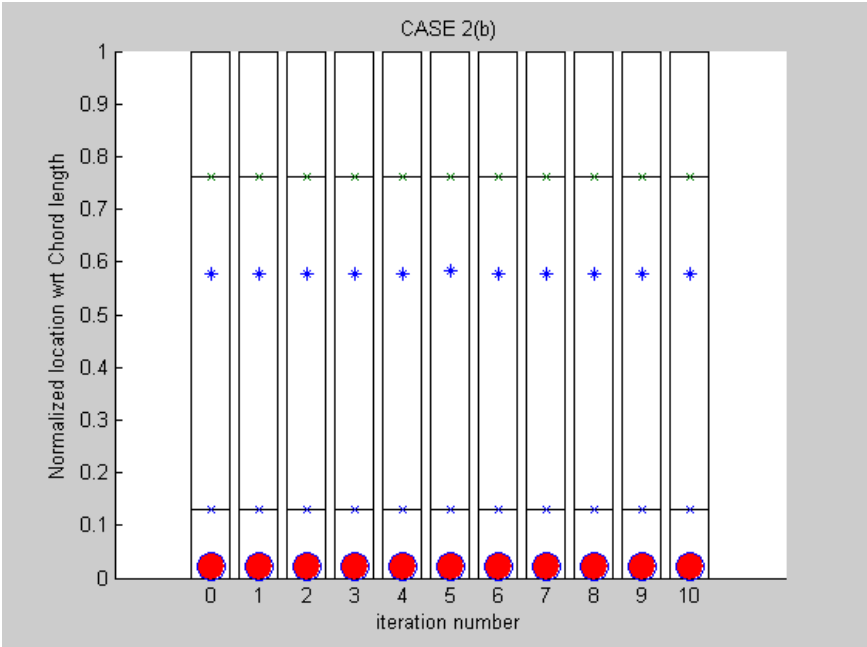

(a)

Figure 3.28. Case T2(b) Optimization history
(a) Objective function convergence history (top) and normalized blade parameters (bottom), corresponding (b) spar location (*), web extension (|), front and rear ballast weights (•), and start and end of active region (- x -), all normalized by chord length.

CASE T2(c)

Consider the following:

- Design variables: Active start, active end, two ballast weights, spar location
- End of the nose reinforcement = Active start +0.1c
- **Three** plies are used for the nose reinforcement
- Two plies are used on the spar-web
- Upper limit and initial point of spar location are now reduced to **0.45c**

Table 3.22. Case T2(c) Initial and optimized values

	Initial	Optimized
Active start	0.131c	**0.171c**
Active end	0.762c	0.768c
Ballast weight mass	(0.284, 0.000)	(0.311, 0.000)
Ballast weight location	(0.022c, 0.448c)	(0.022c, 0.448c)
Spar location	**0.450c**	0.450c
Twist rate (deg/m)	2.471	**2.21**
1st torsional frequency (1/rev)	4.13	4.06
Blade mass / length (kg/m)	0.846	0.870
Max strain (μm/m)	**6160**	5500
Center of gravity (CG)	0.263c	0.260c
Elastic axis (EA)	**0.136c**	0.140c

This case modifies Case T2(a) similarly as it was done Case T1(c). This case has two plies for the spar-web as in Case T2(a). As in Case T1(c), the upper limit and the initial location of the spar are set to 0.45c. At the initial design, the elastic axis is moved to a feasible point and the maximum strain is outside of its upper limit. Similar trends are noticed in Case T1(c). The start location of the active region was moved backward and, as a result, the active twist rate was reduced by 19.5%.

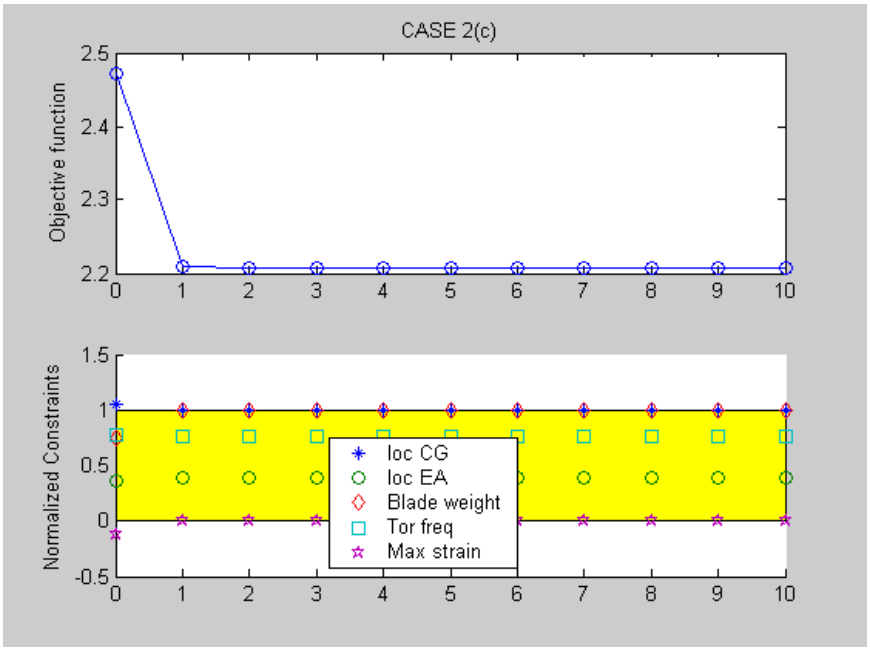

(a)

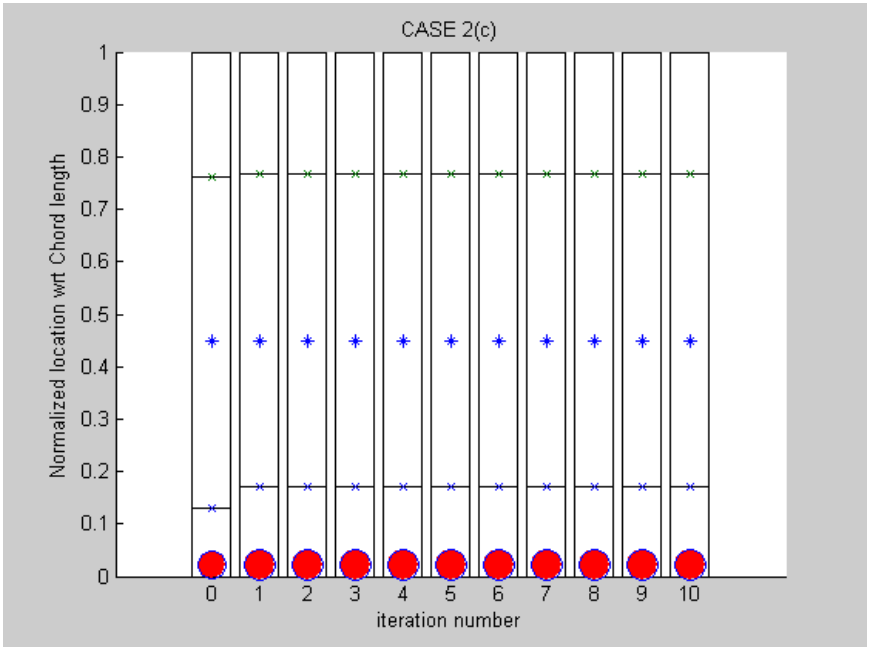

(b)

Figure 3.29. Case T2(c) Optimization history
(a) Objective function convergence history (top) and normalized blade parameters (bottom), corresponding (b) spar location (*), web extension (|), front and rear ballast weights (•), and start and end of active region (- x -), all normalized by chord length.

Case T2(d)

Consider the following:

- Design variables: Active start, Active end, two ballast weights, spar location
- End of the nose reinforcement = Active start +0.1c
- **Five** plies are used for nose reinforcement
- Two plies are used on the spar-web
- Upper limit and initial point of spar location is now reduced to **0.45c**

Table 3.23. Case T2(d) Initial and optimized values

	Initial	Optimized
Active start	0.131c	0.1285c
Active end	0.762c	0.7629c
Ballast weight mass	(0.284, 0.000)	(0.283, 0.000)
Ballast weight location	(0.022c, 0.448c)	(0.022c, 0.448c)
Spar location	0.450c	0.450c
Twist rate (deg/m)	2.45	2.46
1st torsional frequency (1/rev)	4.15	4.14
Blade mass / length (kg/m)	**0.871**	0.870
Max strain (μm/m)	**5480**	5500
Center of gravity (CG)	0.260c	0.260c
Elastic axis (EA)	**0.124c**	0.124c

This case combines Case T2(b), which has five plies at the nose reinforcement, and Case T2 (c), which has a spar location at 0.45c. This is similar to Case T1(d), but the blade mass per unit length was slightly out of its upper limit. This violation would be the reason why this case took longer to converge than Case T1(d). The optimum design shows a slight increase in twist rate, similar to Case T1(d).

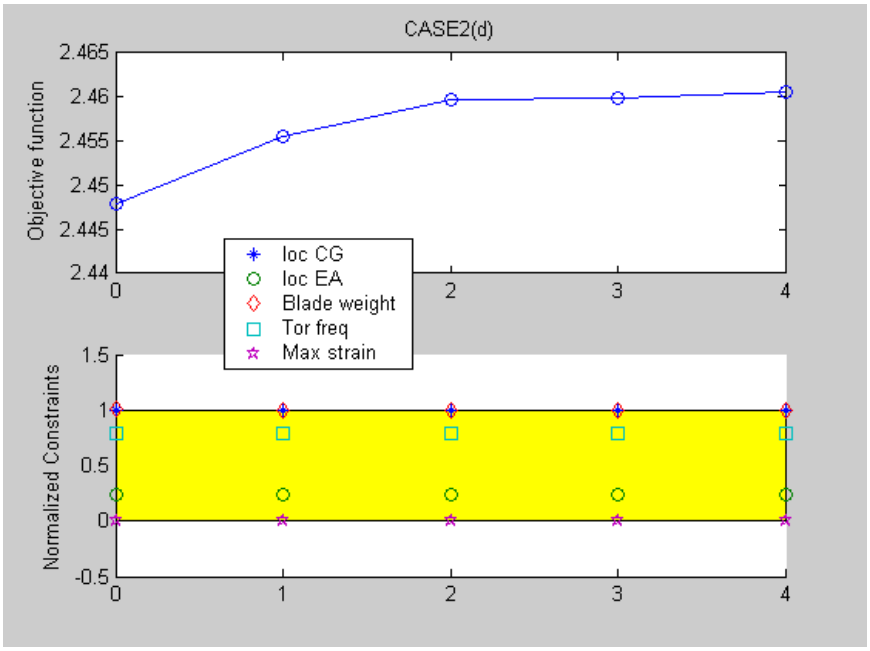

(a)

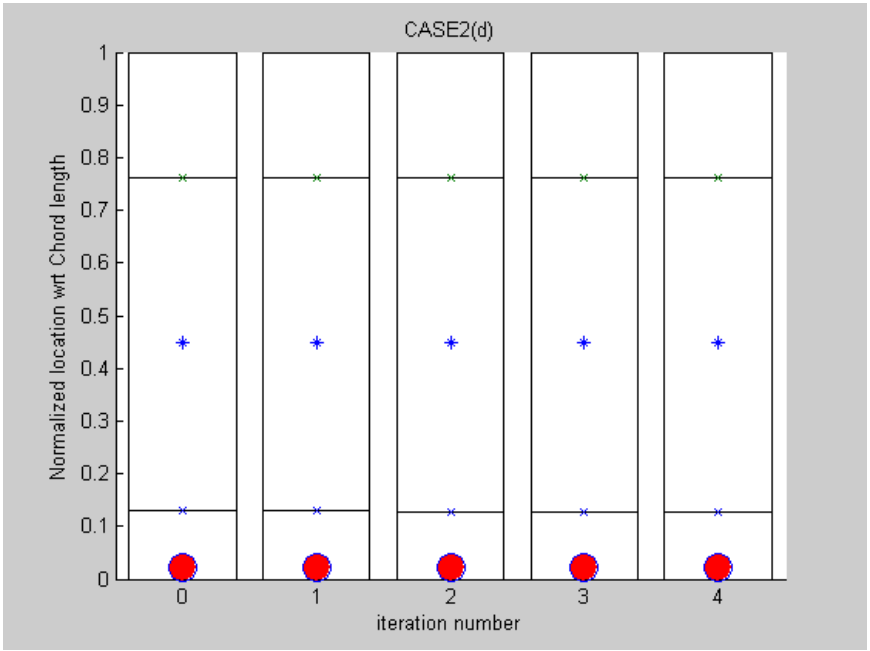

(b)

Figure 3.30. Case T2(d) Optimization history
(a) Objective function convergence history (top) and normalized blade parameters (bottom), corresponding (b) spar location (*), web extension (|), front and rear ballast weights (•), and start and end of active region (- x -), all normalized by chord length.

3.2.4 Comparison of the various ATR-A optimized cases and down selection

As presented in the previous section 3.2.3, there were 8 cases chosen for which optimized solution were found. A summary of them is presented in Table 3.24.

Table 3.24. ATR-A case study summary

	No. of web plies	No. of extra plies at nose	Upper limit of spar location	Active twist rate (deg/m)	Active tip twist angle (deg)
Case T1(a)	3	3	0.85c	2.27	2.61
Case T1(b)		**5**	0.85c	2.52	**2.91**
Case T1(c)		3	**0.45c**	2.21	2.55
Case T1(d)		**5**	**0.45c**	2.47	**2.85**
Case T2(a)	2	3	0.85c	2.37	2.73
Case T2(b)		**5**	0.85c	2.66	**3.07**
Case T2(c)		3	**0.45c**	2.21	2.54
Case T2(d)		**5**	**0.45c**	2.46	**2.84**

Tip twist angle = twist rate * length of active region

Length of active region (m)= 1.1523 = 1.609*(0.943-0.227)

Among those cases, Case T1(b) and Case T2(b) are selected as the recommended ones for further consideration. Those cases show the maximum twist rate at a given number of web plies. Figure 3.31and Figure 3.32 show the cross sectional view for each case.

The filling foam is then implemented in both of these cases. The distorted quad element is fixed in PATRAN, as described in the previous section. As expected, the elastic axis has moved backwards and has ended up near the quarter chord, as summarized in Table 3.26 and Table 3.27. The material properties of the foam are presented in Table 3.25.

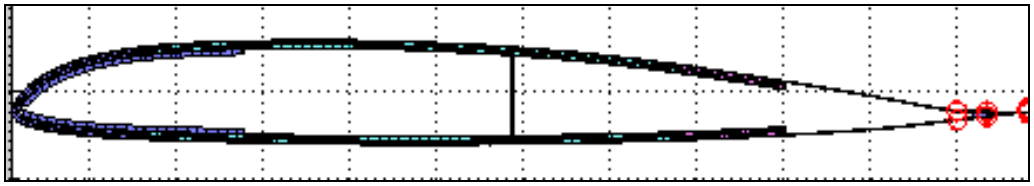

(a)

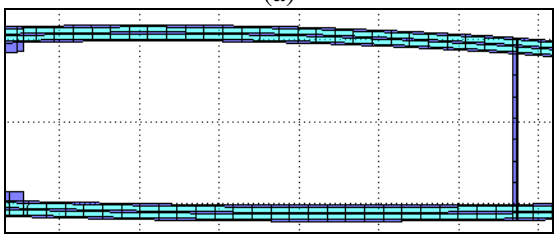

(b)

Figure 3.31. Case T1(b) Cross section layup
(a)whole cross section (b) near end of nose reinforcement and spar location

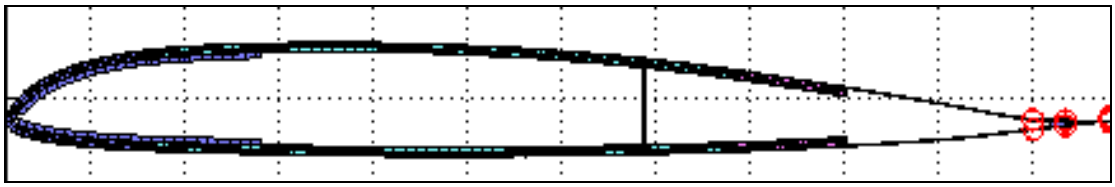

(a)

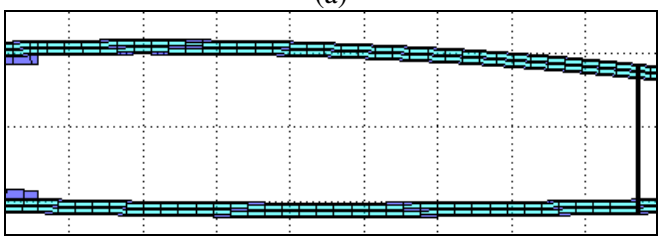

(b)

Figure 3.32. Case T2(b) Cross section layup
(a)whole cross section (b) near end of nose reinforcement and spar location

Table 3.25. Material Properties of the foam

E (MPa)	υ	ρ (kg/m^3)
35	0.26	35

Table 3.26. Case T1(b) before and after the inclusion of foam

Foam implementation	No	Yes
Active start	0.130c	0.130c
Active end	0.761c	0.761c
Ballast weight mass	(0.283, 0.000)	(0.283, 0.000)
Ballast weight location	(0.022c, 0.489c)	(0.022c, 0.489c)
Spar location	0.491c	0.491c
Twist rate (deg/m)	2.52	2.62
1st torsional frequency (1/rev)	4.36	4.46
Blade mass / length (kg/m)	0.870	0.899
Max strain (μm/m)	5500	5490
Center of gravity (CG)	0.260c	0.265c
Elastic axis (EA)	0.191c	0.281c

Table 3.27. Case T2(b) before and after the inclusion of foam

Foam implementation	No	Yes
Active start	0.131c	0.131c
Active end	0.762c	0.762c
Ballast weight mass	(0.284, 0.000)	(0.284, 0.000)
Ballast weight location	(0.022c, 0.575c)	(0.022c, 0.575c)
Spar location	0.577c	0.577c
Twist rate (deg/m)	2.66	2.673
1st torsional frequency (1/rev)	4.36	4.46
Blade mass / length (kg/m)	0.870	0.899
Max strain (μm/m)	5500	5500
Center of gravity (CG)	0.260c	0.265c
Elastic axis (EA)	0.200c	0.281c

3.2.5 Analysis of effect of span-wise design optimization

In this section, the effect of the span-wise design optimization is explored. The cross-sectional layups are designed differently along the blade. The blade is divided into four sections along the span. The first three sections may have active materials while the last section is the passive tip. For the ATR-A cases, the spacial distributions is as follows:

- Section 1: 0.227R to 0.4657R (Active region)
- Section 2: 0.4657R to 0.7043R (Active region)
- Section 3: 0.7043R to 0.943R (Active region)
- Section 4: 0.943R to 1.000R

In each of the sections, a set of design variables are independently defined. Considering manufacturability of the blade, the spar location for each section is set to the same value, which implies in linking the corresponding design variables in each section to a unique one. The remaining design variables are:

- Section 1: active start, active end, ballast weight (2)
- Section 2: active start, active end, ballast weight (2)
- Section 3: active start, active end, ballast weight (2)
- Section 4: active start, active end, ballast weight (2), spar location

Constraints and bounds are shown in Table 3.28. They are the same as used for Case T1(b) for each section, except the lower bound of the active region. Sections 2, 3 and 4 have the lower bound of the active region set to 0.0455c instead of 0.846c, which may provide larger twist actuation. The cross sectional layup is also the same as in Case T1(b). Only section 4, the tip region, has E-glass 0/90 instead of MFC.

Table 3.28. Constraints and bounds for the span-wise optimization case

Elastic Axis (EA)	0.10c < EA< 0.20c
Center of Gravity (CG)	0.20c < CG < 0.26c
Blade mass / length (kg/m)	0.79 < *m* < 0.87
1st torsional frequency (1T)	1T < 5/rev
Local Strain in the worst case loading	1.5xMax strain < ultimate strength of original constituent material
Ballast weight (kg/m)	0.0 <weight < 1.0
Active region	0.084615c (0.0455c) < Loc<0.85c
Spar location	0.3c < $Spar_{loc}$ < 0.85c

Table 3.29. Initial and optimized values for the span-wise optimization case

	Initial	Optimized
Tip twist angle (deg)	3.37	**3.43**
1st torsional frequency (1/rev)	4.32	4.40

Table 3.30. Optimized length of the MFC for the different active sections

	Upper	Lower
Section 1 (mm)	75.0	73.4
Section 2 (mm)	79.0	77.2
Section 3 (mm)	80.6	78.1

Figure 3.34 shows the optimization history of the objective function and constraints. The initial and optimized values of tip twist angle and first torsional frequencies are presented in Table 3.29. Table 3.30 shows the optimized length of the MFC on each active section.

Table 3.31 shows the initial and optimized values for each section, while Figure 3.33 presents the summary of the cross sectional designs at different blade sections.

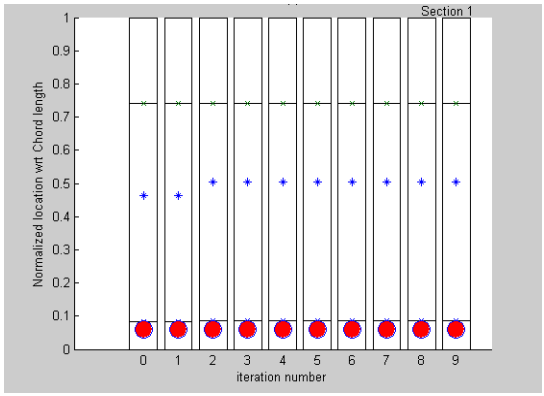

(a) Section 1

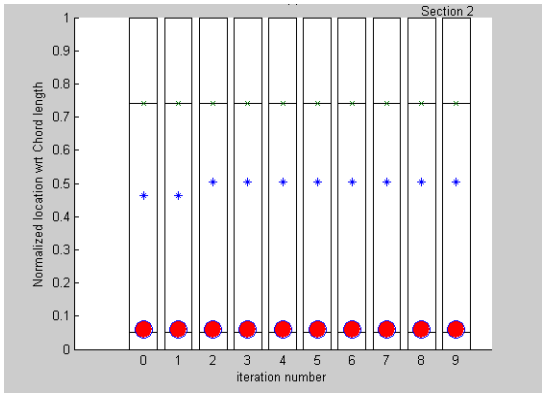

(b) Section 2

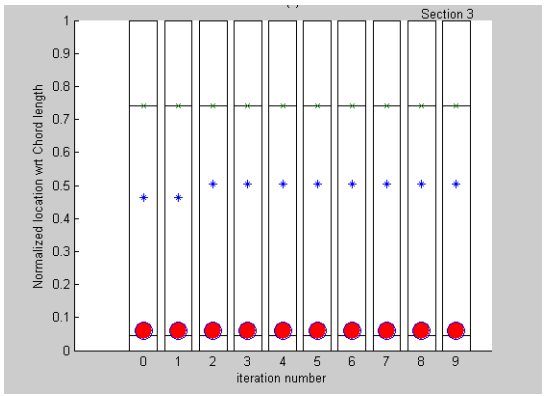

(c) Section 3

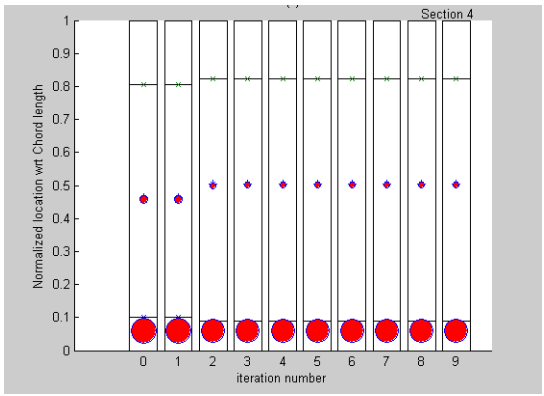

(d) Section 4

Figure 3.33 Span-wise optimization history – cross sectional design

Spar location (*), web extension (|), front and rear ballast weights (●), and start and end of active region (- x -), all normalized by chord length.

For this particular design, the additional freedom brought up by span-wise design variables had only a small impact in the objective function (~2% increase in tip twist) and a small adjustment in the constraints (see

Table 3.31). This came with the additional complexity/cost due to the different actuator sizes required for each section (Table 3.30). The trade is not worthwhile for ATR-A and the design will continue without the subdivision of the active region of the blade.

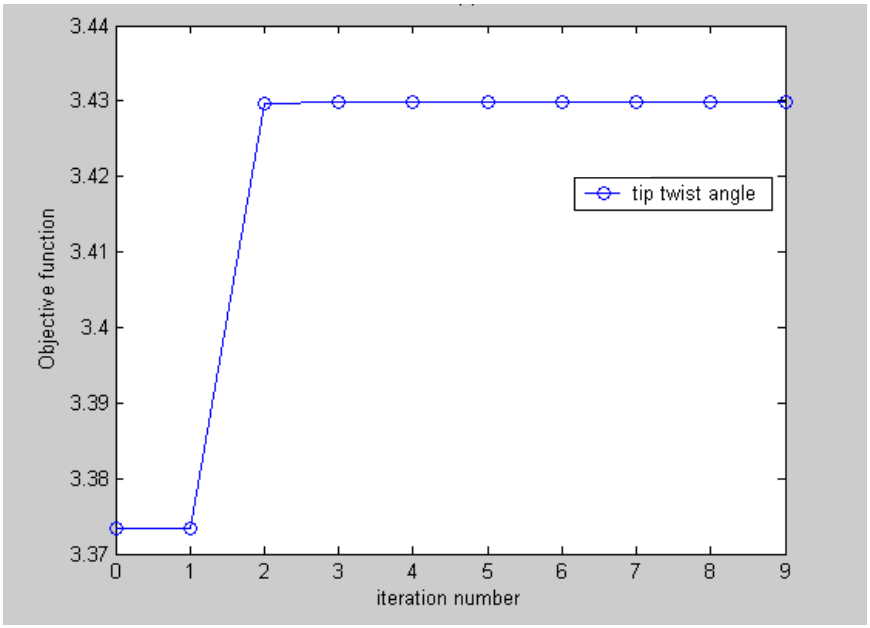

(a)

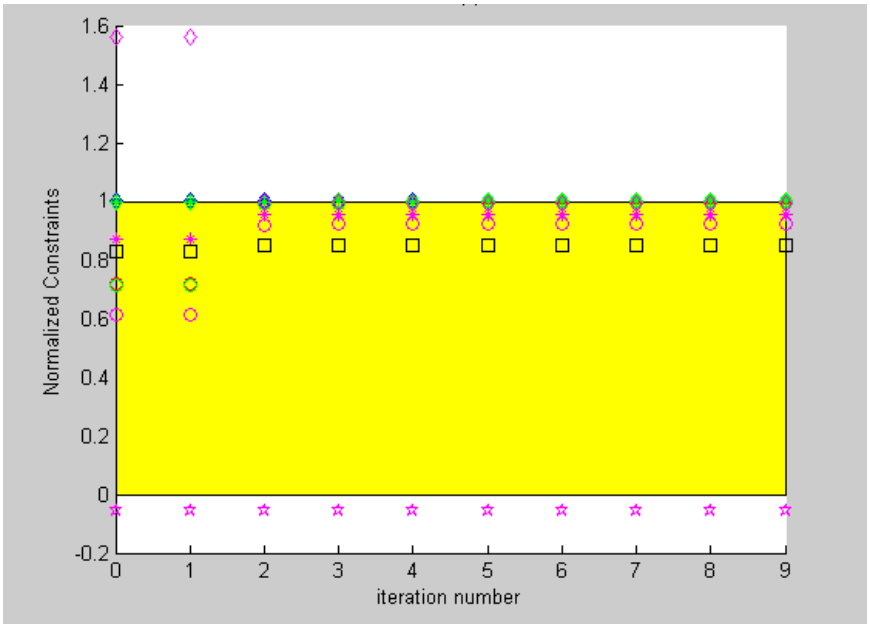

(b)

Figure 3.34. Span-wise Optimization history

(a) Objective function convergence history (b) normalized constraints (*: location of CG, O: location of EA, ◇: blade weight, ⋆: max strain, □: torsional frequency) (Red: section 1, Blue: section 2, Green: section 3, Magenta: section 4)

Table 3.31. Initial and optimized values of the span-wise optimization case

SEC	Parameters	Initial	**Optimized**
1	Active start	0.085c	0.085c
	Active end	0.740c	0.740c
	Ballast weight mass	0.290, 0.000	0.290, 0.000
	Ballast weight location	0.060c, 0.459c	0.060c, 0.501c
	Spar location	0.463c	0.505c
	Blade mass / length (kg/m)	0.870	0.8700
	Center of gravity (CG)	0.260c	0.2600c
	Elastic axis (EA)	0.172c	0.200c
	Max strain (μstrain)	5810	**5810**
2	Active start	0.052c	0.052c
	Active end	0.742c	0.741c
	Ballast weight mass	0.284, 0.000	0.284, 0.000
	Ballast weight location	0.060c, 0.459c	0.060c, 0.501c
	Spar location	0.463c	0.505c
	Blade mass / length (kg/m)	0.870	0.870
	Center of gravity (CG)	0.260c	0.260c
	Elastic axis (EA)	0.172c	0.200c
	Max strain (μstrain)	5480	5500
3	Active start	0.046c	0.046c
	Active end	0.742c	0.742c
	Ballast weight mass	0.282, 0.00	0.282, 0.000
	Ballast weight location	0.060c, 0.459c	0.060c, 0.501c
	Spar location	0.463c	0.505c
	Blade mass / length (kg/m)	0.870	0.870
	Center of gravity (CG)	0.260c	0.260c
	Elastic axis (EA)	0.171c	**0.200c**
	Max strain (μstrain)	**5000**	5012
4	Active start(passive material)	0.100c	0.090c
	Active end(passive material)	0.804c	0.823c
	Ballast weight mass	0.401, 0.000	0.385, 0.099
	Ballast weight location	0.060c, 0.589c	0.060c, 0.501c
	Spar location	0.463c	0.505c
	Blade mass / length (kg/m)	0.915	0.870
	Center of gravity (CG)	0.252c	0.257c
	Elastic axis (EA)	0.161c	**0.192c**
	Max strain (μstrain)	**1280**	1220

3.2.6 Refined ATR-A blade optimum design

(1) Update worst-case loading with previous optimum design

Outer Loop

As mentioned earlier, the aerodynamic load analysis is not included within the optimization loop and is only updated once a converged solution if obtained in the optimization loop (Figure 2.2). Among the optimization cases above, Case T1(b) has been chosen as an optimized design and sent to the outer loop. The aeroelastic analysis was performed on this design, Case T1(b), using CAMRAD II (analysis performed at NASA LaRC/ US Army VTD).

The aeroelastic loadings are provided at every 15˚ azimuthal angle on every given station along the blade for unactuated case and 3P actuated case at 45˚ phase angle. Then the critical load for all six load components is selected by scanning the loads for all azimuthal angles, all radial positions along the blade, and all flight conditions. Figure 3.35 shows an example of the actuated loads associated with the torsional moment 3P, 45 phase angle. The point where the torsional load is maximium is identified: 0.23R and 120˚ angle, and the other five components corresponding to the same point are collected as part of the worst case loading matrix.

Based on the new loads calculated from CAMRAD II with the optimized result of Case T1(b), new maximum load cases were obtained, as exemplified in Table 3.32. In each matrix, the first row represents the loads for the maximum torsion case; the second the maximum for flap-wise bending moment; the third the maximum for lag-wise bending moment; the forth the maximum for axial force; the fifth the maximum for chord-wise shear force; and the sixth the maximum for normal shear force. Maximum loads at other blade locations were also computed and are shown in Appendix 4.

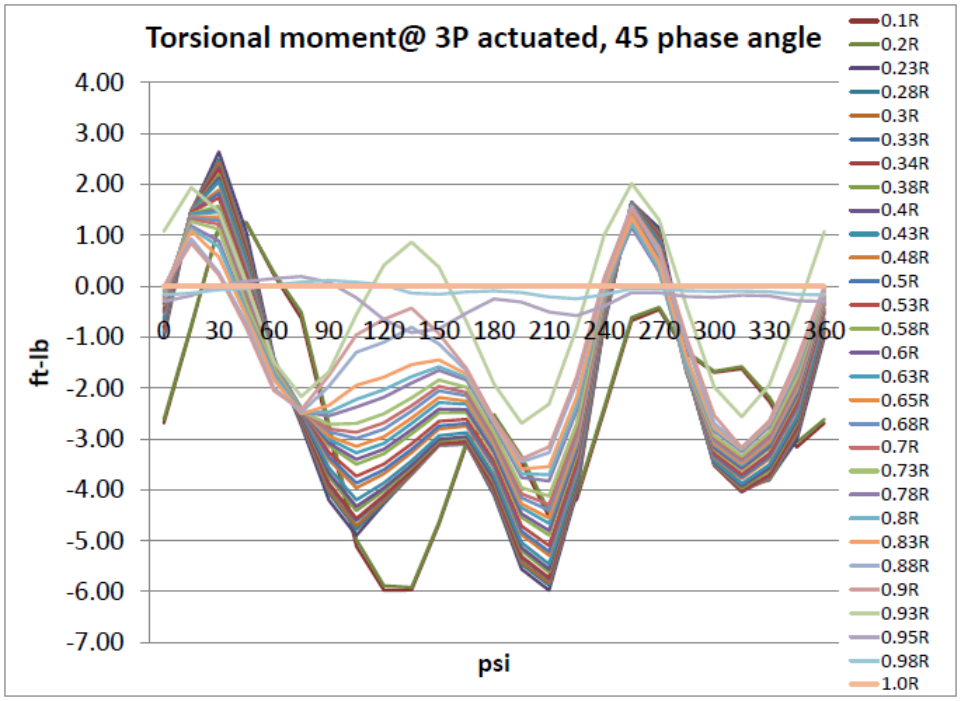

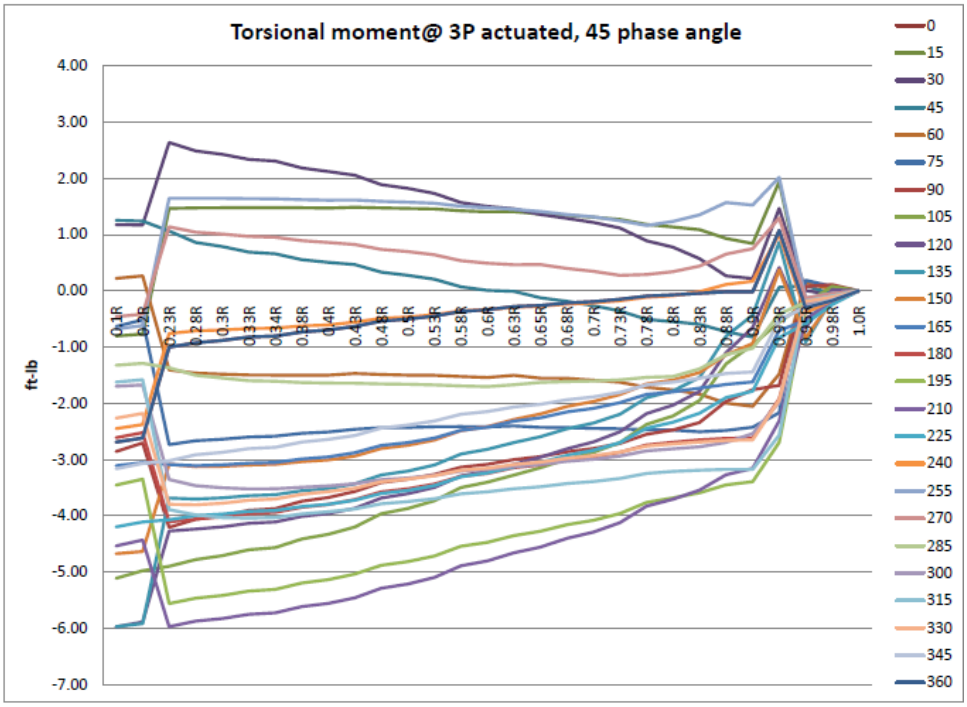

Figure 3.35. Torsional moment at 3P actuated, 45 phase angle

Table 3.32. Updated worst-case loading with optimized design

Max loads for Torsion case (in - lb)

0.1R	0.2R	0.3R	0.4R	0.5R	0.6R	0.7R	0.8R	0.9R	1.0R
-78.4	-77.8	-82.8	-78.4	-73.1	-66.9	-58.9	-49.8	-42.2	0.0
14.4	12.3	29.1	19.6	18.5	-30.3	-2.4	-3.9	5.2	0.0
-14.0	-13.1	14.7	15.0	-5.6	-4.0	-2.6	-1.0	2.0	0.0
-39.5	-38.5	-18.3	-60.1	-55.2	-49.0	-41.0	-15.4	-7.1	0.0
-5.5	-5.0	12.1	-18.0	-5.9	15.6	7.6	3.4	2.6	0.0
-29.4	14.9	9.4	-1.0	-18.9	19.4	16.8	-24.9	2.3	0.0

Max loads for Flap-wise bending case (in -lb)

0.1R	0.2R	0.3R	0.4R	0.5R	0.6R	0.7R	0.8R	0.9R	1.0R
-15.0	-39.8	7.0	10.5	13.9	18.3	23.7	23.3	9.8	0.0
-63.6	-99.6	-60.7	-52.1	-48.9	56.0	80.0	92.8	34.6	0.0
1.3	-18.8	-34.3	-35.4	-26.3	-11.8	8.3	28.0	8.1	0.0
7.4	-12.4	-19.7	9.3	26.5	49.2	66.0	86.5	31.7	0.0
1.2	-34.3	-39.9	-16.1	-2.0	-13.7	34.8	65.1	24.7	0.0
7.1	-98.3	-50.3	1.8	21.3	-8.2	28.7	-6.5	33.9	0.0

Max loads for Lag-wise bending case (in - lb)

0.1R	0.2R	0.3R	0.4R	0.5R	0.6R	0.7R	0.8R	0.9R	1.0R
343.5	113.0	84.2	81.4	61.5	48.5	40.4	41.1	32.8	0.0
123.5	-130.0	-49.8	80.2	70.9	40.1	2.0	-10.5	20.2	0.0
510.9	306.5	313.6	317.3	282.7	232.3	169.0	102.5	45.8	0.0
452.3	241.4	244.7	-2.3	-20.5	-23.9	-13.9	-3.3	17.4	0.0
363.9	88.4	40.9	15.5	-22.4	228.3	-54.0	-18.3	9.7	0.0
505.0	-150.8	-124.3	128.8	-48.6	1.5	-4.4	18.4	15.7	0.0

Max loads for axial shear force case (lb)

0.1R	0.2R	0.3R	0.4R	0.5R	0.6R	0.7R	0.8R	0.9R	1.0R
1394.9	1319.9	1261.6	1182.0	1079.7	954.6	806.8	634.4	436.6	0.0
1337.8	1266.8	1214.2	1146.2	1066.5	955.7	810.2	640.2	444.9	0.0
1400.1	1323.1	1262.4	1180.2	1077.4	949.7	800.0	628.6	435.8	0.0
1404.0	1327.8	1267.8	1187.7	1086.2	961.6	813.9	642.7	447.6	0.0
1381.0	1305.5	1247.4	1136.7	1039.3	947.1	778.3	613.8	424.8	0.0
1402.0	1260.9	1205.9	1178.0	1080.7	925.2	782.0	621.5	445.8	0.0

Max loads for chord shear force case (lb)

0.1R	0.2R	0.3R	0.4R	0.5R	0.6R	0.7R	0.8R	0.9R	1.0R
23.5	16.7	3.9	1.9	0.2	-1.2	-2.2	-2.1	-0.8	0.0
21.5	12.4	3.6	3.2	1.3	-1.8	-3.7	-7.9	-5.8	0.0
17.0	12.1	1.0	2.4	4.1	6.1	7.2	6.0	3.1	0.0
17.8	12.8	1.5	2.3	-0.5	-3.2	-5.3	-6.9	-6.5	0.0
30.2	21.9	7.7	-6.0	-5.2	6.5	-7.8	-9.3	-9.1	0.0
16.9	8.9	-2.6	1.1	-0.8	-0.8	-2.7	-5.2	-7.3	0.0

Max loads for normal shear force case (lb)

0.1R	0.2R	0.3R	0.4R	0.5R	0.6R	0.7R	0.8R	0.9R	1.0R
-6.4	2.7	0.4	-1.4	-0.3	-0.9	-0.4	-1.9	-8.6	0.0
-0.1	10.4	1.6	0.7	-0.4	1.4	3.5	-2.4	-18.1	0.0
-11.6	-4.8	-1.1	0.9	1.7	2.4	3.5	0.7	-9.2	0.0
-7.9	-3.7	-0.2	0.4	2.4	1.6	1.2	-2.4	-17.3	0.0
-5.1	-2.7	-1.6	0.6	2.4	2.6	4.9	1.1	-16.1	0.0
-11.8	11.4	2.6	2.7	3.7	4.7	7.0	-3.6	-18.5	0.0

Inner Loop

Then the optimization was run again with a layup similar to Case T1(b) (Figure 3.31) but with updated loads as in Table 3.32. Constraints and design variables are kept the same as Case T1(b) and are shown on Table 3.33 for completeness. This case will be known as Case Tu. The initial and optimized values are presented in Table 3.34. shows the optimized layup sketch of this case, while Figure 3.36 shows the optimization history. Since the initial values used on the optimization process were the optimized solution for Case T1(b), only a few iterations were needed in order to reach convergence. The results of the application of the new loads on the design show that the MFC plies move toward the leading edge from 0.1296c to 0.1051c, which produces an increment in the active tip twist angle of 6.5% (3.10˚ instead of 2.91˚). This is due to a slight decrease of the design loads, which have been used as the worst loading from the previous iteration.

Table 3.33.Constraints and bounds for Case Tu

Elastic axis (EA)	0.10c < EA< 0.20c
Center of gravity (CG)	0.20c < CG < 0.26c
Blade mass / length (kg/m)	0.79 < *m* < 0.87
1st torsional frequency (1T)	1T < 5/rev
Local Strain in the worst loading case	1.5×Max strain < ultimate strength of original constituent material
Ballast weight (kg/m)	0.0 <weight < 1.0
Active region	0.084615 c< Loc<0.85c
Spar location	0.3c < $Spar_{loc}$ < 0.85c

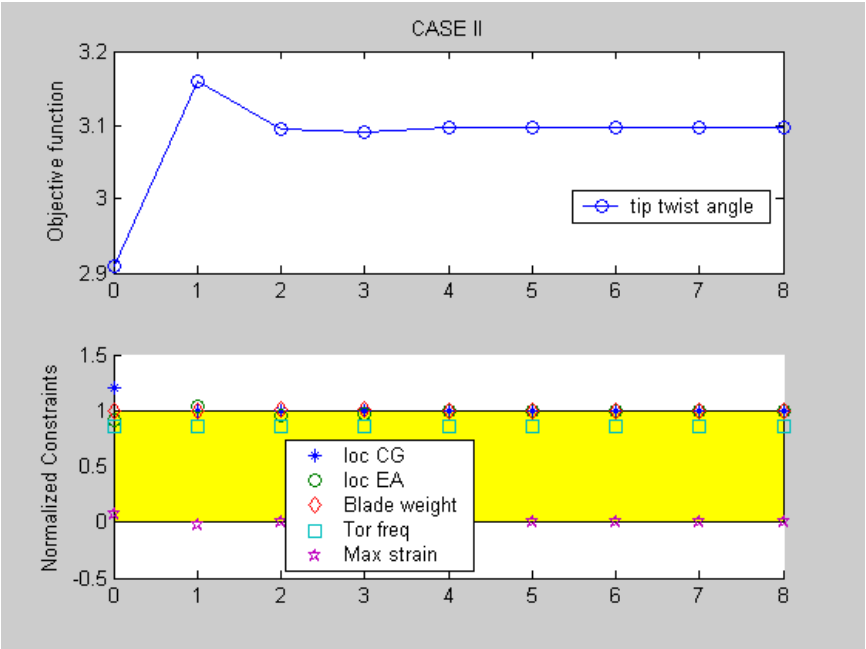

(a)

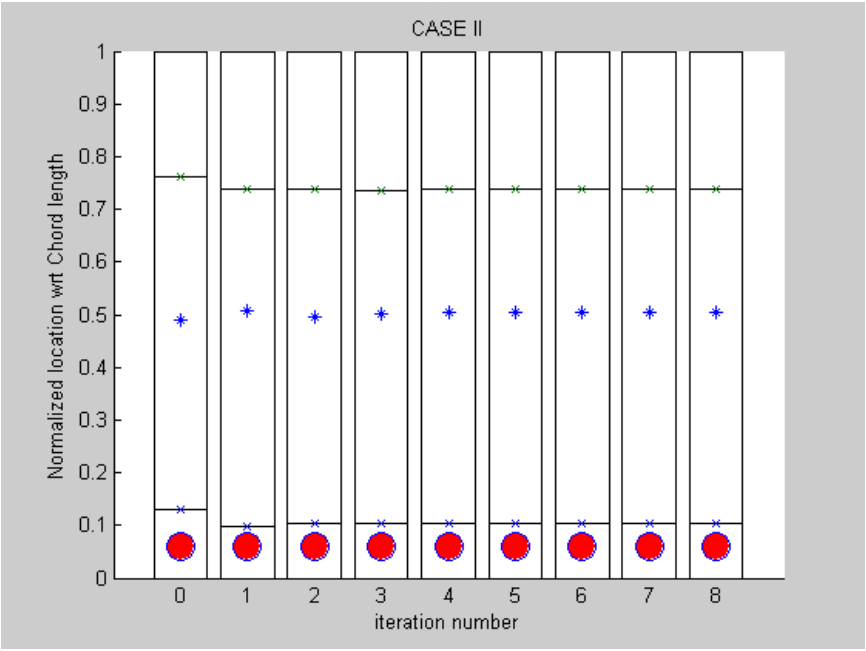

(b)

Figure 3.36. Case Tu Optimization history

(a) Objective function convergence history (top) and normalized blade parameters (bottom); (b) spar location (*), web extension (|), front and rear ballast weights (●), and start and end of active region (- x -), all normalized by chord length.

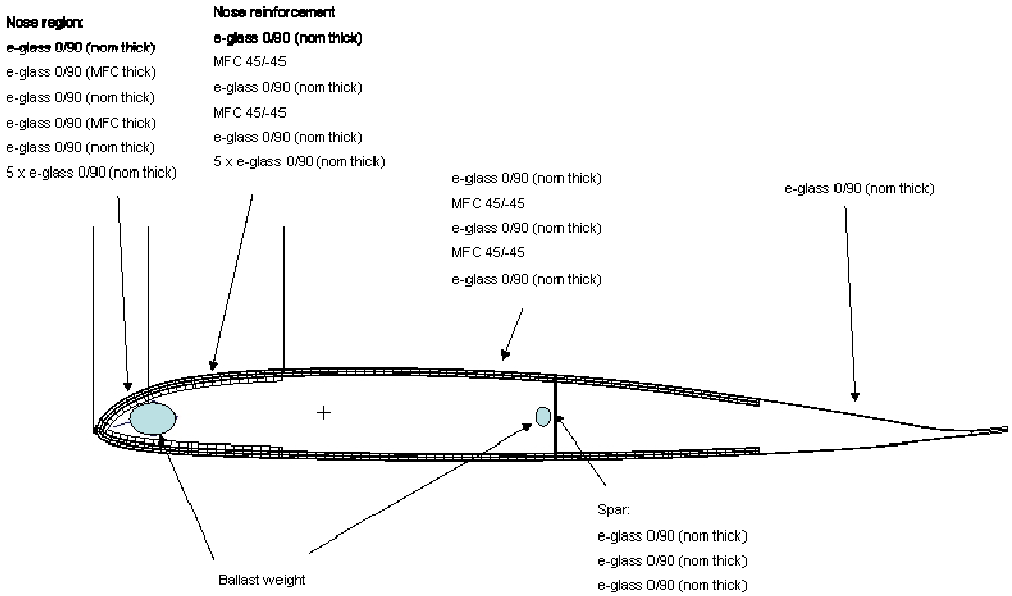

Figure 3.37. Optimized Layup result for Case Tu

Table 3.34. Case Tu Initial and optimized results

	Initial	Optimized
Active start	0.127c	0.105c (-19%)
Active end	0.761c	0.737c (-3%)
Ballast weight mass	(0.283, 0.000)	(0.295, 0.000)
Ballast weight location	(0.060c, 0.487c)	(0.060c, 0.501c)
Spar location	0.491c	0.505
Tip twist angle (deg)	2.91	3.10 (6.5%)
1st torsional frequency (1/rev)	4.42	4.44
Blade mass / length (kg/m)	0.870	0.870
Max strain	5100	5500
Center of gravity (CG)	0.272c	0.260c (-4.5%)
Elastic axis (EA)	0.191c	0.200c

(2) **Analysis of the effect of using stiffer foam**

The effect of placing stiffer foam on the D-spar region of the cross section is studied in this section. Properties of different foam placed on the cross section are presented in Table 3.35. Different cases were run based on the Case Tu layup shown in Figure 3.37, and they are summarized in Table 3.36. Rohacell 31 IG and 71 IG are foam used on ATR-I on the fairing region of the cross section. The value of υ is not given by the manufacturer. The manufacturer provides E and G and assuming an isotropic material the value of υ was computed. Case Tu1 represents a section with both regions of the cross section having the same foam (Rohacell 31 IG.) Case Tu2 presents the same foam distribution used in ATR-I, and in Case Tu3 much stiffer and denser foam is used on the D-spar section (Rohacell 200 WF.) In all the cases, the new set of loads presented in the first section of this report is used.

Table 3.35. Mechanical properties of foam

Commercial name	E (MPa)	G (MPa)	υ	ρ (kg/m^3)
Rohacell 31 IG	36.0	13.0	0.385	32.0
Rohacell 71 IG	81.2	29	0.400	75.0
Rohacell 200 WF	350	150	0.167	205

Table 3.36. Cases analyzed in foam study

	D-spar	fairing
Case Tu1	31 IG	31 IG
Case Tu2	71 IG	31 IG
Case Tu3	200 WF	31 IG

The results for Case Tu1 are presented in Table 3.37. When light foam is used in both regions of a cross section it is observed that actuation only increased 1% from 3.1^o to 3.13^o, while also a slight reduction in max shear strain value is obtained. The CG is slightly moved aft (2%) while the EA is changed by 42% toward the back of the airfoil, locating it around 0.28c.

Table 3.37. Comparison with foam implementation for Case Tu1

	without foam	with foam
Active start	0.105c	0.105c
Active end	0.737c	0.737c
Ballast weight mass	(0.295, 0.000)	(0.295, 0.0)
Ballast weight location	(0.060c, 0.501c)	(0.060c, 0.501c)
Spar location	0.505c	0.505c
Tip twist angle (deg)	3.10	3.13 (1%)
1st torsional frequency (1/rev)	4.44	4.46 (0.5%)
Blade mass / length (kg/m)	0.87	0.89 (2.8%)
Max strain (με)	5500	5430 (-1.3%)
Longitudinal strain (με)	2600	2290 (-11%)
Lateral strain (με)	2530	2200 (-13%)
Shear strain (με)	5500	5430 (-1%)
Center of gravity (CG)	0.260c	0.265c (2%)
Elastic axis (EA)	0.200c	0.283c (42 %)

For Case Tu2 and Case Tu3, an initial optimized result was obtained with a lower value for the blade weight upper bound value (0.84 and 0.80 kg/m respectively), such that, when the foam is implemented, the weight upper limit is not violated. All other constraints were kept at their original values (Table 3.34). By reducing the upper bound of the blade mass per unit length, a reduction on the twist actuation is observed. This reduction comes as a consequence of the reduction on the length of the active ply to compensate for the reduction of ballast weight all in order to keep the center of gravity position constant.

Results for Case Tu2 are presented in Table 3.38. Increasing the density of the foam placed on the D-spar region produces an increase of twist actuation of 1% and at the same time the maximum shear strain is reduced by 2% from 5500 to 5390με. The first torsional frequency changes from 4.47 to 5.35 /rev (20%). The center of gravity is changed from 0.260c to 0.267c (3%), while the elastic axis moves from 0.200c to 0.279c (39%).

Table 3.38. Comparison with foam implementation for Case Tu2

	without foam	with foam
Active start	0.105c	0.105c
Active end	0.727c	0.727c
Ballast weight mass	(0.274, 0.000)	(0.274, 0.000)
Ballast weight location	(0.060c, 0.499c)	(0.060c, 0.499c)
Spar location	0.504	0.504
Tip twist angle (deg)	3.09	3.10 (1%)
1st torsional frequency (1/rev)	4.47	5.35 (20%)
Blade mass / length (kg/m)	0.840	0.886 (5.5%)
Max strain (με)	5500	5390 (-2%)
Longitudinal strain (με)	2630	2300 (-12%)
Lateral strain (με)	2550	2200 (-14%)
Shear strain (με)	5500	5390 (-2%)
Center of gravity (CG)	0.260c	0.265c (2%)
Elastic axis (EA)	0.200c	0.279c (39%)

The comparison between Case Tu1 and Case Tu2 shows that the effect on the variables is similar with the exception of the first torsional frequency, which for Case Tu2 increased by 20% while in Case Tu1 is not significantly altered.

The results for Case Tu3 are presented in Table 3.39. Even though using stiffer and denser foam on the D-spar region slightly reduces the actuation by 1%, it has a significant effect on the maximum strain reducing it from 5500 to 5120με. Similar to Case Tu2, the first torsional frequency increases from 4.52 to 5.54 /rev. The center of gravity is changed by 3% (from 0.260c to 0.267c) while the elastic axis moves from 0.200c to 0.300c (50%).

This analysis shows that placing denser and stiffer foam on the D-spar region of the cross section helps to reduce the strain generated on the cross section without significantly affecting the actuation obtained. Independent of the density of the foam, the location of the CG is not affected, while the elastic axis changes at around 50% (approximately 0.2c to 0.3c). The density of the foam may affect the value of the first torsional frequency up to 20%.

Since using Rohacell 200WF provides a significant reduction in strain (between 7% and 12%) and a reduction on the ballast weight needed in the leading edge without a significant effect on twist actuation (-1%), Case Tu3 is selected and considered further. For this case, the length of the MFC plies with active fiber on it is 57.0 mm and 58.3 mm for the upper and lower portion of the airfoil, respectively.

Table 3.39. Comparison with foam implementation for Case Tu3

	without foam	with foam
Active start	0.104c	0.104c
Active end	0.709c	0.709c
Ballast weight mass	(0.248, 0.0)	(0.248, 0.0)
Ballast weight location	(0.06c, 0.496c)	(0.06c, 0.496c)
Spar location	0.500	0.500
Tip twist angle(deg)	3.07	3.03 (-1%)
1^{st} torsional frequency (1/rev)	4.52	5.54 (23%)
Blade mass / length (kg/m)	0.800	0.906 (13%)
Max strain (με)	5500	5120 (-7%)
Longitudinal strain (με)	2650	2330 (-12%)
Lateral strain (με)	2570	2260 (-12%)
Shear strain (με)	5500	5120 (-7%)
Center of gravity (c)	0.260	0.267 (3%)
Elastic axis (c)	0.200	0.299 (50%)

Table 3.40 presents properties of all three cases when the foams are included accordingly. Among these, Case Tu2 is selected since it has relatively higher tip twist angle with lower maximum strain and the elastic axis is nearer to the quarter chord. Moreover, it is using the materials that has heritages from ATR-I blade.

Table 3.40. Comparison of with foam implementation cases

	Case Tu1 With foam	Case Tu2 With foam	Case Tu3 With foam
Active start	0.1051c	0.1048c	0.1038c
Active end	0.7373c	0.7265c	0.7088c
Ballast weight mass	(0.295, 0.0)	(0.274, 0.0)	(0.248, 0.0)
Ballast weight location	(0.06c, 0.501c)	(0.06c, 0.499c)	(0.06c, 0.496c)
Spar location	0.505c	0.504	0.500
Tip twist angle (deg)	**3.13**	**3.10**	3.03
1st torsional frequency (1/rev)	4.46	5.35	5.54
Blade mass / length (kg/m)	0.894	0.888	0.906
Max strain (με)	5430	**5390**	5120
Longitudinal strain (με)	2290	2300	2330
Lateral strain (με)	2200	2200	2260
Shear strain (με)	5430	5390	5120
Center of gravity (CG)	0.265c	0.265c	0.267
Elastic axis (EA)	0.283c	**0.279c**	0.299

3.2.7 Ballast mass

Figure 3.38 shows a schematic cross sectional view of two ballast mass implementations. For Case Tu3, a ballast weight of 0.2475 kg/m is needed at the leading edge of the airfoil. Tungsten is usually introduced as the material for the ballast mass. The density of tungsten is 19.3 kg/m^3.

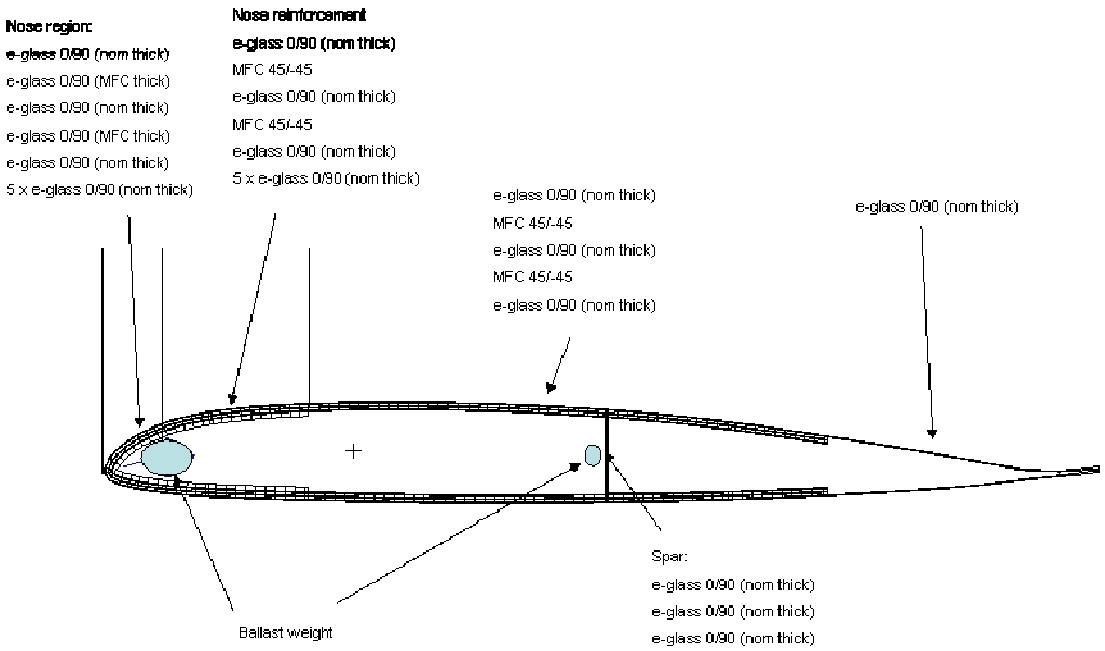

Figure 3.38. Cross section sketch for layup with two ballast masses

There can be several different approaches to place this ballast weight. The first one is to use a tungsten rod of 5/16" diameter and machine it to give the shape of the airfoil up to 6.6 mm from the leading edge. This would be a similar approach as the one used for the ATR-I prototype blade. The ATR-I blade used a tantalum rod of 1/4" diameter. This is presented in shaded area on the schematic diagram showed in Figure 3.39 (Shin 1999). Another possibility is to use a collection of tungsten rods with smaller diameters and to arrange them in the region close to the leading edge. One possible configuration would be to use seven tungsten rods of 1.5 mm in diameter together with two of 0.5 mm as shown in Figure 3.40(a) and (b). The option shown in Figure 3.40 (a) has a centroid located at 6 mm (0.05c) from the leading edge and it goes from 3 mm up to 9 mm from the leading edge, while the one shown in Figure 3.40 (b) has the centroid at 4.75 mm (0.04c) and it goes from 1 mm up to 9 mm from the leading edge. Notice that the value used in Case Tu3 for the location of the ballast weight is 0.06c. The third approach is to use a tungsten compound and mix-up with paste to meet a certain density and make in a certain shape such as depicted in Figure 3.41.

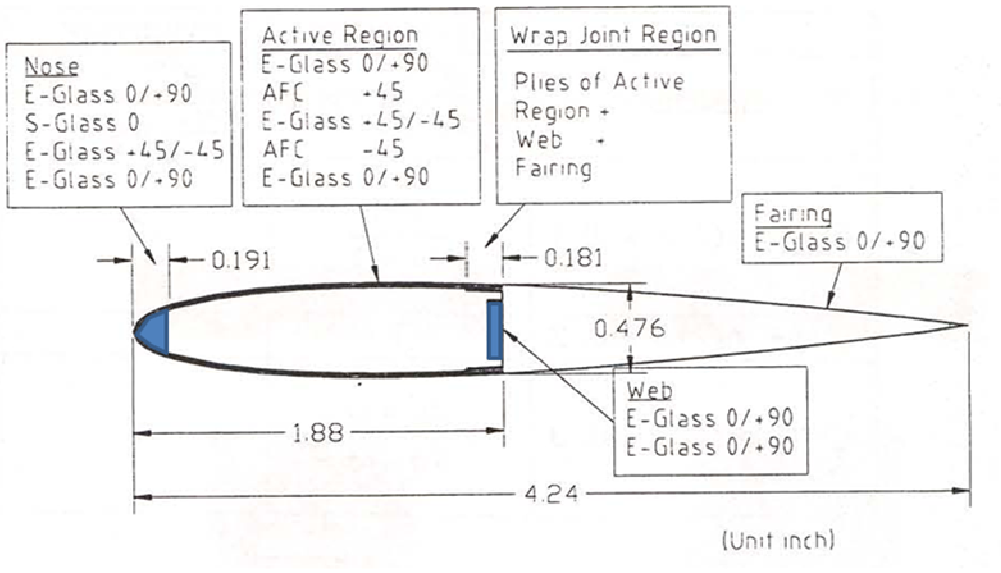

Figure 3.39 Schematic diagram of the ATR-I blade design (Shin 1999)

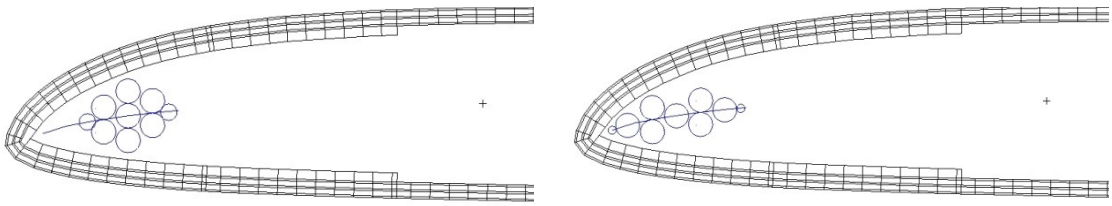

(a) (b)

Figure 3.40. Position of ballast rods on leading edge of airfoil

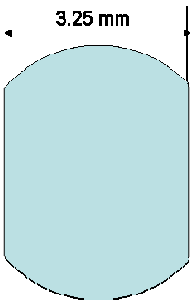

Figure 3.41. Possible geometry of ballast mass

3.2.8 Strain Analysis

The strain analysis on the proposed design after the optimization indicated that the maximum torsional strain occurs on the one-ply fairing and the web. To alleviate that, adjustments to the optimized case are introduced as in Table 3.41 and the effects of the changed constraints and the objective function are studied.

- CASE S1: Original ATR-A baseline
- CASE S2: Additional two Glass/Epoxy plies added to the web (butt ending).
- CASE S3: Extension of innermost 0/90 Glass/Epoxy ply from the active region going all the way to the end of the fairing.
- CASE S4: Combination of CASE S2 and CASE S3.

Table 3.41. Case description

	CASE S1	CASE S2	CASE S3	CASE S4
Thickness of spar (mm)	0.114× *3*	0.114× 5	0.114× 3	0.114× 3
Thickness of the TE (mm)	0.114× *1*	0.114× *1*	0.114× *2*	0.114× *2*

Strain analysis on torsional strain per unit torque was performed to find the maximum strain points. Table 3.42 shows the common properties for these cases. CASE S1 serves the baseline for comparison of other cases. Table 3.55 in section 3.2.9 shows the detailed values for CASE S1, which is the baseline for comparison of other cases. The results are summarized in Table 3.43, Table 3.44 and Table 3.45. Figure 3.42 through Figure 3.45 present the distribution of the strain due to the unit torque application. The hot spots in CASE S1 (baseline) were the one-ply fairing (35 με/in-lb) and the web (27 με/in-lb). CASE S2 reduces the fairing strain by 7% and the web by 26%. CASE 3 reduces the fairing strain by 14% and the web by 10%. CASE S4 reduces the fairing strain by 18.5% and the web by 22%. Adding the trailing edge (fairing) ply (CASE S3) reduces the twist actuation by ~2% while adding plies to the web (CASE S2) improves the actuation (in this case, ~0.5%). The combined modifications (CASE S4) present a reduction of ~1% from the baseline CASE S1.

For all cases, the center of gravity is basically unaffected. It moved aft but on the order of 3% from the original position, or 0.8% chord. The elastic axis is the variable affected most. It moved ~8% of its original value aft (or 2.25% of chord). Small changes are noticed on frequencies but nothing was significant. Then, the biggest negative impact is associated with the elastic axis position. Actuation is basically unaffected (Table 3.45) and the torsional strain per unit torque is reduced at the hot spots (Table 3.44). Though the adjustment reduced the strain at hot spots, by adding the plies to the web or the trailing edge, there also showed some negative effects in mass per unit length and the location of the elastic axis. Since the hot spots in the CASE S1 still satisfies the strain allowable, that case, which is the original ATR-A baseline is kept as a final model.

Table 3.42. Common properties for sections 0, 1 & 2

Thickness of nose part (outer, inner) (mm)	0.114× (3, 3)
Thickness of nose reinforcement (before, after active start) (mm)	0.114× (4, 5)
Space around ballast weight (mm)	0.114× 3
Active start (upper, bottom)	(0.092c, 0.092c)
Active end (upper, bottom)	(0.609c, 0.610c)
Electrode start(upper, bottom)	(0.609c, 0.610c)
Electrode end (upper, bottom)	(0.709c, 0.710c)
End of nose reinforcement	0.1920c
Spar location	0.5040

Table 3.43. Cross sectional properties (with foam)

Section		CASE S1			CASE S2			CASE S3			CASE S4		
		Mass	CG loc	EA loc	Mass	CG loc	EA loc	Mass	CG loc	EA loc	Mass	CG loc	EA loc
		[kg/m]	[%c]	[%c]	[kg/m]	[%c]	[%c]	[kg/m]	[%c]	[%c]	[kg/m]	[%c]	[%c]
0	0.227~0.847R	0.88	25.60	28.50	0.88	25.70	30.15	0.89	26.29	29.33	0.89	26.38	30.74
1	0.847~0.938R	1.50	19.38	28.50	1.51	19.45	30.15	1.51	19.83	29.33	1.52	19.89	30.74
2	0.938~0.943R	1.63	25.12	28.50	1.63	25.17	30.15	1.64	25.50	29.33	1.64	25.55	30.74

Table 3.44. Strain values for worst case loads

	CASE S1	CASE S2	CASE S3	CASE S4
Thickness of spar (mm)	0.114× *3*	0.114× 5	0.114× 3	0.114× 3
Thickness of the TE (mm)	0.114× *1*	0.114× *1*	0.114× *2*	0.114× *2*
Max strain (με)	5160	5150	5170	5160
Longitudinal strain (με)	2200	2170	2080	2050
Lateral strain (με)	1930	1920	1910	1910
Shear strain (με)	5160	5150	5170	5160

Table 3.45. Blade actuation properties

	CASE S1	CASE S2	CASE S3	CASE S4
Thickness of spar (mm)	0.114 × *3*	0.114× 5	0.114× 3	0.114× 3
Thickness of the TE (mm)	0.114 × *1*	0.114× *1*	0.114× *2*	0.114× *2*
Tip twist angle (deg)	3.05	3.07	3.00	3.01

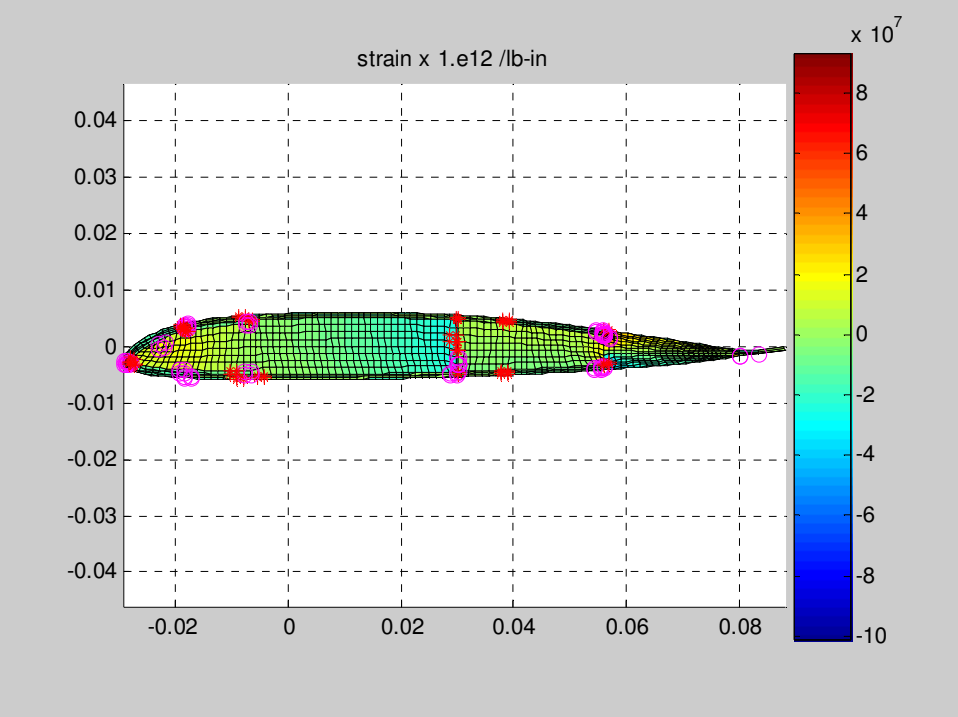

Figure 3.42. Case S1 Sectional distribution of strain due to unit torque (Γ_{12} per in-lbf)

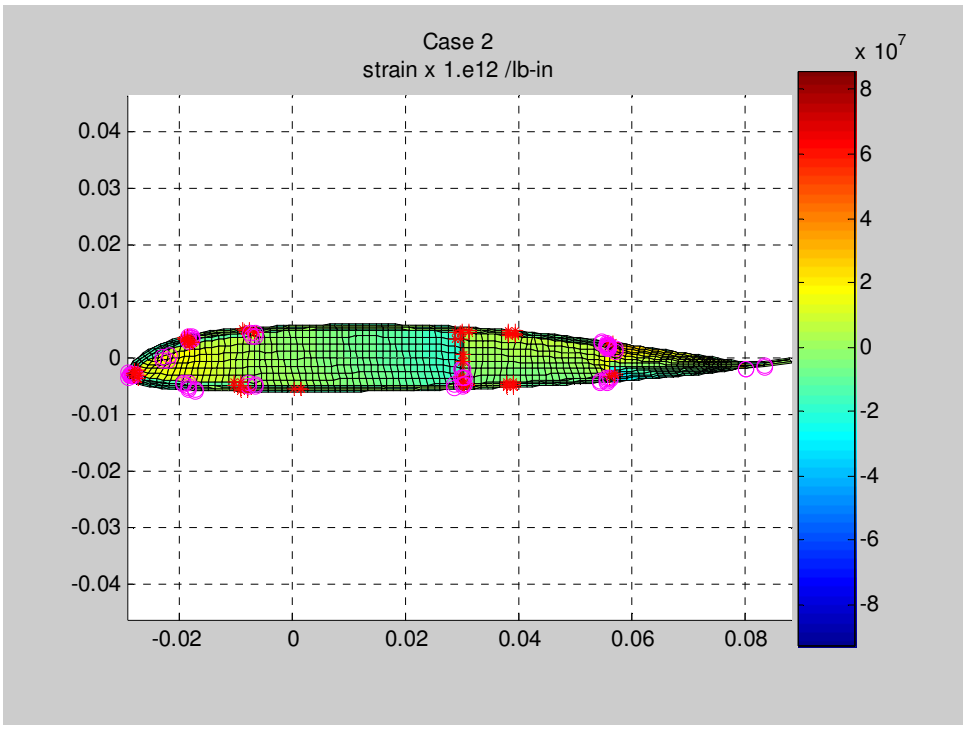

Figure 3.43. Case S2 Sectional distribution of strain due to unit torque (Γ_{12} per in-lbf)

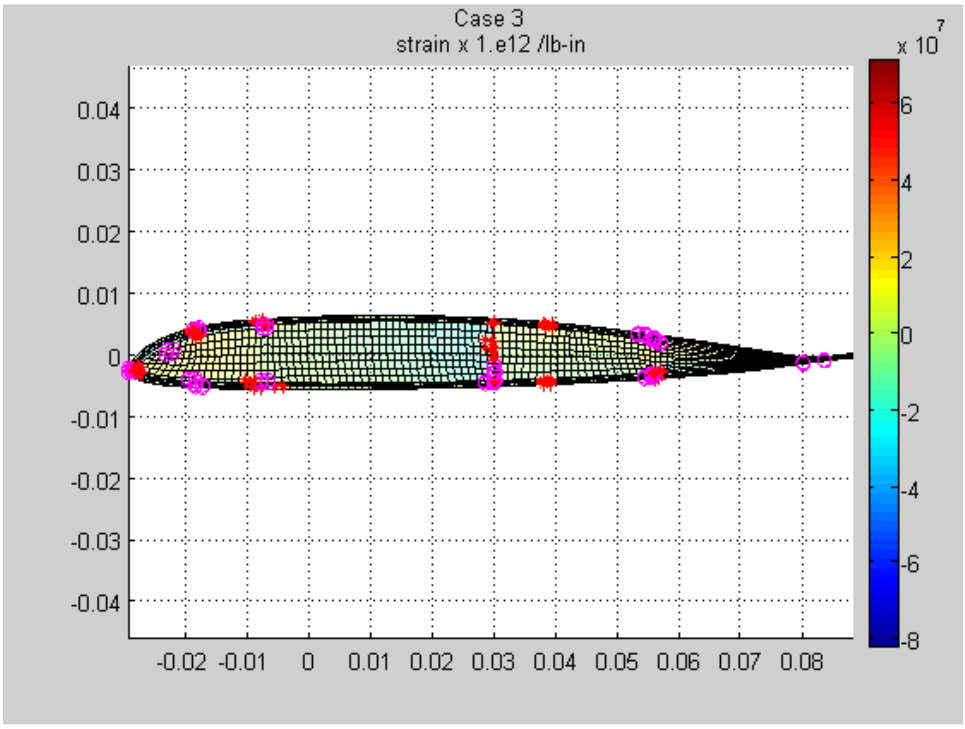

Figure 3.44. Case S3 Sectional distribution of strain due to unit torque (Γ_{12} per in-lbf)

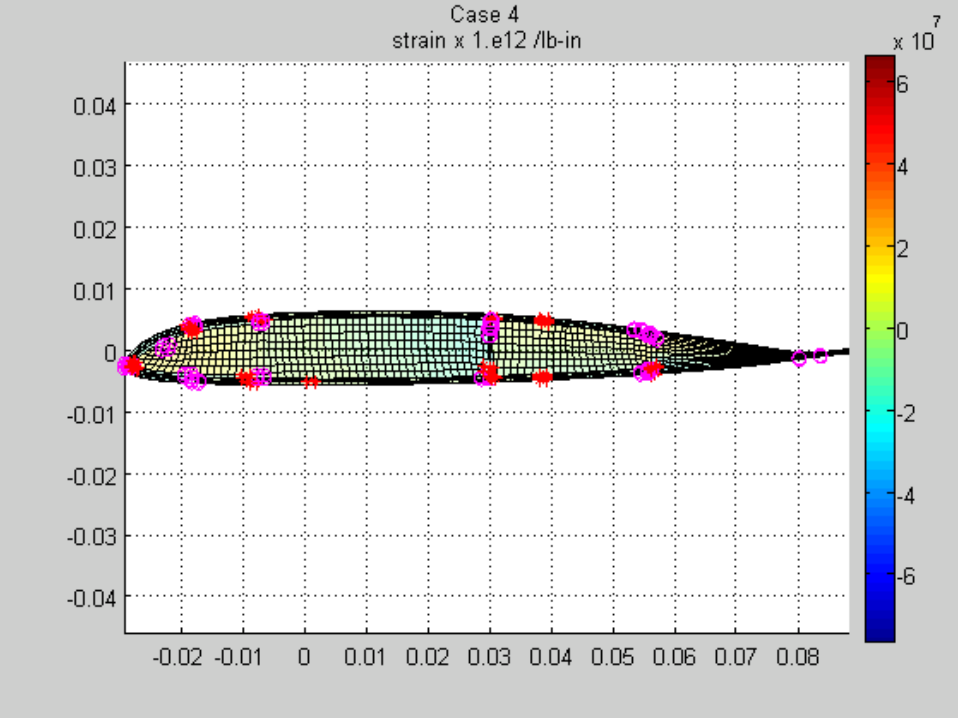

Figure 3.45. Case S4 Sectional distribution of strain due to unit torque (Γ_{12} per in-lbf)

3.2.9 Refining the ATR-A Design

In this section, the study focused on the refinement of Case Tu2 to account for practical manufacturing limitations and its impact on the cross section properties of the active blade. Properties of the baseline materials and the commercially available materials are shown in Table 3.47 and Table 3.46, respectively. The study resulted in a small adjustment to the cross sectional parameters.

Table 3.46. Commercially available material properties provided by manufacturer

	E-Glass	Graphite IM7	Rohacell 31 IG	Rohacell 71 IG
Remark	Resin (F-155)	Root/Resin (SP 381)	Fairing	D-spar
Weave	Fabric	Uni-tape		
Thickness (mm)	0.12	0.14	-	-
Density (kg/m3)	1716	1550	32	75
E11 (GPa)	20.7	165	0.036	0.092
E22 (GPa)	20.7	8.3	-	-
v12	0.13	0.34	0.385	0.04
G12 (GPa)	4.1	4.3	0.013	0.029

Table 3.47. Baseline material properties

	MFC	E-Glass	Graphite IM7 (root)	Kapton	Electrode model	Rohacell 31 IG	Rohacell 71 IG
Remark		Resin F-155	Resin SP 381			Fairing	D-spar
Weave	-	Fabric	Uni-tape				
Thickness (mm)	0.315	0.114	0.1397	-	0.315	-	-
Density (kg/m^3)	4480	1716	1550	1100	1531	32	75
E_{11} (GPa)	20.0	19.3	142	1.0		0.036	0.0812
E_{22} (GPa)	12.3	19.3	8.3	1.0		-	-
ν_{12}	0.291	0.148	0.34	0.3		0.385	0.04
G_{12} (GPa)	3.78	4.1	4.9	0.7		0.013	0.029
d_{11} (m/V) [3]	3.9×10^{10}	-	-	-	-	-	-
d_{12} (m/V)	-1.9×10^{10}	-	-	-	-	-	-
t_{elect} (mm)	0.43	-	-	-	-	-	-
Q_{11} (GPa)	21.10	19.73		1.10	14.14		
Q_{12} (GPa)	3.78	2.92		3.30	2.14		
Q_{22} (GPa)	12.98	19.73		1.10	14.14		
Q_{33} (GPa)	3.78	4.10		0.70	3.10		
X_t (μstrain)	3000	15000	15000	10000	10000	10000	10000
Y_t (μstrain)	3000	10000	10000	10000	10000	10000	10000
S (μstrain)	3000	10000	10000	10000	10000	10000	10000
X_c (μstrain)	3000	10000	10000	10000	10000	10000	10000
Y_c (μstrain)	5500	10000	10000	10000	10000	10000	10000

(1) **Main blade layup**

The main blade layup is shown in Figure 3.46. Figure 3.47 is a close up of the layup near the ballast rod and presents how the additional mass would be integrated to the nose region. The cross sectional constants for this case (with and without foam) are presented in Table 3.49.

[3] Computed at aprox. 1250 V peak -to-peak to produce 1100 μstrain peak-to-peak

Table 3.49 also compares those properties with the cases when the material properties are adjusted with commercially available ones. After the foam is included, the ballast weight is increased to move the CG forward without violating the blade weight constraint. Table 3.48 presents the geometric properties of the active layer. The adjusted design has virtually the same active tip twist as Case Tu2. The mass and stiffness matrices as well as the actuation vector (SI units) are shown in Appendix 5.

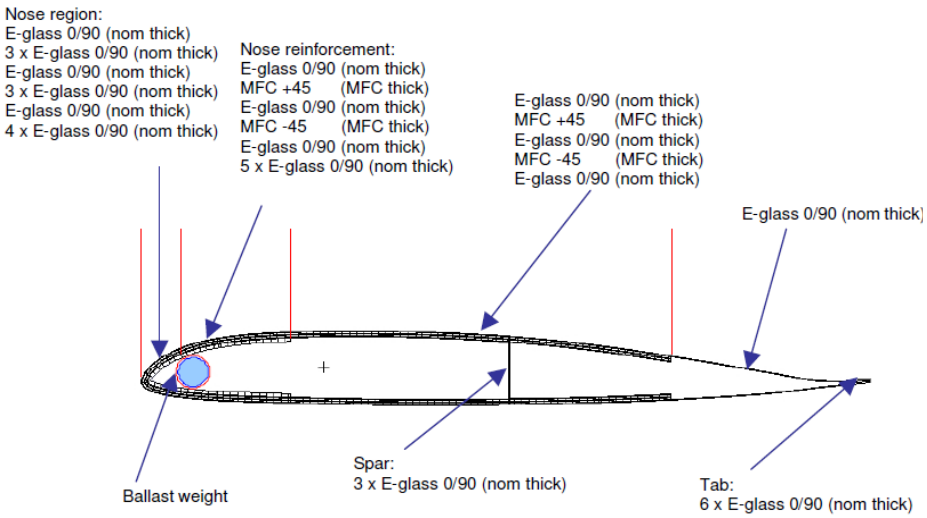

Figure 3.46. Active cross section for **Case Tu**2 showing layup definition

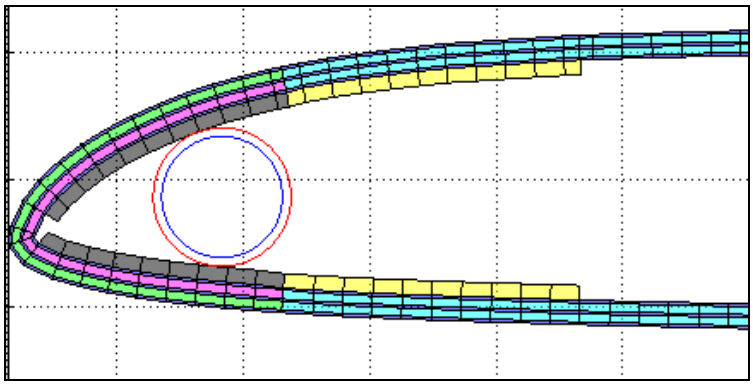

Figure 3.47. Detail of the cross section near the ballast mass location

(Green: outer nose part, Pink: inner nose part, Grey: nose reinforcement before active region, Yellow: nose reinforcement after active region, Blue circle: tungsten rod, Red circle: E-glass cover)

Table 3.48. Active layer geometric information

		Upper	Lower
MFC	placement	0.092c, 0.609c	0.092c, 0.610c
	Width	58mm	58mm
Electrode length	placement	0.609c, 0.709c	0.610c, 0.710c
	Width	11.2mm	11.3mm

Table 3.49. Main blade cross sectional properties

Material Properties	Baseline		**Commercially available**	
Foam implementation	Without foam	**With foam**	Without foam	**With foam**
Thickness of nose part (outer, inner) (mm)	0.114x (3, 3)	0.114x (3, 3)	0.114x (3, 3)	0.114x (3, 3)
Thickness of nose reinforcement (before, after active start) (mm)	0.114x (4, 5)	0.114x (4, 5)	0.114x (4, 5)	0.114x (4, 5)
Margin around ballast weight (mm)	0.114x 3	0.114x 3	0.114x 3	0.114x 3
Active start (upper, bottom)	(0.092c,0.092c)	(0.092c,0.092c)	(0.092c, 0.092c)	(0.092c, 0.092c)
Active end (upper, bottom)	(0.709c,0.710c)	(0.709c,0.710c)	(0.709c, 0.710c)	(0.709c, 0.710c)
End of nose reinforcement	0.1920c	0.1920c	0.1920c	0.1920c
Ballast weight mass	(0.280, 0.0)	(**0.2863**, 0.0)	(0.280, 0.0)	(**0.2863**, 0.0)
Ballast Weight location	(0.068c, 0.4992c)	(0.068c, 0.4992c)	(0.068c, 0.4992c)	(0.068c, 0.4992c)
Spar location	0.50	0.50	0.50	0.50
Tip twist angle (deg)	3.17	3.16	3.17	3.16
1^{st} torsional frequency (1/rev)	4.47	5.39	4.38	5.39
Blade mass / length (kg/m)	0.840	0.890	0.846	0.890
Max strain (με)	5700	5506	5364	5185
Longitudinal strain (με)	2214	2199	2109	2114
Lateral strain (με)	2062	1998	1991	1927
Shear strain (με)	5700	5506	5364	5185
Center of Gravity (CG)	0.2579c	0.2620c	0.2579c	0.2620c
Elastic Axis (EA)	0.2005c	0.2859c	0.2005c	0.2869c

(2) **Root layup**

For the ATR-I blade, graphite/epoxy composite was the material of the choice for the root part of the blade. The same type of graphite/epoxy is also used here. Figure 3.48 shows the cross sectional geometry and layup of the root region. The root layup is made of 28 layers of IM7/SP381 with the following stacking sequence: $(45/0/-45/90)_7$. Additional E-glass plies with various layup angles are added to the spar web to reduce the maximum strain in that region. Option 1 is the case where the spar web is composed of four layers of E-glass, while in Option 2 it has ten layers. Option 3 also has the spar web with four layers but with different layup angles than Option 1, as given in Table 3.51. The stress components for of these cases are also presented on Table 3.51. Option 1 is selected as a candidate for the root design since it satisfies all the strain constraint with a simpler layup.

Table 3.50 shows the desired properties of the blade root provided by NASA Langley, along with the properties from one of the study cases, Option 1. The mass and stiffness matrices for Option 1 (SI units) are given in Appendix 6. The mass per unit length is very similar to the target (desired) value. The stiffness components need to be uncoupled. For example, the lead-lag stiffness seems too high if only considering the diagonal entries of the stiffness matrix. However, it comes with significant extension-bending coupling. To uncouple those terms, the stiffness matrix has been recalculated by UM/VABS with respect to the shear center location.

Table 3.50. ATR-A blade root properties

	Desired Value		Option 1 (w/o foam)	
Unit	English	SI	SI	%
EI (flap)	1831.1 (lb-ft^2)	77.16 (kg-m^2)	305	295
EI (chord)	3800 (lb-ft^2)	118 (kg-m^2)	6760	5630
GJ	1250.0 (lb-ft)	52.68 (kg-m)	215	308
EA	2.2×10^6 (lb)	9.979×10^5 (kg)	2.49×10^7	2395
m	0.0173 (sl/ft)	0.8283 (kg/m)	0.8570	3.46
I_θ	0.000106 (sl-ft)	4.72×10^{-4} (kg-m)	3.02×10^{-4}	-35

Table 3.51. Root cross sectional geometry and max strain component

Material Properties	Baseline			**Commercially available**
	Option 1	Option 2	Option 3	Option 1
Foam implementation	w/o foam			
Thickness of the spar web	0.114*x* 4	0.114*x* 10	0.114*x* 4	0.114*x* 4
Layup of the spar web (E-glass)	0_4	0_{10}	0/45/-45/90	0_4
Max strain	6834.0 (10000)	2832.1 (6800)	4698.7 (10000)	6763.2 (10000)
Γ_{11}	807.4 (10000)	806.0 (3000)	-2188.5 (10000)	714.1(10000)
Γ_{22}	803.5 (10000)	823.3 (5000)	2257.5 (10000)	719.4 (10000)
Γ_{12}	6834.0 (10000)	2832.1 (6800)	4698.7 (10000)	6763.2 (10000)
Γ_{13}	88.5 (10000)	306.5 (10000)	86.8 (10000)	77.8 (10000)
Γ_{23}	87.5 (10000)	76.7 (10000)	86.9 (10000)	76.9 (10000)
Γ_{33}	-797.4 (10000)	-811.2 (10000)	-814.6 (10000)	-769.4 (10000)
Center of Gravity (CG)	0.2380c	0.2037c	0. 2124c	0.2380c
Elastic Axis (EA)	0.1791c	0.2493c	0.1894c	0.1791c

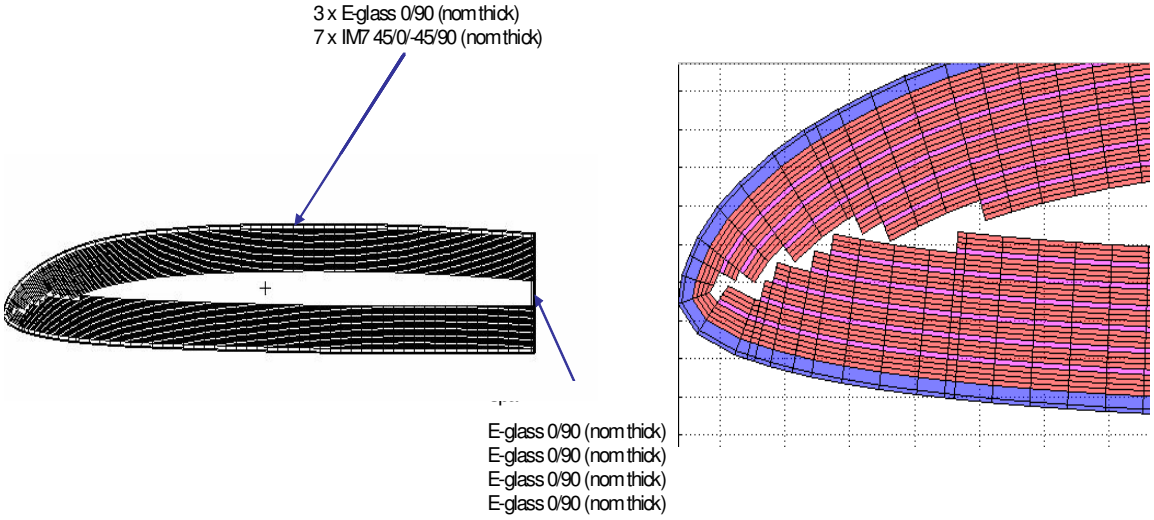

(a) (b)

Figure 3.48. Cross-Section of the root layup – Option 1

(a) Overall sketch (b) Close-up near the leading edge

(3) **Tip layup**

Table 3.52 shows the target properties of the tip and the proposed properties. Table 3.53 shows the results of different layup options for the tip section. Even though we have only few composite plies, every strain component is within the allowable. Figure 3.49 presents an example of tip layup, for Option 3, and the stiffness and mass matrices for this case are presented in Appendix 7.

Table 3.52. ATR-A Blade Tip Properties

	Desired Value				Option 3 (w/o foam)	
r/R	0.965		1.0		Tip region	
Unit	English	SI	English	SI	SI	Δ%
EI (flap)	112.4 (lb-ft^2)	4.71 (kg-m^2)	53.7 (lb-ft^2)	2.26 (kg-m^2)	30.5	1249
EI (chord)	5151 (lb-ft^2)	217 (kg-m^2)	980 (lb-ft^2)	41.3 (kg-m^2)	2010	4766
GJ	117.6 (lb-ft)	4.96 (kg-m)	53.8 (lb-ft)	2.26 (kg-m)	20.7	815
EA	N/A (lb)	N/A (kg)	N/A (lb)	N/A (kg)	1.40×10^{7}	N/A
m	0.0187 (sl/ft)	0.8954 (kg/m)	0.078 (sl/ft)	0.3735 (kg/m)	0.4782	129
I_θ	0.000146 (sl-ft)	6.49×10^{-4} (kg-m)	0.000146 (sl-ft)	6.49×10^{-4} (kg-m)	3.12×10^{-4}	-53

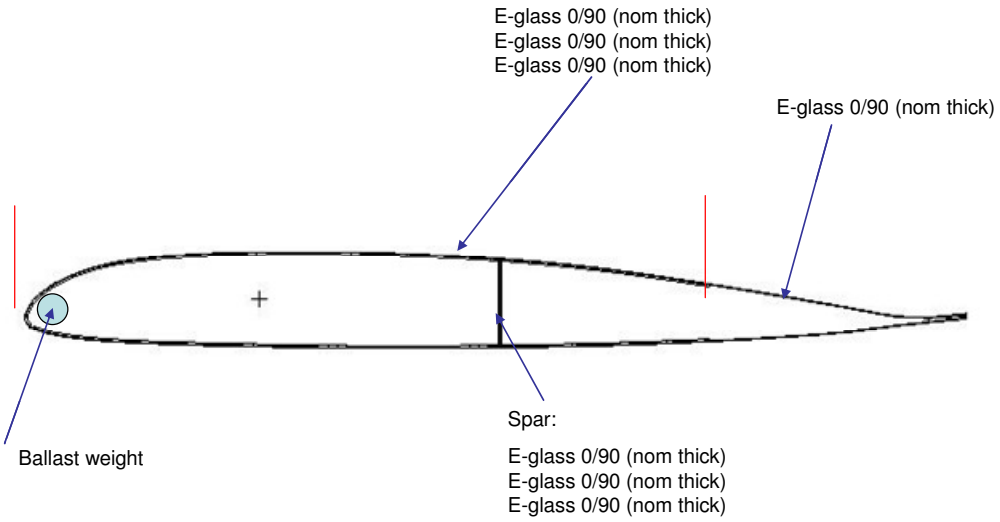

Figure 3.49. Cross-Section sketch for the tip layup definition - Option 3

Table 3.53. Tip cross sectional geometry and maximum strain components

Material Properties	Baseline			**Commercially Available**
	Option 1	Option 2	Option 3	Option 3
Foam implementation	w/o foam			
Inner layer (mm)	0.114× 4	0.114× 3	0.114× 2	0.114× 2
Inner layer end (upper, bottom)	(0.709c, 0.710c)	(0.709c, 0.710c)	(0.709c, 0.710c)	(0.709c, 0.710c)
Ballast weight mass	(0.286, 0.0)	(0.286, 0.000)	(0.286, 0.000)	(0.286, 0.000)
Ballast Weight location	(0.068c, 0.499c)	(0.068c, 0.499c)	(0.068c, 0.499c)	(0.068c, 0.499c)
Spar location (c)	0.504	0.504	0.504	0.504
1st torsional frequency (1/rev)	4.63	4.45	4.45	4.44
Blade mass / length (kg/m)	0.478	0.445	0.411	0.405
Max strain (με)	2560	2867.9	3284.6	3284.6
Longitudinal strain (με)	1380 (15000)	1680 (15000)	2170 (15000)	2020 (15000)
Lateral strain (με)	-204 (10000)	-248 (10000)	-320 (10000)	-303 (10000)
Shear strain (με)	2560 (10000)	2867.9 (10000)	3284.6 (10000)	3280 (10000)
Center of Gravity (CG)	0.205c	0.193c	0.179c	0.181c
Elastic Axis (EA)	0.297c	0.313c	0.331c	0.331c

3.2.10 Final proposed ATR-A Design

This section presents the final design proposed for the ATR-A blade. Figure 3.50 shows the rotor blade split into several sections. Each blade section has different cross sectional design specifications. Blade sections 0, 1, and 2 belong to the main (un-swept) portion of the blade, while blade sections 3 and 4 belong to the swept blade tip. Table 3.55 presents the properties of each blade section. The stock-size tungsten rods used in final design are given in Table 3.54.

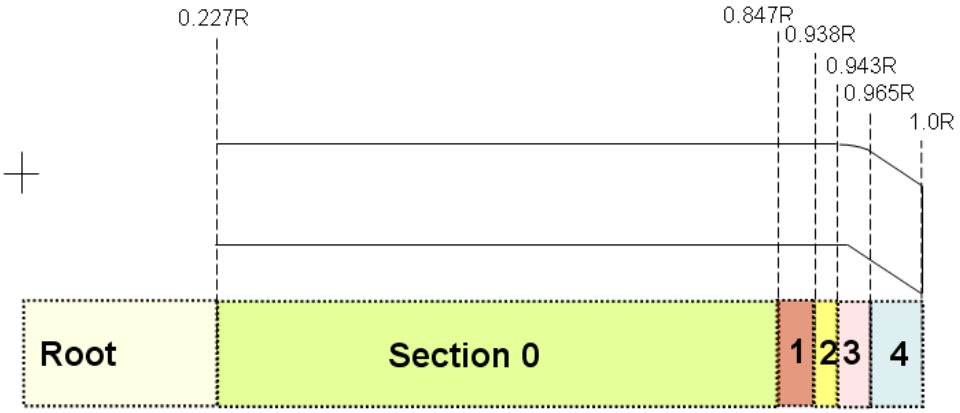

Figure 3.50. Sectional distribution

Figure 3.52 and Figure 3.53 show the layup for the main section of the blade. Figure 3.54 and Figure 3.55 show the layup for the swept part of the blade. It may be noted that, in the swept portion, the layup is the same as in the main part of the blade except for three layers of E-glass (with the same layup angle as the corresponding MFC layer) are used in place of each MFC layer of the main blade section. Also, in the nose region of the swept tip portion, the layup is modified from 0/90 (which is used for the main sections) to +/-45 E-glass. This was done to provide continuity in the ply angle through the end of the blade. The +/-45 plies are used at Sections 3 and 4, to better locate the elastic axis where there is no active material that can be negatively impacted by the layup change. Foam added throughout the span contributed around 0.045 kg/m to the original mass per length property at all sections. However, the center of gravity location in all sections was not significantly affected. Concentrated masses (ballast rods) are applied at the positions indicated Table 3.55. The maximum active MFC width was set to 57mm for the final design. Figure 3.56 shows the details of the VR-18 trailing edge tab.

Table 3.54. Types of tungsten rods

	Diameter (mm)	Area (m^2)	Maximum mass per unit length (kg/m)
A	2.20	3.81×10^{-6}	0.073
B	4.80	1.78×10^{-5}	0.343
C	6.35	3.81×10^{-5}	0.610

Density of Tungsten: 19250kg/m^3

Table 3.55. ATR-A blade properties

Section		Target			Proposed design						
		Mass	I_θ	CG loc	Mass	I_θ	CG loc	EA loc	Ballast rods		
		[kg/m]	[kg-m]	[%c]	[kg/m]	[kg-m]	[%c]	[%c]	Weight [kg/m]	Location [%c]	Type
0	0.227~0.847R	0.89	6.49×10^{-4}	26.2	0.88	5.78×10^{-4}	25.6	28.5	0.2836	6.80	B
1	0.847~0.938R	1.52	9.79×10^{-4}	18.9	1.50	7.69×10^{-4}	19.4	28.5	0.070 0.344 0.500	3.30 6.80 12.1	A B C
2	0.938~0.943R	1.66	6.49×10^{-4}	25.0	1.63	8.84×10^{-4}	25.1	28.5	0.280 0.500 0.260	6.80 12.1 48.0	B C B
3	0.943~0.965R	1.66	6.49×10^{-4}	25.0	1.65	9.57×10^{-4}	25.6	31.7	0.300 0.560 0.385	6.80 12.1 47.4	B C C
4	0.965~1.0R	0.64	6.49×10^{-4}	25.0	0.62	5.20×10^{-4}	26.5	31.7	0.220	6.80	B

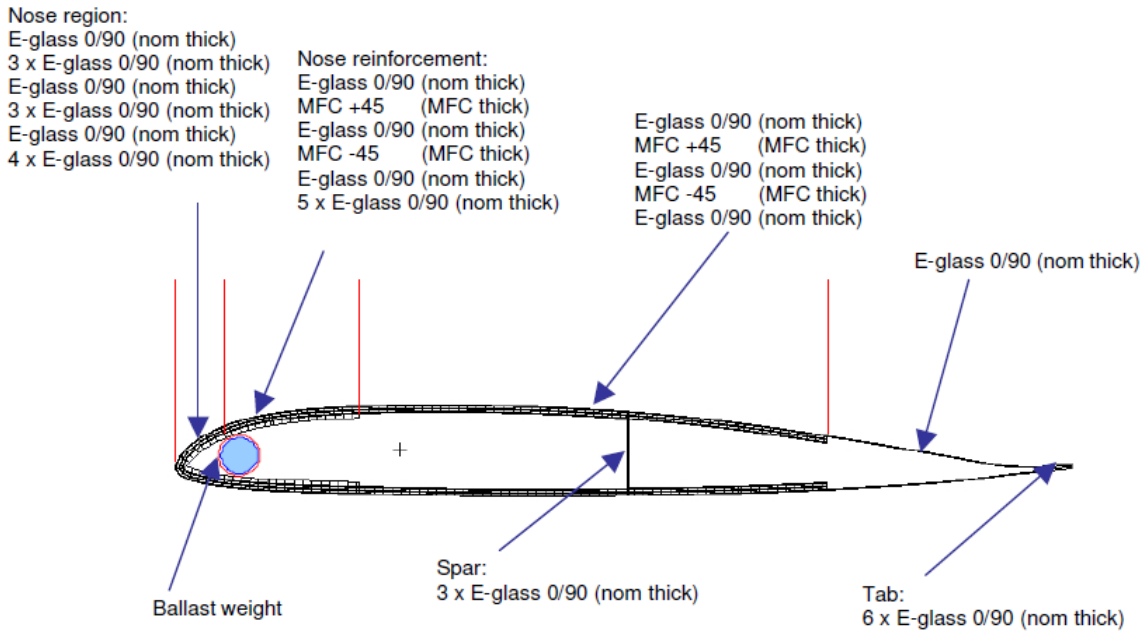

Figure 3.51. Cross section sketch for layup definition (Section 0)

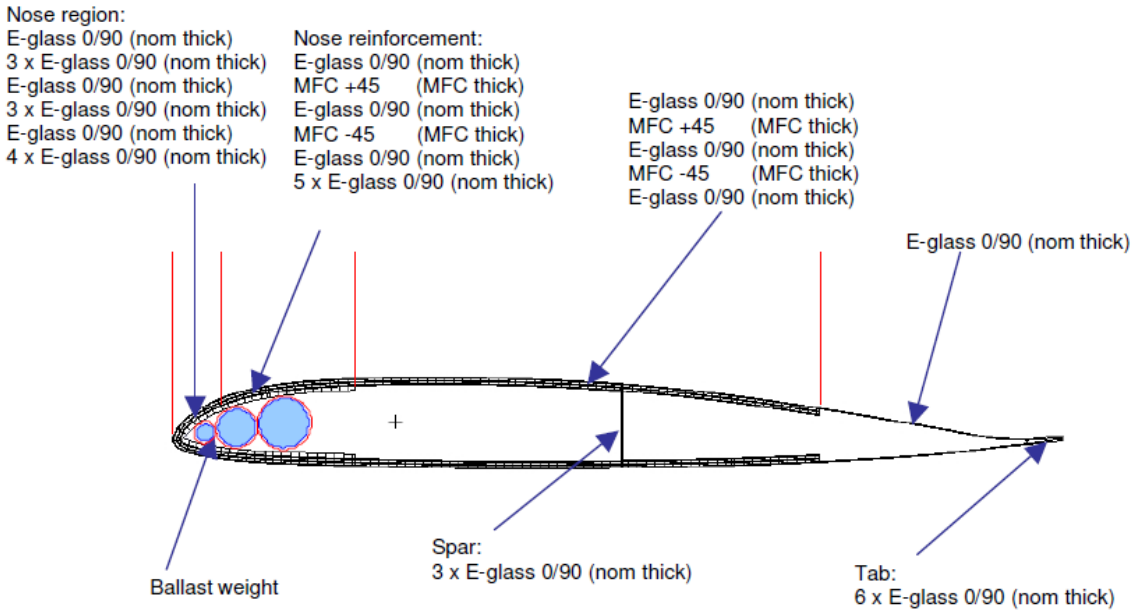

Figure 3.52. Cross section sketch for layup definition (Section 1)

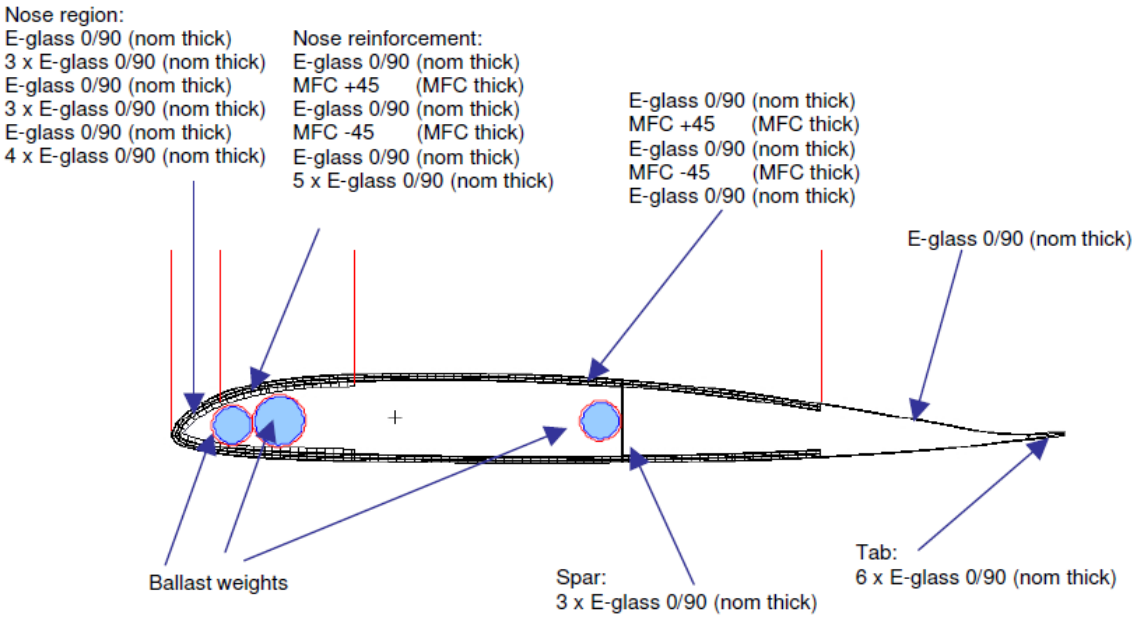

Figure 3.53. Cross section sketch for layup definition (Section 2)

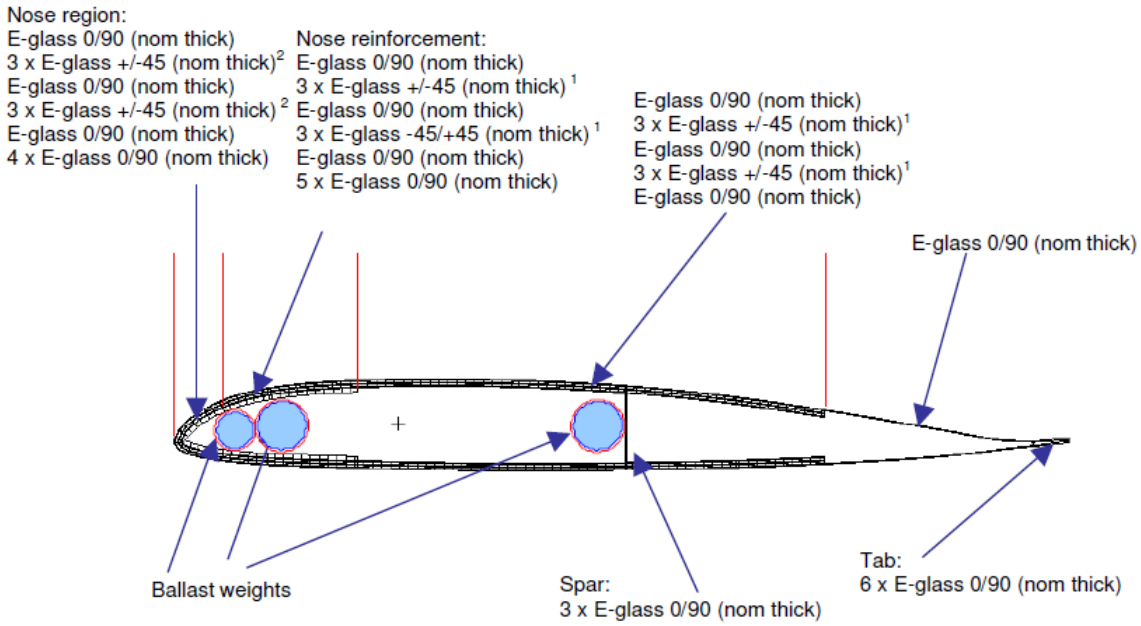

Figure 3.54. Cross section sketch for layup definition (Section 3)

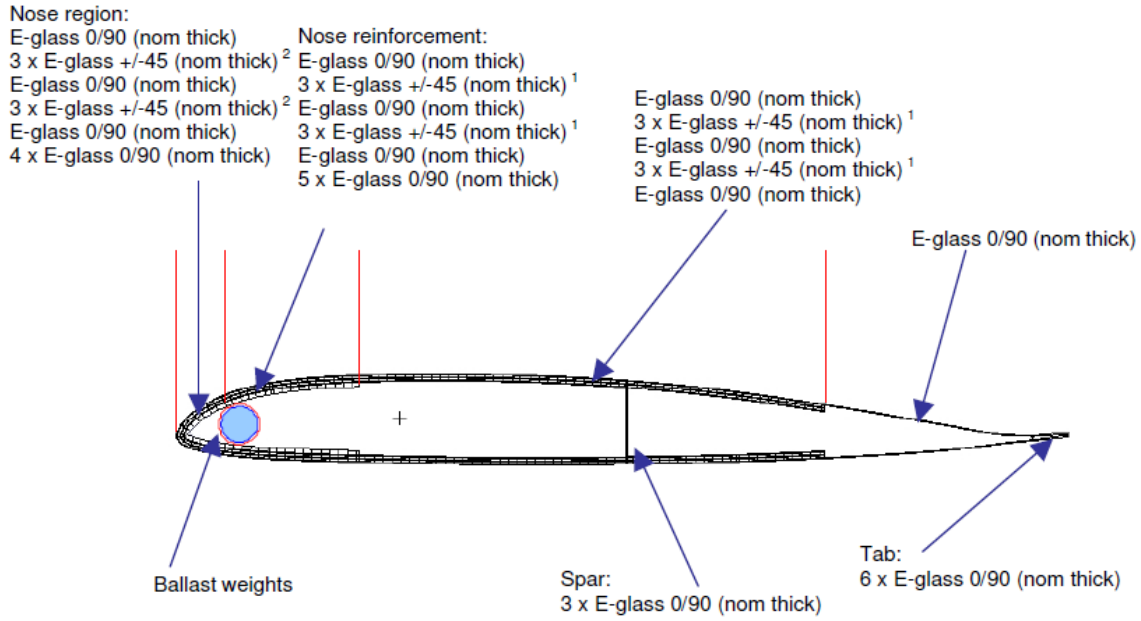

Figure 3.55. Cross section sketch for layup definition (Section 4) [4]

[4] E-glass layer which replaces MFC layer (E-glass +/-45: E-glass 0/90 in 45 degree layup angle)

[2] Corresponding nose layer to super script 1 layer

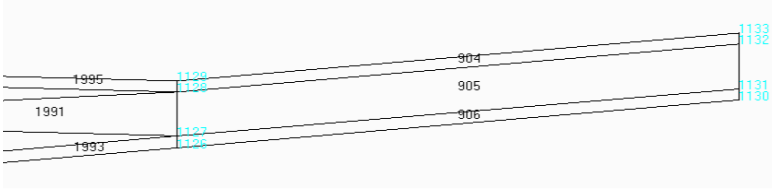

Figure 3.56. Detailed of trailing edge tab

Minor changes have been applied to the proposed design to make it more manufacturable. The length of the electrode is set to a fixed value of 24.5 mm as opposed to keeping it arbitrary. The end point of the electrode is moved to 0.78 chord for both the upper and lower surfaces as shown in Figure 3.57.

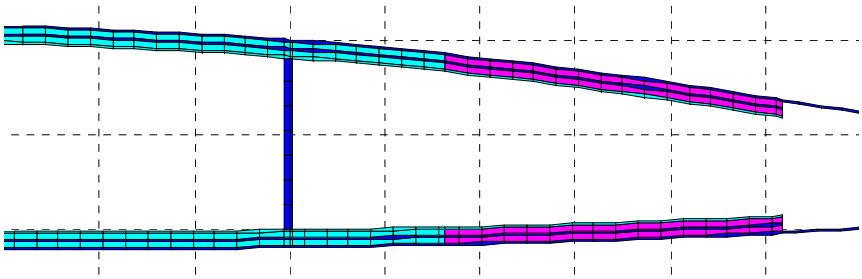

Figure 3.57. Detailed view near the electrode (pink)

When manufacturing, there will be ply-drops as shown in Figure 3.58. Figure 3.59 shows how the ply drops were modeled in this modified design. As a result of these modifications, the basic characteristics of the active blade design have changed, although not significantly. The twist rate is reduced by about 1%; the center of gravity locations of cross sections with electrodes are closer to the trailing edge, as expected. The elastic axis location is closer to the leading edge. This change results in a better design, considering the effect of foam implementation on the elastic axis.

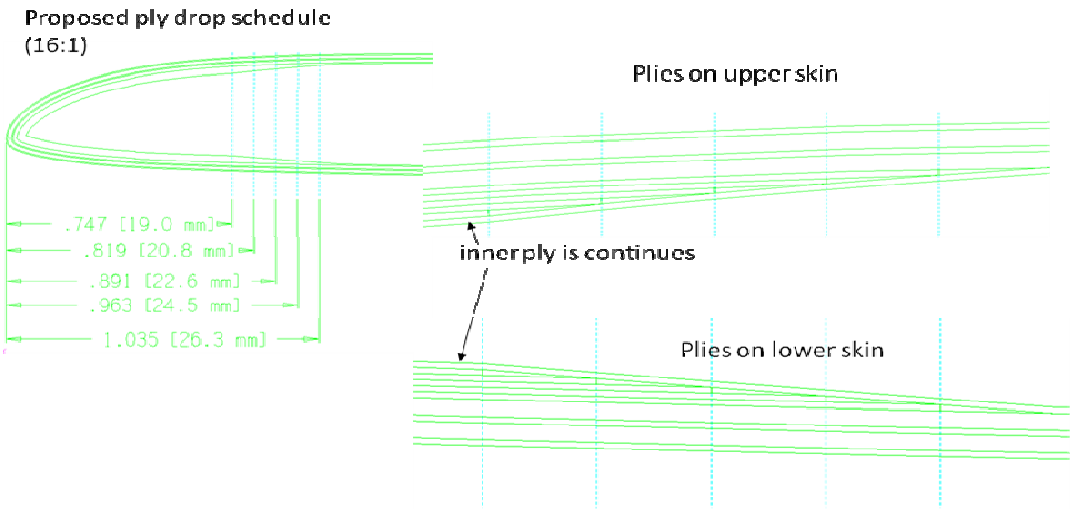

Figure 3.58. Nose zoom for proposed ply drop

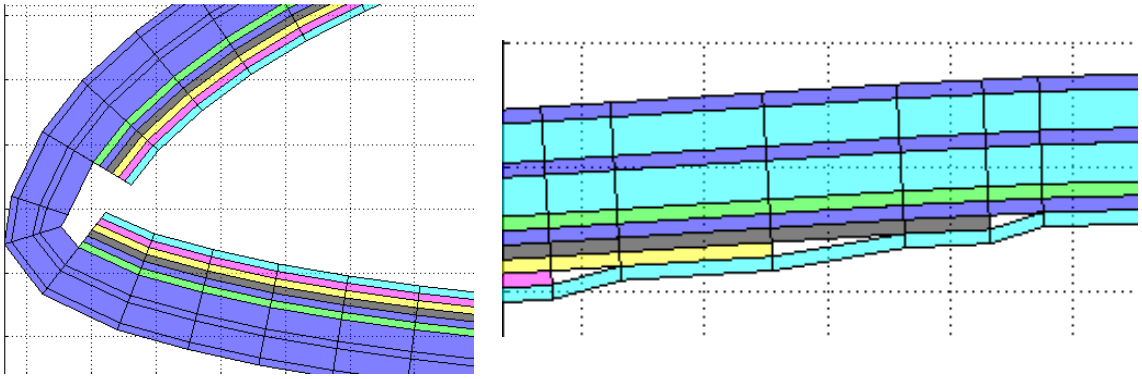

(a) close up near nose (b) Close up near inner ply drop

Figure 3.59. Modeling ply-drop on mesh-generator

3.2.11 Comparison to target design

The following figures show the comparison of stiffness (Figure 3.60) and mass components (Figure 3.61) between targeted values (Table 3.55) and the values from the current design. Mostly, they indicate that the current design is following the targeted value well except for the stiffness at the tip region. The reason is that the tip sections were not optimized separately. Instead, the tip section has been designed to have the same layup as the main section except the MFC plies that were replaced with Glass/Epoxy plies. Glass/Epoxy has higher moduli than MFC, which results in higher stiffness constants. The fact that the stiffness of the blade tip is higer than the target does not impact the blade dynamics significantly since its mass properties are matched well. The overall mass properties could be

adjusted very closely to the given target values by using different ballast mass for each section.

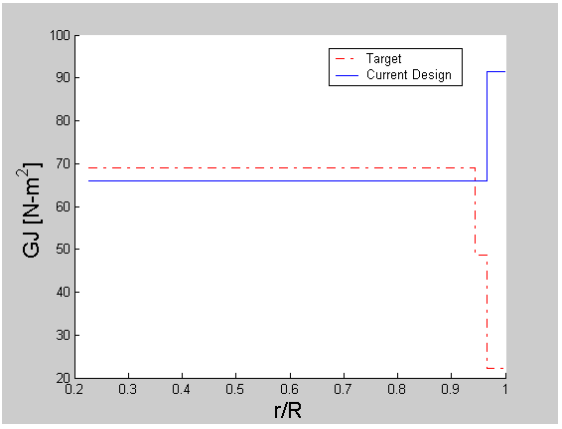

(a) Sectional distribution of torsional stiffness

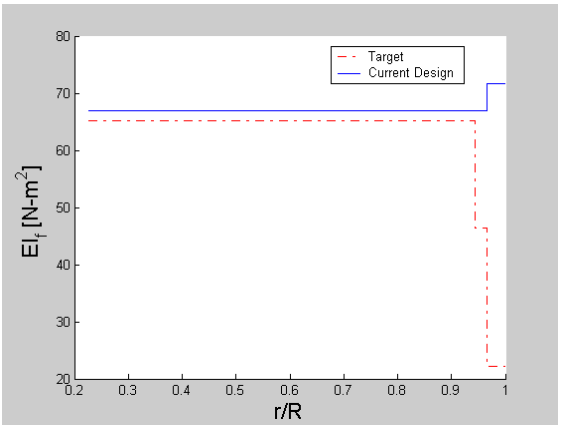

(b) Sectional distribution of flapping stiffness

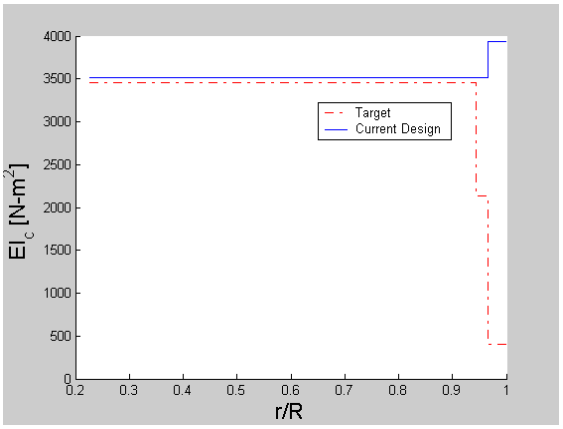

(c) Sectional distribution of chord-wise bending stiffness

Figure 3.60. Comparison of stiffness components

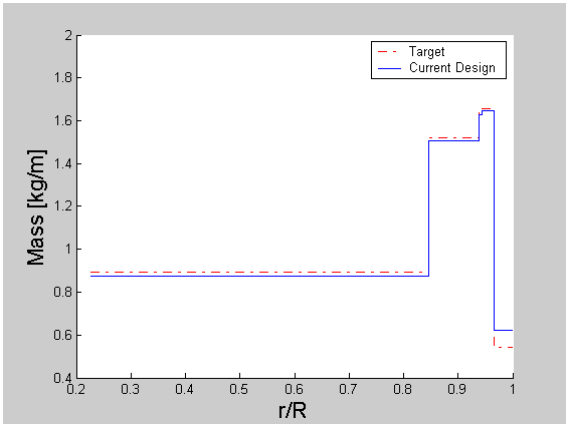

(a) Sectional distribution of mass per unit length

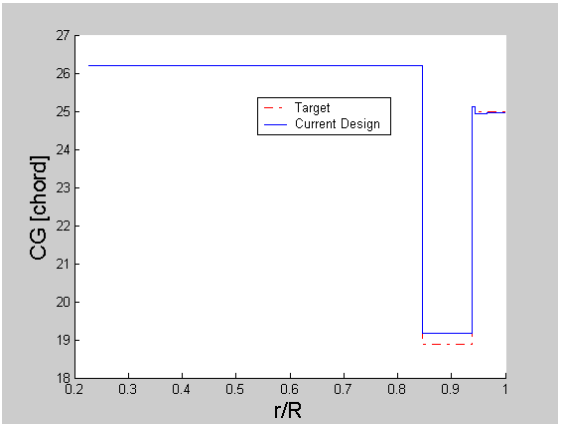

(b) Sectional distribution of center of gravity

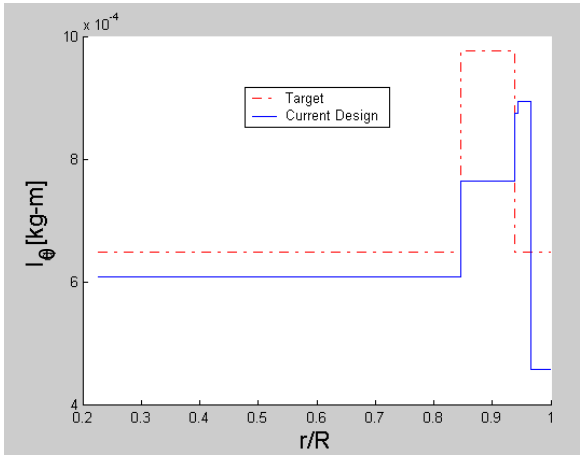

(c) Sectional distribution of torsional inertia

Figure 3.61. Comparison of mass components

3.2.12 Summary of ATR-A design development

As mentioned, the ATR-A example showed the capability to deal with a more complex and realistic model such as different types of airfoil with different blade planform. The DYMORE input generating sub-routine is updated to model the blade with linear twist, droop and swept tip sections making it more stable for this kind of blade. The cases for hinge-less rotors were successfully executed. Some analyses were done on articulated rotors, but it was necessary to include a spring at the root for DYMORE in order to compute the frequencies and modes. At this point, the effect of a spring is not yet well understood and needs further exploration in future work.

Table 3.56. ATR-A blade final design properties

Section		Final design					
		Mass	I_θ	CG loc	EA loc	Ballast rods	
		[kg/m]	[kg-m]	[%c]	[%c]	Weight [kg/m]	Location [%c]
0	0.227~0.847R	0.88	5.78×10^{-4}	25.6	28.5	0.284	6.80
1	0.847~0.938R	1.50	7.69×10^{-4}	19.4	28.5	0.070	3.30
2	0.938~0.943R	1.63	8.84×10^{-4}	25.1	28.5	0.344	6.80
3	0.943~0.965R	1.65	9.57×10^{-4}	25.6	31.7	0.500	12.1
4	0.965~1.000R	0.62	5.20×10^{-4}	26.5	31.7	0.280	6.80

During the pre-processing, the effects of some important parameter have been studied followed by the optimization process. Once the optimization reached convergence, new loads corresponding to that optimized design were recalculated using CAMRAD-II. Based on those loads, another optimization process was run. The results of the application of the new loads on the design are that the MFC plies move toward the leading edge and the tip twist angle increased 6.5 % due to a slight decrease on the design loads. Implementation of denser and stiffer foam on the D-spar region of the cross section helps to reduce the strain generated on the cross section without significantly affecting the actuation obtained. The foam

implementation moved the elastic axis backward and added 0.045kg/m to the weight/length. Specific diameters of the tungsten rod are used for the ballast weight. Ply drop modeling reduced the twist rate by 1%. The final design for each section is shown in section 3.2.10 and the summarized again in Table 3.56.

CHAPTER 4
CONCLUSIONS AND RECOMMENDATIONS

This chapter summarizes the main accomplishments of this dissertation. It then makes conclusions based upon the results from the numerical analysis. Finally, it addresses the recommendations on some of the important areas for future improvements.

4.1 Summary and main conclusions

In this dissertation, the process to optimally design active twist rotor blades was introduced. The proposed optimization framework allows for exploring a rich and highly nonlinear design space in order to maximize twist authority while satisfying a series of constraints. Different analyses are combined in the framework: cross sectional analysis, an automated mesh generator, a one-dimensional beam solver, a three-dimensional local strain module, and numerical optimization routines. The mathematical optimization problem was subdivided in two loops: the other loop provides critical design loads for the inner loop and only need to run for a few iterations. With those critical loads, the inner optimization loop was run for several iterations until an optimum solution was obtained. The design was then passed back to the outer loop, and the process started again until convergence. This convergence shown to be fast, which indicates that although the loads changes with changes in blade stiffness and inertia properties, the critical load values, for structural sizing do not vary much. This allows the design to be done much faster and effectively. Adjustment to the optimum design was done at the end to ensure manufacturability of the blade and to take into account limitations of commercially available materials.

Due to the limitations on some of these solvers, resolution strategies were proposed. These include mesh overlapping, element distortion, trailing edge tab modeling, electrode modeling and foam implementation of the mesh generator. Also, due to sensitivity of the optimizer to the initial designs, an approach to generate an initial feasible design was presented.

The effectiveness of the proposed design process has been demonstrated through two examples. Optimization studies were performed using the existing NASA/Army/MIT ATR blade case. The first example studied was the ATR-I: by introducing the optimization process, the original design was able to be further refined and improved. The optimization process showed that the original design could be improved significantly. The examples showed that the original ATR blade, successfully manufactured and tested, could exhibit at least a 20% higher actuation performance level than the original blade if designed within the proposed optimization framework. The constraint of the elastic axis position with respect to the quarter chord affects the position of the spar along the cross section. Some passive plies are added near the nose to reduce the maximum strain and this showed a positive effect on the actuation authority of the blade.

The second example, ATR-A, presented a much more challenging problem. Based on a scaled model of AH-60D Apache blade, advanced airfoils, blade planform, MFC integrated actuator design, and practical blade mechanical target property distribution along its radius (so to match those of the target rotor system) were introduced to this nonlinear design space. The proposed nested-loop optimization approach was successfully used. Manufacturing and other practical constraints were brought to the problem. Several studies were conducted that investigated the dependence of several blade parameters (e.g., center of gravity, elastic axis, strain hot spots, torsional frequency, etc.) and blade twist authority to the design variables. It was shown, for example, that the unmodeled foam can change the elastic axis by as much as 30% chord and the 1st torsional frequency around 20% while basically not affecting the center of gravity. The effect of placing stiffer foam on the D-spar region of the cross section is also studied. The distorted element showed a very small effect on the blade properties and considered to be negligible. The recalculated worst loading case on the inner loop converged design showed slight decrease and the implementation of those loading to the proposed

optimization process showed that the MFC plies moved toward the leading edge about 20% and increased the active tip twist angle of 6.5%. Based on this optimized design, final designs along the span which satisfied the target values and also the given constraints are proposed. These designs are also been carefully adjusted considering the practical manufacture process.

4.2 Key contributions

The following were the key contributions achieved in this dissertation:

- Development of the first mathematical optimization based design framework for active twist rotor blades

- Introduction of a nested, two-level optimization architecture that speeds up the optimization process.

- Numerically shown that the already test-flown NASA/Army/MIT ATR blade can be altered to have a 30% increase in active tip twist while better satisfying its original target properties

- Complete design of an advanced active twist rotor blade using the new framework. It is based on 1/6 scale of the AH 64D Apache blade that has 2.5 times more authority than its predecessor. The design is being built and is scheduled to fly at NASA's Transonic Dynamics Tunnel during the fall of 2010.

Several other findings associated with the design sensitivities of active twist blades and the practical implementations of the concept were introduced in this dissertation.

4.3 Recommendation for future work

From the studies conducted in this dissertation, the following areas should be considered for further studies:

- Change of the optimization method. The gradient-based optimization method used in this dissertation suffers from the typical shortcomes of this class of optimizer: no guarantee of global optimum and dependence to the initial guess. Introducing different optimization methods that are more robust to the initial point or a global optimization scheme would also be a good option when pursued with careful consideration to the computational cost.

- Improve on the sensitivity calculation. The sensitivity of the objective function and constraints were calculated based on direct finite differences. This was done for simplicity at an increased computational cost. While analytical sensitivity is not feasible due to the complexity of the problem, there are alternative methods that are far superior to the simple finite difference (e.g., Adjoint Method).

- Further subdivision of the optimization architecture. While dealing with the ply thickness as continuous design variables worked well, the manual rounding of their results to integer multiples of the prepreg nominal thickness slows down the optimization process. This could be avoided by using the stiffness and mass constants as design variables and setup a separate inverse optimization in which ply thickness and angles need to be determined to match the target stiffness and mass constants coming from the other optimization loop.

- Further study on the relative frequency of loads calculation. Although the inner-outer loop separation proved to work very well for the cases studied in this dissertation, more studies are recommended. By extending the implemented formulation such that

both the inner and outer loops are part of the same Matlab code, one could better quantify the frequency needed for the critical loads to be recalculated. Moreover, this is expected to be a function of the initial design and flight conditions.

- Introduction of a dynamic objective function. Instead of maximizing static tip twist, a more interesting objective function would be to maximize the tip twist at (N-1)P, NP, and (N+1)P, where N represents the number of blades and P the blade passage frequency. This reflects the ultimate goal that is to maximize blade control authority for vibration reduction at the frequency range of interest.

Appendix 1. ATR optimization code structure

The structure of the code used in this dissertation is presented below. Blocks indicate the sub folders and the files under that folder. The first column shows the sequence of the file called, with the heritage being associated with the origin of the call. The file name itself is quite self –explanatory but the last column gives some additional information.

Process Seq.	Code Structure	Heritage	Etc
	ATR_Optimization		
1	ATR_design.m		
0	del_previous_design.m		
	INPUTS		
2	input_optmization_options	ATR_design.m	
3	input_initials.m	ATR_design.m	
4	problem_definition_inputs	ATR_design.m	
5	input_constraint.m	ATR_design.m	
6	input_airfoil_data.m	ATR_design.m	
31	input_worst_loading.m	compute_strain.m	
10	Sec_1_layup.m	run_Xsectional_analysis.m	Section 1 layup info
10	Sec_2_layup.m	run_Xsectional_analysis.m	Section 2 layup info
10	Sec_3_layup.m	run_Xsectional_analysis.m	Section 3 layup info
10	Sec_4_layup.m	run_Xsectional_analysis.m	Section 4 layup info
	ROUTINES		
7	objective_function.m	ATR_design.m	
8	compute_obj_fun_value.m	objective_function.m	
33	compute_obj_fun_gradient.m	objective_function.m	
7	constraint.m	ATR_design.m	
32	compute_constraint_value.m	compute_obj_fun_value.m	
34	compute_constraint_gradient.m	compute_obj_fun_gradient.m	
9	run_Xsectional_analysis.m	compute_obj_fun_value.m	Run Xsectional analsys module
22	run_Beam_analysis.m	compute_obj_fun_value.m	Run Beam analysis module
29	run_Strain_analysis.m	compute_obj_fun_value.m	Run strain recovery module
30	compute_strain.m	run_Strain_analysis.m	
	Xsectional_analysis		
11	Xsection_main.m	run_Xsectional_analysis.m	
20	vabs.exe	Xsection_main.m	UM/VABS executable
	Xroutines		
12	getMATS0.m	Xsection_main.m	
13	convertMATS.m	Xsection_main.m	Read material properties
14	get_airfoil_coordinate.m	Xsection_main.m	convert material properties
15	ARcorrect.m	Xsection_main.m	mesh-generator
16	offset.m	Xsection_main.m	mesh-generator
17	trim.m	Xsection_main.m	mesh-generator
18	numbering1.m	Xsection_main.m	mesh-generator
19	VABSwrite.m	Xsection_main.m	write UM/VABS input file
21	VABSread.m	Xsection_main.m	Read UM/VABS output file
	Beam_analysis		
23	write_DYM.m	run_Beam_analysis.m	write ATR_strucprop.dat
24	write_DYM_input.m	run_Beam_analysis.m	write input.dym
25	write_DYM_blade.m	run_Beam_analysis.m	write ATR_blade.dat
26	Dymore.exe	run_Beam_analysis.m	DYMORE executable
27	read_DYM.m	run_Beam_analysis.m	read from ATRs_4b.evl
28	read_DYM_MDT.m	run_Beam_analysis.m	read from ATRs_4b.mdt

Appendix 2. Maximum loads for ATR-I by CAMRAD II

Max loads for Torsion case (in - lb)

0.2R	0.3R	0.4R	0.5R	0.6R	0.7R	0.8R	0.9R
-11.7	-10.7	-9.6	-7.8	-6.6	-5.1	-3.3	-1.8
6.2	4.2	3.2	3.9	5.2	3.5	2.7	1
-10.7	-11.15	-10.2	-5.9	-8.05	-4	-2.9	-1.55

Max loads for Flap-wise bending case (in -lb)

0.2R	0.3R	0.4R	0.5R	0.6R	0.7R	0.8R	0.9R
-11.7	-10.7	-9.6	-7.8	-6.6	-5.1	-3.3	-1.8
6.2	4.2	3.2	3.9	5.2	3.5	2.7	1
-10.7	-11.15	-10.2	-5.9	-8.05	-4	-2.9	-1.55

Max loads for Lag-wise bending case (in - lb)

0.2R	0.3R	0.4R	0.5R	0.6R	0.7R	0.8R	0.9R
-11.7	-10.7	-9.6	-7.8	-6.6	-5.1	-3.3	-1.8
6.2	4.2	3.2	3.9	5.2	3.5	2.7	1
-10.7	-11.15	-10.2	-5.9	-8.05	-4	-2.9	-1.55

Appendix 3. ATR-A blade lead-lag stiffness study

The ATR-A initial design presented over three times the lead-lag stiffness (EI_lag) of the ATR-I baseline case. Although the blade geometrics are different, it was unknown the sources of such high lead-lag stiffness in the ATR-A blade. All the cases considered here do not include foam. To study the effect of the different design variables and other blade characteristics, several cases are performed as shown in Table A.. Starting from the ATR-I baseline model, individual design variables are changed and the % change in lead-lag stiffness is shown. Most of the changes from ATR-I to ATR-A have a positive effect, highlighted in **Bold**, especially the active end which was the key factor for such increase in the lead-lag stiffness. There are some changes that have a negative effect, highlighted in *Italic*, such as the change in active material properties, and the web extension.

Table A.2.1 Sensitivity of lead-lag stiffness with respect to different blade characteristics

CASE		EI_{lag}	%	Modified Parameters	Before	After
ATR-I	0	1088	100			
	1	1953	**180**	Active end	0.45c	0.7265c
	2	1099	**101**	Active start	0.0455c	0.1048c
	3	1964	**181**	Active start, end	0.0455c, 0.45c	0.1048c, 0.7265c
	4	1061	*98*	Active material	AFC	MFC
	5	1409	**129**	Chord length	0.1077	0.1173
	6	1224	**112**	Airfoil type	NACA0012	VR18
	7	1277	**117**	Trailing Edge Tab + Airfoil type	NACA w/o tab	VR w/ tab
	8	1124	**103**	Cross sectional layup	ATR-I	ATR-A
	9	1118	**103**	spar location	0.4438	0.5035
	10	1099	**101**	spar web thickness	2	3
	11	1106	**102**	Angle of ply between active plies	45	0
	12	1067	98	Web extension	0.05	0
	13	2330	**214**	Geometric var[5].	ATR-I	ATR-A
ATR-A W/o foam	14	3305	**304**	Geometric var. + Airfoil char[6].	ATR-I	ATR-A

[5] start and end of active material, cross sectional layup, spar location and thickness, web extension, angle of ply

[6] chord length, airfoil type, trailing edge tab

Appendix 4. Maximum loads for Case T1(b) by CAMRAD II

Max loads for Torsion case (in - lb)

0.1R	0.2R	0.23R	0.28R	0.3R	0.33R	0.34R	0.38R	0.4R	0.43R	0.48R	0.5R	0.53R	0.58R	0.6R	0.63R	0.65R	0.68R	0.7R	0.73R	0.78R	0.8R	0.83R	0.88R	0.9R	0.93R	0.95R	0.98R	1.0R
-78.36	-77.82	-94.47	-83.52	-92.83	-81.64	-81.21	-79.39	-78.41	-77.04	-74.30	-73.14	-71.41	-68.26	-66.91	-64.98	-63.08	-60.70	-58.87	-56.15	-51.48	-49.79	-47.45	-43.40	-42.19	-35.50	-12.33	-3.17	0.00
14.37	12.25	29.21	29.84	29.12	28.03	27.66	19.80	19.57	19.39	19.03	18.53	17.80	-31.04	-30.25	-5.02	-4.70	-3.31	-2.41	-1.08	-4.97	-3.89	-2.28	4.50	5.17	-4.31	-3.62	-1.65	0.00
-13.96	-13.09	14.23	10.32	14.68	14.77	14.80	14.92	14.96	15.33	-5.89	-5.59	-5.09	-4.31	-4.01	-3.54	-3.28	-2.85	-2.58	-2.15	-1.38	-1.04	-0.19	1.35	2.02	12.05	-2.68	-2.68	0.00
-39.49	-38.47	-18.99	-18.43	-18.25	-53.59	-53.36	-60.78	-60.13	-58.83	-56.32	-55.22	-53.50	-50.37	-49.04	-46.87	-45.14	-42.72	-40.99	-38.40	-17.05	-15.41	-12.91	-8.60	-7.07	7.97	-8.50	-3.17	0.00
-5.53	-4.99	13.64	12.51	12.12	-17.96	-18.00	-18.03	-18.01	-17.65	-5.72	-5.88	-5.88	-5.88	15.71	15.64	15.60	15.38	8.78	7.56	6.00	3.80	3.44	3.34	3.18	2.59	12.47	-4.74	-0.80	0.00
-29.40	14.86	12.74	10.32	9.43	-11.56	-11.47	-17.96	-1.00	-12.10	-19.57	-18.89	-17.76	20.07	19.37	19.07	18.09	17.46	16.76	15.71	-33.58	-24.88	-2.28	0.99	2.27	-4.31	-1.91	-2.10	0.00

Max loads for Flap wise bending case (in -lb)

0.1R	0.2R	0.23R	0.28R	0.3R	0.33R	0.34R	0.38R	0.4R	0.43R	0.48R	0.5R	0.53R	0.58R	0.6R	0.63R	0.65R	0.68R	0.7R	0.73R	0.78R	0.8R	0.83R	0.88R	0.9R	0.93R	0.95R	0.98R	1.0R
-15.03	-39.80	-2.09	4.98	7.03	9.29	9.73	10.66	10.53	10.79	12.68	13.88	15.64	17.93	18.27	19.70	20.76	22.60	23.69	24.64	24.57	23.31	20.74	23.76	9.83	-0.97	-8.46	-2.33	0.00
-63.60	-99.56	-80.19	-63.83	-60.67	-57.29	-56.54	-53.35	-52.07	-50.20	-49.01	-48.91	-48.61	52.50	56.00	61.11	66.08	74.54	80.02	97.07	93.04	92.81	85.08	54.37	34.59	-17.20	-13.12	-3.22	0.00
1.27	-18.80	-24.68	-55.43	-34.31	-35.97	-36.31	-36.10	-35.36	-33.60	-28.37	-26.25	-22.56	-15.01	-11.79	-6.93	-3.15	3.46	8.27	15.48	25.44	27.95	27.59	16.87	8.06	-10.73	-8.53	-2.11	0.00
7.39	-12.35	-15.62	-19.38	-19.70	0.34	1.41	7.02	9.30	12.80	21.93	26.52	33.61	45.18	49.24	54.14	57.55	62.77	66.00	69.86	86.88	86.48	79.27	50.34	31.66	-4.44	-7.73	-2.33	0.00
1.17	-34.31	-35.68	-39.76	-39.85	-22.98	-21.76	-17.75	-16.05	-12.56	-6.17	-2.04	4.24	-17.01	-13.68	-8.13	-3.84	27.68	34.81	45.58	60.93	65.05	64.33	41.16	24.66	-4.77	-9.20	-1.37	0.00
7.10	-98.30	-76.81	-55.43	-50.25	-5.72	-3.86	-32.43	1.82	9.19	15.52	21.27	30.43	-15.18	-8.20	0.38	7.20	19.50	28.72	42.91	-18.83	-6.53	85.08	53.97	33.93	-17.20	-11.63	-3.11	0.00

Max loads for Lag wise bending case (in - lb)

0.1R	0.2R	0.23R	0.28R	0.3R	0.33R	0.34R	0.38R	0.4R	0.43R	0.48R	0.5R	0.53R	0.58R	0.6R	0.63R	0.65R	0.68R	0.7R	0.73R	0.78R	0.8R	0.83R	0.88R	0.9R	0.93R	0.95R	0.98R	1.0R
343.51	113.03	168.06	-10.95	84.17	99.89	97.11	86.25	81.36	74.58	64.86	61.51	56.98	50.65	48.50	45.65	43.94	41.72	40.42	38.66	42.90	41.08	38.20	29.24	32.77	89.26	105.53	17.81	0.00
123.46	-130.00	-58.69	-141.54	-49.80	-34.28	-36.77	86.49	80.22	71.18	75.81	70.89	64.24	41.39	40.12	25.74	1.19	1.45	2.01	3.44	-15.93	-10.46	-2.04	18.11	20.24	84.32	105.22	16.86	0.00
510.90	306.54	382.24	-222.32	313.56	333.43	331.67	322.64	317.32	308.11	290.87	282.74	269.31	243.63	232.32	214.47	201.95	182.40	169.00	148.69	115.34	102.55	94.25	56.06	45.85	96.21	107.82	17.88	0.00
452.33	241.38	316.14	146.12	244.73	139.71	136.92	3.15	-2.34	-9.35	-18.10	-20.54	-23.09	-24.41	-23.95	-22.00	-20.18	-16.70	-13.94	-9.27	-7.39	-3.27	3.53	14.00	17.42	87.49	105.96	17.81	0.00
363.91	88.41	144.72	-47.73	40.92	-4.84	-1.54	10.17	15.53	22.80	-26.36	-22.39	-16.70	240.00	228.31	209.92	197.08	-60.02	-53.99	-44.18	-25.93	-18.34	-7.44	2.72	9.65	85.81	107.37	17.73	0.00
504.96	-150.75	-73.40	-223.32	-124.34	56.52	55.14	219.13	129.79	22.36	-46.57	-49.64	-50.58	3.91	1.51	-1.14	-2.53	-3.94	-4.37	-4.13	15.57	18.41	-2.04	11.24	15.70	84.32	101.64	17.35	0.00

Max loads for axial shear force case (lb)

0.1R	0.2R	0.23R	0.28R	0.3R	0.33R	0.34R	0.38R	0.4R	0.43R	0.48R	0.5R	0.53R	0.58R	0.6R	0.63R	0.65R	0.68R	0.7R	0.73R	0.78R	0.8R	0.83R	0.88R	0.9R	0.93R	0.95R	0.98R	1.0R
1394.9	1319.9	1304.6	1274.7	1261.6	1240.1	1232.5	1199.8	1182.0	1153.7	1102.0	1079.7	1044.6	981.5	954.6	912.7	883.5	838.2	806.8	757.9	670.4	634.4	578.7	483.4	436.6	200.1	129.6	28.4	0.0
1337.8	1266.8	1251.8	1226.9	1214.2	1193.4	1186.0	1163.8	1146.2	1118.2	1089.0	1066.5	1031.2	982.4	955.7	911.6	886.6	841.4	810.2	761.4	676.2	640.2	584.4	485.7	444.9	196.7	127.0	27.0	0.0
1400.1	1323.1	1306.8	1218.2	1262.4	1240.2	1232.3	1198.5	1180.2	1151.1	1100.2	1077.4	1041.4	977.0	949.7	907.1	877.5	831.6	800.0	750.8	664.6	628.6	573.0	476.1	435.8	198.4	129.9	27.7	0.0
1404.0	1327.8	1311.7	1281.2	1267.8	1245.9	1238.2	1205.3	1187.7	1159.7	1108.3	1086.2	1051.2	988.4	961.6	919.8	890.7	845.3	813.9	765.0	678.8	642.7	586.7	488.6	447.6	203.8	131.5	28.4	0.0
1381.0	1305.5	1289.9	1260.4	1247.3	1191.4	1184.2	1153.4	1136.7	1109.9	1060.4	1039.3	1005.9	974.5	947.1	904.5	874.9	808.4	778.3	731.4	648.6	613.8	559.9	464.1	424.8	201.9	126.9	28.0	0.0
1402.0	1260.9	1246.1	1218.2	1205.9	1234.3	1226.8	1190.8	1178.0	1154.2	1102.5	1080.7	1046.1	951.2	925.2	884.6	856.4	812.4	782.0	734.7	658.0	621.5	584.4	496.6	445.8	196.7	126.6	27.4	0.0

Max loads for chord shear force case (lb)

0.1R	0.2R	0.23R	0.28R	0.3R	0.33R	0.34R	0.38R	0.4R	0.43R	0.48R	0.5R	0.53R	0.58R	0.6R	0.63R	0.65R	0.68R	0.7R	0.73R	0.78R	0.8R	0.83R	0.88R	0.9R	0.93R	0.95R	0.98R	1.0R
23.50	16.65	5.66	4.35	3.90	3.26	3.06	2.29	1.95	1.37	0.52	0.22	-0.25	-0.95	-1.20	-1.44	-1.66	-2.00	-2.20	-2.46	-2.15	-2.15	-2.05	-2.72	-0.77	-2.74	33.20	6.75	0.00
21.51	12.37	1.70	4.11	3.64	2.91	2.67	3.41	3.24	2.77	1.67	1.30	0.72	-1.59	-1.77	-2.06	-2.80	-3.36	-3.67	-4.17	-7.63	-7.87	-8.11	-5.78	-5.81	-3.99	34.34	6.78	0.00
17.05	12.08	1.28	-2.37	1.03	1.25	1.36	1.97	2.37	2.91	3.56	4.06	4.69	5.70	6.08	6.63	6.93	7.11	7.21	7.10	6.41	5.97	5.42	3.88	3.14	0.56	35.11	7.25	0.00
17.78	12.79	1.94	1.53	1.50	3.07	2.95	2.81	2.31	1.39	-0.02	-0.54	-1.42	-2.76	-3.25	-3.98	-4.38	-4.99	-5.33	-5.79	-6.67	-6.90	-7.19	-6.86	-6.55	-4.89	32.68	6.75	0.00
30.25	21.95	10.58	8.53	7.68	-6.55	-6.49	-6.20	-6.03	-5.51	-5.27	-5.24	-5.21	6.09	6.46	6.93	7.21	-7.41	-7.78	-8.42	-9.22	-9.30	-9.13	-9.37	-9.10	-5.36	35.29	7.41	0.00
16.89	8.87	-1.55	-2.37	-2.64	0.95	0.88	2.72	1.08	0.95	-0.30	-0.81	-1.73	-0.52	-0.76	-1.33	-1.61	-2.29	-2.68	-3.42	-5.41	-5.15	-8.11	-7.69	-7.29	-3.99	31.94	7.17	0.00

Max loads for normal shear force case (lb)

0.1R	0.2R	0.23R	0.28R	0.3R	0.33R	0.34R	0.38R	0.4R	0.43R	0.48R	0.5R	0.53R	0.58R	0.6R	0.63R	0.65R	0.68R	0.7R	0.73R	0.78R	0.8R	0.83R	0.88R	0.9R	0.93R	0.95R	0.98R	1.0R
-6.42	2.67	1.59	0.80	0.43	-0.21	-0.40	-1.18	-1.39	-0.97	-0.43	-0.27	-0.27	-0.64	-0.93	-0.51	-0.34	-0.28	-0.39	-0.64	-1.72	-1.95	-2.66	-7.11	-8.58	-1.19	0.47	0.91	0.00
-0.05	10.39	7.60	2.26	1.57	0.84	0.74	0.12	0.72	0.72	-0.68	-0.44	-0.32	1.48	1.44	2.88	4.14	3.71	3.52	2.38	-0.87	-2.41	-6.25	-14.49	-18.11	5.44	3.44	2.71	0.00
-11.57	-4.76	-3.03	3.76	-1.15	-0.44	-0.22	0.51	0.89	0.79	1.28	1.74	1.97	2.28	2.43	2.79	3.27	3.29	3.52	3.16	1.67	0.74	-1.51	-6.76	-9.22	1.64	2.42	1.26	0.00
-7.85	-3.71	-2.02	-0.72	-0.18	0.98	1.06	0.46	0.39	1.05	2.02	2.42	2.30	1.82	1.58	1.71	1.87	1.47	1.23	0.41	-0.91	-2.37	-5.91	-13.75	-17.27	-1.05	-0.24	0.91	0.00
-5.14	-2.71	-1.72	-1.62	-1.59	1.16	0.95	0.45	0.55	1.06	2.08	2.40	2.41	2.30	2.57	3.00	3.54	4.60	4.92	4.50	2.46	1.14	-2.61	-11.56	-16.05	-1.31	2.08	1.08	0.00
-11.76	11.41	8.35	3.76	2.60	2.24	2.24	-2.36	2.72	2.66	3.13	3.72	3.75	4.25	4.69	5.32	6.25	6.48	7.00	6.59	-4.37	-3.60	-6.25	-14.74	-18.51	5.44	5.32	3.06	0.00

Appendix 5. Refined ATR-A main blade mass stiffness and actuation matrices (SI unit)

With the baseline material properties (w/ foam):

$$m = \begin{bmatrix} 0.89 & 0.00 & 0.00 & 0.00 & -2.81x10^{-4} & -1.23x10^{-3} \\ 0.00 & 0.89 & 0.00 & 2.81x10^{-4} & 0.00 & 0.00 \\ 0.00 & 0.00 & 0.89 & 1.23x10^{-3} & 0.00 & 0.00 \\ 0.00 & 2.81x10^{-4} & 1.23x10^{-3} & 6.02x10^{-4} & 0.00 & 0.00 \\ -2.81x10^{-4} & 0.00 & 0.00 & 0.00 & 1.30x10^{-5} & 3.97x10^{-7} \\ -1.23x10^{-3} & 0.00 & 0.00 & 0.00 & 3.97x10^{-7} & 5.89x10^{-4} \end{bmatrix}$$

$$k = \begin{bmatrix} 3.32x10^{6} & -32.92 & -4.61 & -0.084 & -1.38x10^{3} & -3.84x10^{4} \\ -32.92 & 6.27x10^{5} & 1.32x10^{4} & -2.13x10^{2} & 1.79x10^{-1} & 1.62x10^{-1} \\ -4.61 & 1.32x10^{4} & 4.02x10^{4} & 1.64x10^{2} & 0.70 & -7.56x10^{-2} \\ -0.084 & -2.13x10^{2} & 1.64x10^{2} & 65.73 & -0.39 & -4.17x10^{-3} \\ -1.38x10^{3} & 1.79x10^{-1} & 0.70 & -0.39 & 63.97 & -8.11 \\ -3.84x10^{4} & 1.62x10^{-1} & -7.56x10^{-2} & -4.17x10^{-3} & -8.11 & 3.34x10^{3} \end{bmatrix}$$

$$F^{(a)} = \begin{bmatrix} 0.8578 & 4.5885 & 14.7767 & -3.0453 & 0.0409 & 0.0002 \end{bmatrix}^{T}$$

With the commercially available material properties (w/ foam):

$$m = \begin{bmatrix} 0.89 & 0.00 & 0.00 & 0.00 & -2.81x10^{-4} & -1.26x10^{-3} \\ 0.00 & 0.89 & 0.00 & 2.81x10^{-4} & 0.00 & 0.00 \\ 0.00 & 0.00 & 0.89 & 1.26x10^{-3} & 0.00 & 0.00 \\ 0.00 & 2.81x10^{-4} & 1.26x10^{-3} & 6.02x10^{-4} & 0.00 & 0.00 \\ -2.81x10^{-4} & 0.00 & 0.00 & 0.00 & 1.30x10^{-5} & 3.97x10^{-7} \\ -1.26x10^{-3} & 0.00 & 0.00 & 0.00 & 3.97x10^{-7} & 5.89x10^{-4} \end{bmatrix}$$

$$k = \begin{bmatrix} 3.48x10^{6} & -34.66 & -4.85 & -0.086 & -1.47x10^{3} & -3.95x10^{4} \\ -34.66 & 6.32x10^{5} & 1.39x10^{4} & -2.10x10^{2} & 1.95x10^{-1} & 1.69x10^{-1} \\ -4.85 & 1.39x10^{4} & 4.20x10^{4} & 1.76x10^{2} & 0.75 & -8.14x10^{-2} \\ -0.084 & -2.10x10^{2} & 1.76x10^{2} & 65.95 & -0.39 & -4.23x10^{-3} \\ -1.47x10^{3} & 1.95x10^{-1} & 0.75 & -0.39 & 66.70 & -8.92 \\ -3.95x10^{4} & 1.69x10^{-1} & -8.14x10^{-2} & -4.23x10^{-3} & -8.92 & 3.51x10^{3} \end{bmatrix}$$

$$F^{(a)} = \begin{bmatrix} 0.8666 & 4.8535 & 15.5423 & -3.0467 & 0.0413 & 0.0002 \end{bmatrix}^{T}$$

where the standard convention of extension, transverse shear (chordwise), transverse shear (flapwise), torsion, flapwise bending, and lead-lag bending is used in this sequence.

Appendix 6. Refined ATR-A Root design mass and stiffness matrices (SI unit)

With the baseline material properties (w/o foam):

STIFFNESS_MATRIX : Option 1

$2.49\,x10^{7}$	$2.27\,x10^{2}$	$6.08\,x10^{3}$	$-1.29\,x10^{3}$	$-6.55\,x10^{3}$	$-4.91\,x10^{4}$
$2.27\,x10^{2}$	$7.86\,x10^{6}$	$1.06\,x10^{3}$	$-1.74\,x10^{3}$	$5.82\,x10^{2}$	11.5
$6.08\,x10^{3}$	$1.06\,x10^{3}$	$1.13\,x10^{5}$	$-1.32\,x10^{3}$	-5.29	-32.7
$-1.29\,x10^{3}$	$-1.74\,x10^{3}$	$-1.32\,x10^{3}$	$2.15\,x10^{2}$	2.27E-01	-3.42
$-6.55\,x10^{3}$	$5.82\,x10^{2}$	-5.29	2.27E-01	$3.05\,x10^{2}$	15.3
$-4.91\,x10^{4}$	11.5	-32.7	-3.42	15.3	$6.76\,x10^{3}$

MASS_MATRIX (w/o ballast weight): Option 1

$7.77\,x10^{-1}$	0.0	0.0	0.0	$-2.08\,x10^{-4}$	$-1.43\,x10^{-3}$
0.0	$7.77\,x10^{-1}$	0.0	$-2.08\,x10^{-4}$	0.0	0.0
0.0	0.0	$7.77\,x10^{-1}$	$-1.43\,x10^{-3}$	0.0	0.0
0.0	$-2.08\,x10^{-4}$	$-1.43\,x10^{-3}$	$2.25\,x10^{-4}$	0.0	0.0
$-2.08\,x10^{-4}$	0.0	0.0	0.0	$1.03\,x10^{-5}$	$3.69\,x10^{-7}$
$-1.43\,x10^{-3}$	0.0	0.0	0.0	$3.69\,x10^{-7}$	$2.14\,x10^{-4}$

With the commercially available material properties (w/o foam):

STIFFNESS_MATRIX : Option 1

$2.82\,x10^{7}$	$1.30\,x10^{2}$	$7.42\,x10^{3}$	$-1.48\,x10^{3}$	$-7.42\,x10^{3}$	$-5.43\,x10^{4}$
$1.30\,x10^{2}$	$8.83\,x10^{6}$	$6.61\,x10^{3}$	$-2.07\,x10^{3}$	$6.64\,x10^{2}$	11.1
$7.42\,x10^{3}$	$6.61\,x10^{3}$	$1.19\,x10^{5}$	$-1.59\,x10^{3}$	-5.7629	-35.9
$-1.48\,x10^{3}$	$-2.07\,x10^{3}$	$-1.59\,x10^{3}$	$2.32\,x10^{2}$	2.43E-01	-4.52
$-7.42\,x10^{3}$	$6.64\,x10^{2}$	-5.7629	2.43E-01	$3.45\,x10^{2}$	15.3
$-5.43\,x10^{4}$	11.1	-35.9	-4.52	15.3	$7.67\,x10^{3}$

MASS_MATRIX (Before implementing ballast weight): Option 1

$7.79\,x10^{-1}$	0.0	0.0	0.0	$-2.09\,x10^{-4}$	$-1.3943\,x10^{-3}$
0.0	$7.79\,x10^{-1}$	0.0	$2.09\,x10^{-4}$	0.0	0.0
0.0	0.0	$7.79\,x10^{-1}$	$1.39\,x10^{-3}$	0.0	0.0
0.0	$2.09\,x10^{-4}$	$1.39\,x10^{-3}$	$2.25\,x10^{-4}$	0.0	0.0
$-2.09\,x10^{-4}$	0.0	0.0	0.0	$1.03\,x10^{-5}$	$3.59\,x10^{-7}$
$-1.39\,x10^{-3}$	0.0	0.0	0.0	$3.59\,x10^{-7}$	$2.15\,x10^{-4}$

Appendix 7. Refined ATR-A Tip layup mass and stiffness matrices (SI unit)

With the baseline material properties (w/o foam):

STIFFNESS_MATRIX

$1.40\,x10^{6}$	0.0	0.0	0.0	$-5.36\,x10^{2}$	$-3.03\,x10^{4}$
0.0	2.38E+05	$8.41\,x10^{2}$	-74.6	0.0	0.0
0.0	$8.41\,x10^{2}$	$1.39\,x10^{4}$	$1.32\,x10^{2}$	0.0	0.0
0.0	-74.6	$1.32\,x10^{2}$	20.7	0.0	0.0
$-5.36\,x10^{2}$	0.0	0.0	0.0	30.5	11.6
$-3.03\,x10^{4}$	0.0	0.0	0.0	11.6	$2.01\,x10^{3}$

MASS_MATRIX (Before implementing ballast weight)

$1.24\,x10^{-1}$	0.0	0.0	0.0	$-4.76\,x10^{-5}$	$-2.69\,x10^{-3}$
0.0	$1.24\,x10^{-1}$	0.0	$4.76\,x10^{-5}$	0.0	0.0
0.0	0.0	$1.24\,x10^{-1}$	$2.69\,x10^{-3}$	0.0	0.0
0.0	$4.76\,x10^{-5}$	$2.69\,x10^{-3}$	$1.81\,x10^{-4}$	0.0	0.0
$-4.76\,x10^{-5}$	0.0	0.0	0.0	$2.71\,x10^{-6}$	$1.03\,x10^{-6}$
$-2.69\,x10^{-3}$	0.0	0.0	0.0	$1.03\,x10^{-6}$	$1.78\,x10^{-4}$

MASS_MATRIX (After implementing ballast weight)

$4.11\,x10^{-1}$	0.0	0.0	0.0	$-9.43\,x10^{-5}$	$3.42\,x10^{-3}$
0.0	$4.11\,x10^{-1}$	0.0	$9.43\,x10^{-5}$	0.0	0.0
0.0	0.0	$4.11\,x10^{-1}$	$-3.42\,x10^{-3}$	0.0	0.0
0.0	$9.43\,x10^{-5}$	$-3.42\,x10^{-3}$	$3.12\,x10^{-4}$	0.0	0.0
$-9.43\,x10^{-5}$	0.0	0.0	0.0	$2.71\,x10^{-6}$	$-7.85\,x10^{-7}$
$3.42\,x10^{-3}$	0.0	0.0	0.0	$-7.85\,x10^{-7}$	$3.09\,x10^{-4}$

With the commercially available material properties (w/o foam):

STIFFNESS_MATRIX

$1.40\,x10^{6}$	0.0	0.0	0.0	$-5.36\,x10^{2}$	$-3.03\,x10^{4}$
0.0	2.38E+05	$8.41\,x10^{2}$	-74.6	0.0	0.0
0.0	$8.41\,x10^{2}$	$1.39\,x10^{4}$	$1.32\,x10^{2}$	0.0	0.0
0.0	-74.6	$1.32\,x10^{2}$	20.7	0.0	0.0
$-5.36\,x10^{2}$	0.0	0.0	0.0	30.5	11.6
$-3.03\,x10^{4}$	0.0	0.0	0.0	11.6	$2.01\,x10^{3}$

MASS_MATRIX (Before implementing ballast weight)

$1.24\ x10^{-1}$	0.0	0.0	0.0	$-4.76\ x10^{-5}$	$-2.69\ x10^{-3}$
0.0	$1.24\ x10^{-1}$	0.0	$4.76\ x10^{-5}$	0.0	0.0
0.0	0.0	$1.24\ x10^{-1}$	$2.69\ x10^{-3}$	0.0	0.0
0.0	$4.76\ x10^{-5}$	$2.69\ x10^{-3}$	$1.81\ x10^{-4}$	0.0	0.0
$-4.76\ x10^{-5}$	0.0	0.0	0.0	$2.71\ x10^{-6}$	$1.03\ x10^{-6}$
$-2.69\ x10^{-3}$	0.0	0.0	0.0	$1.03\ x10^{-6}$	$1.78\ x10^{-4}$

MASS_MATRIX (After implementing ballast weight)

$4.11\ x10^{-1}$	0.0	0.0	0.0	$-9.43\ x10^{-5}$	$3.42\ x10^{-3}$
0.0	$4.11\ x10^{-1}$	0.0	$9.43\ x10^{-5}$	0.0	0.0
0.0	0.0	$4.11\ x10^{-1}$	$-3.42\ x10^{-3}$	0.0	0.0
0.0	$9.43\ x10^{-5}$	$-3.42\ x10^{-3}$	$3.12\ x10^{-4}$	0.0	0.0
$-9.43\ x10^{-5}$	0.0	0.0	0.0	$2.71\ x10^{-6}$	$-7.85\ x10^{-7}$
$3.42\ x10^{-3}$	0.0	0.0	0.0	$-7.85\ x10^{-7}$	$3.09\ x10^{-4}$

BIBLIOGRAPHY

Aoyama, T., C. Yang, N. Kondo and S. Saito (2006). Comparison of Noise Reduction Effect between Afc and Conventional Ibc by Moving Overlapped Grid Method. 12th AIAA/CEAS Aeroacoustics Conference (27th AIAA Aeroacoustics Conference), Cambridge, MA.

Barrett, R. M. (1990). Intelligent Rotor Blade and Structures Development Using Directionally Attached Piezoelectric Crystals College park, The University of Maryland **Master of Science**.

Bauchau, O. A. (1998). "Computational Schemes for Flexible Nonlinear Multi-Body Systems." Multibody System Dynamics **2**: pp. 169–225.

Bauchau, O. A. (2008). "Review of Contemporary Approaches for Constraint Enforcement in Multibody Systems." Journal of Computational and Nonlinear Dynamics **3**(1): 011005-1-8.

Bent, A. A. and N. W. Hagood (1997). "Piezoelectric Fiber Composites with Interdigitated Electrodes." Journal of Intelligent Material Systems and Structures **8**(11): 903-919.

Bent, A. A., N. W. Hagood and J. P. Rodgers (1995). "Anisotropic Actuation with Piezoelectric Fiber Composites." Journal of Intelligent Material Systems and Structures **6**(3): 338-349.

Bernhard, A. P. F. and J. Wong (2003). Sikorsky Active Rotor Control Evaluation of Nasa/Army/Mit Active Twist Rotor. American Helicopter Society Society 59th Annual Forum, Phoenix, AR.

Booth, E. R. and M. L. Wilbur (2004). "Acoustic Aspects of Active-Twist Rotor Control." Journal of the American Helicopter Society **49**(1): 3-10.

Brockmann, T. H. and R. Lammering (2006). "Beam Finite Elements for Rotating Piezoelectric Fiber Composite Structures." Journal Of Intelligent Material Systems and Structures(5): 431.

Brown, E. L. (2003). Integrated Strain Actuation in Aircraft with Highly Flexible Composite Wings. Cambridge, MA, Massachusetts Institute of Technology. **Doctor of Philosophy**.

Celi, R. (1999). "Recent Applications of Design Optimization to Rotorcraft - a Survey." Journal of Aircraft **36**(1): 176-189.

Centolanza, L. R. (2002). "Induced-Shear Piezoelectric Actuators for Active Twist Rotor Blades." Collection of Technical Papers - AIAA/ASME/ASCE/AHS/ASC Structures, Structural Dynamics and Materials Conference **3**: 1977-1987.

Cesnik, C. E. S., J. Mok, J. A. Morillo and A. S. Parikh (2005). Design Optimization of Active Twist Rotor Blades. 30th European Rotorcraft Forum, Marseilles, France.

Cesnik, C. E. S., J. Mok, A. S. Parikh and S. Shin (2004). Optimum Design Framework for Integrally Twisted Helicopter Blades 45th AIAA/ASME/ASCE/AHS/ASC

Structures, Structural Dynamics and Materials Conference, Palm Springs, California.

Cesnik, C. E. S. and R. Palacios (2003). Modeling Piezocomposite Actuators Embedded in Slender Structures. AIAA/ASME/ASCE/AHS/ASC 44th Structures, Structural Dynamics and Materials Conference- Adaptive Structures, Norfolk, VA.

Cesnik, C. E. S., R. S. Park and R. Palacios (2003). "Effective Cross-Section Distribution of Anisotropic Piezocomposite Actuators for Wing Twist." Smart Structures and Materials 2003: Smart Structures and Integrated Systems **5056**: 21-32.

Cesnik, C. E. S., S.-J. Shin, W. K. Wilkie, M. L. Wilbur and P. H. Mirick (1999). Modeling, Design, and Testing of the Nasa/Army/Mit Active Twist Rotor Prototype Blade. American Helicopter Society 55th Annual Forum, Montreal, Canada

Cesnik, C. E. S. and S. Shin (2001). "On the Modeling of Integrally Actuated Helicopter Blades." International Journal of Solids and Structures **38**(10-13): 1765-1789.

Cesnik, C. E. S. and S. J. Shin (2001). "On the Twist Performance of a Multiple-Cell Active Helicopter Blade." Smart Materials & Structures **10**(1): 53-61.

Cesnik, C. E. S., S. J. Shin and M. L. Wilbur (2001). "Dynamic Response of Active Twist Rotor Blades." Smart Materials & Structures **10**(1): 62-76.

Chen, P. C. and I. Chopra (1996). "Induced Strain Actuation of Composite Beams and Rotor Blades with Embedded Piezoceramic Elements." Smart Materials and Structures(1): 35.

Chopra, I. (2000). "Status of Application of Smart Structures Technology to Rotorcraft Systems." Journal of the American Helicopter Society **45**(4): 228-252.

Chopra, I. (2002). "Review of State of Art of Smart Structures and Integrated Systems." Aiaa Journal **40**(11): 2145-2187.

Cribbs, R. C. and P. P. Friedmann (2001). Actuator Saturation and Its Influence on Vibration Reduction by Actively Controlled Flaps. 42nd AIAA/ASME/ASCE/AHS/ASC Structures, Structural Dynamics, and Materials Conference, Reston, VA.

Davis, M. W. and W. H. Wellert (1991). "Helicopter Rotor Dynamics Optimization with Experimental Verification." Journal of Aircraft **28**(1): 38-48.

Depailler, G. and P. P. Friedmann (2002). Reduction of Vibrations Due to Dynamic Stall in Helicopters Using an Actively Controlled Flap. 43rd AIAA/ASME/ASCE/AHS/ASC Structures, Structural Dynamics, and Materials Conference, Denver, Colorado.

Fletcher, R. and M. J. D. Powell (1963). "A Rapidly Convergent Descent Method for Minimization." Journal of Computational and Nonlinear Dynamics **6**: pp. 163-168.

Friedmann, P. P. (1977). "Recent Developments in Rotary-Wing Aeroelasticity." Journal of Aircraft **14**(11): 1027-1041.

Friedmann, P. P. (1987). "Recent Trends in Rotary-Wing Aeroelasticity." Vertica **11**(1-2): 139-170.

Friedmann, P. P. (1990). "Helicopter Rotor Dynamics and Aeroelasticity - Some Key Ideas and Insights." Vertica **14**(1): 101-121.

Friedmann, P. P. (1991). "Helicopter Vibration Reduction Using Structural Optimization with Aeroelastic Multidisciplinary Constraints - a Survey." Journal of Aircraft **28**(1): 8-21.

Friedmann, P. P. (1999). "Renaissance of Aeroelasticity and Its Future." Journal of Aircraft

36(1): 105-121.

Friedmann, P. P. (2004). "Rotary-Wing Aeroelasticity: Current Status and Future Trends." AIAA Journal **42**(10): 1953-1972.

Friedmann, P. P., G. P. Carman and T. A. Millott (2001). "Magnetostrictively Actuated Control Flaps for Vibration Reduction in Helicopter Rotors - Design Considerations for Implementation." Mathematical and Computer Modelling **33**(10-11): 1203-1217.

Friedmann, P. P. and D. H. Hodges (2003). "Rotary Wing Aeroelasticity - a Historical Perspective." Journal of Aircraft **40**(6): 1019-1046.

Friedmann, P. P. and T. A. Millott (1995). "Vibration Reduction in Rotorcraft Using Active Control - a Comparison of Various Approaches." Journal of Guidance Control and Dynamics **18**(4): 664-673.

Friedmann, P. P. and P. Shanthakumaran (1984). "Optimum Design of Rotor Blades for Vibration Reduction in Forward Flight." Journal of the American Helicopter Society **29**(4): 70-90.

Friedmann, P. P., C. Venkatesan and K. Yuan (1992). Development of a Structural Optimization Capability for the Aeroelastic Tailoring of Composite Rotor Blades with Straight and Swept Tips. 4th AIAA/USAF/NASA/OAI Symposium on Multidisciplinary Analysis and Optimization, Cleveland, OH.

Fulton, M. and R. A. Ormiston (1998). Small-Scale Rotor Experiments with on-Blade Elevons to Reduce Blade Vibratory Loads in Forward Flight. Proceedings of the 54th Annual Forum of the American Helicopter Society, Alexandria, VA.

Ganguli, R. (2004). "Survey of Recent Developments in Rotorcraft Design Optimization." Journal of Aircraft **41**(3): 493-510.

Glaz, B. (2008). Active/Passive Optimization of Helicopter Rotor Blades for Improved Vibration, Noise, and Performance Characteristics. Aerospace Engineering, University of Michigan. **Doctor of Philosophy**.

Glaz, B., P. P. Friedmann and L. Lui (2006). Surrogate Based Optimization of Helicopter Rotor Blades for Vibration Reduction in Forward Flight. 47th AIAA/ASME/ASCE/AHS/ASC Structures, Structural Dynamics, and Materials Conference, Newport, Rhode Island.

Glukhikh, S., E. Barkanov, A. Kovalev, P. Masarati, M. Morandini, J. Riemenschneider and P. Wierach (2008). "Design of Helicopter Rotor Blades with Actuators Made of a Piezomacrofiber Composite." Mechanics of Composite Materials **44**(1): 57-64.

Grohmann, B. A., C. Maucher, T. Prunhuber, P. Jänker, O. Dieterich, B. Enenkl, M. Bauer, E. Ahci, A. Altmikus and H. Baier (2008). "Multidisciplinary Design and Optimization of Active Trailing Edge for Smart Helicopter Rotor Blade." Mechanics of Advanced Materials and Structures **15**(3): 307-324.

Hafka, R. T. and Z. Gurdal (1992). Elements of Structural Optimization, Kluwer Academic Publishers.

Hoffmann, F., S. Opitz and J. Riemenschneider (2009). Validation of Active Twist Modeling Based on Whirl Tower Tests. American Helicopter Society 65th Annual Forum, Grapevine, Texas, USA.

Hooper, W. E. (1984). " Vibratatory Airloading of Helicopter Rotors." Vertica **8**(2): 73–92.

Johnson, W. (1992-1997). Camrad. CAMRAD II, Comprehensive Analytical Model of Rotorcraft Aerodynamics and Dynamics. W. Johnson. Palo Alto, California, Johnson Aeronautics.

Jones, R. M. (1999). Mechanics of Composite Materials, Taylor & Francis

Kovalovs, A., E. Barkanov and S. Gluhihs (2007). "Active Twist of Model Rotor Blades with D-Spar Design " Transport. Vilnius: Technika **22**(1): 38-44.

Lemos, R. (2007). The Helicopter: A Hundred Years of Hovering.

Lim, J. w. and I. Chopra (1991). "Aeroelastic Optimization of a Helicopter Rotor." Journal of Aircraft **28**(1): 29-37.

Milgram, J. and I. Chopra (1998). "A Parametric Design Study for Actively Controlledtrailing Edge Flaps." Journal of the American Helicopter Society **43**(2): 110-119.

Millott, T. A. and P. P. Friedmann. (1994). Vibration Reduction in Helicopter Rotors

Using an Actively Controlled Partial Span Trailing Edge Flap Located on the Blade. NASA-CR-4611.

Monner, H. P., S. Opitz, J. Riemenschneider and P. Wierach (2008). Evolution of Active Twist Rotor Designs at Dlr. 49th AIAA/ASME/ASCE/AHS/ASC Structures, Structural Dynamics, and Materials Conference, Schaumburg, IL.

MSCSoftware (2004). Patran. Santa Ana, CA.

Palacios Nieto, R. (2005). Asymptotic Models of Integrally-Strained Slender Structures for High-Fidelity Nonlinear Aeroelastic Analysis. Aerospace Engineering. Ann Arbor, University of Michigan. **Doctor of Philosophy**.

Pape, A. L. and P. Beaumier (2005). "Numerical Optimization of Helicopter Rotor Aerodynamic Performance in Hover." Aerospace Science and Technology **9**: 191-201.

Philippe, J.-J. (2003). "Rotorcraft Challenges and Associated French-German Research Contributions." AIAA/ICAS International Air and Space Symposium and Exposition: The Next 100 Years; Dayton, OH; July 14-17, 2003.

Prahlad, H. and I. Chopra (2007). "Modeling and Experimental Characterization of Sma Torsional Actuators." Journal of Intelligent Material Systems and Structures **18**(1): 29-38.

Prechtl, E. F. (2000). Design and Implementation of a Piezoelectric Servoflap Actuation System for Helicopter Roror Individual Blade Control. Aeronautics and Astronautics, Massachusetts Institute of Technology. **Doctor of Philosophy**.

Rodgers, J. P. (1999). Development of an Integral Twist-Actuated Rotor Blade for Individual Blade Control. Aeronautics and Astronautics, Massachusetts Institute of Technology. **Doctor of Philosophy**.

Rodgers, J. P. and N. W. Hagood (1998). Preliminary Mach-Scale Hover Testing of an Integral Twist-Actuated Rotor Blade, SPIE.

Sanders, B. (2004). "Defense Advanced Research Projects Agency - Smart Materials and Structures Demonstration Program Overview." Journal of Intelligent Material Systems and Structures **15**(4): 227-233.

Sekula, M. K. (2005). "A Parametric Study of the Structural Design for an Advanced Active

Twist Rotor." Annual forum proceedings. **1**: 95.

Shaw, J., N. Albion, E. J. Hanker Jr. and R. S. Teal (1989). "Higher Harmonic Control: Wind Tunnel Demonstration of Fully Effective Vibratory Hub Force Suppression " Journal of the American Helicopter Society Jan 1989 1 14-25 34 **1**.

Shin, S., C. Cesnik and M. L. Wilbur (2000). Dynamic Response of Active Twist Rotor Blade. AIAA/ASME/AHS Adaptive Structures Forum, Atlanta, Georgia.

Shin, S. and C. E. S. Cesnik (1999). Design, Manufacturing and Testing of an Active Twist Rotor, Active Materials and Structures Laboratory, AMSL Report #99-3, Massachusetts Institute of Technology.

Shin, S. and C. E. S. Cesnik (2007). "Helicopter Vibration Reduction in Forward Flight Using Blade Integral Twist Actuation." Journal of Mechanical Science and Technology **21**(2): 251-263.

Shin, S., C. E. S. Cesnik and S. R. Hall (2005). "Closed-Loop Control Test of the Nasa/Army/Mit Active Twist Rotor for Vibration Reduction." Journal of the American Helicopter Society **50**(2): 178-194.

Shin, S., C. E. S. Cesnik and S. R. Hall (2007). "Design and Simulation of Integral Twist Control for Helicopter Vibration Reduction." International Journal of Control Automation and Systems **5**(1): 24-34.

Shin, S. J. (1999). Design Manufacturing and Testing of an Active Twist Rotor. Aeronautics and Astronautics, Massachusetts Institute of Technology. **Master of Science**.

Shin, S. J., C. E. S. Cesnik and S. R. Hall (2005). "System Identification Technique for Active Helicopter Rotors." Journal of Intelligent Material Systems and Structures **16**(11-12): 1025-1038.

Shin, S. J., C. E. S. Cesnik, W. K. Wilkie and M. L. Wilbur (2008). "Design and Manufacturing of a Model-Scale Active Twist Rotor Prototype Blade." Journal of Intelligent Material Systems and Structures **19**(12): 1443-1456.

Viswamurthy, S. R. and R. Ganguli (2004). "An Optimization Approach to Vibration Reduction in Helicopter Rotors with Multiple Active Trailing Edge Flaps." Aerospace Science and Technology **8**: 185-194.

Wickramasinghe, V. K. and N. W. Hagood (2004). "Durability Characterization of Active Fiber Composite Actuators for Helicopter Rotor Blade Applications." Journal of Aircraft **41**(4): 931-937.

Wierach, P., J. Riemenschneider and S. Keye (2005). Development of an Active Twist Rotor Blade with Distributed Actuation and Orthotropic Material, SPIE.

Wilbur, M. L., P. H. Mirick, W. T. Yeager, C. W. Langston, C. E. S. Cesnik and S. Shin (2002). "Vibratory Loads Reduction Testing of the Nasa/Army/Mit Active Twist Rotor." Journal of the American Helicopter Society **47**(2): 123-133.

Wilbur, M. L., P. H. Mirick, W. T. J. Yeager, C. W. Langston, C. E. S. Cesnik and S. J. Shin (2001). Vibratory Loads Reduction Testing of the Nasa/Army/Mit Active Twist Rotor. American Helicopter Society 57th Annual Forum, Washington, D. C.

Wilbur, M. L., W. T. Yeager, Jr. and M. K. Sekula (2001). Further Examination of the Vibratory Loads Reduction Results from the Nasa/Army/Mit Active Twist Rotor. American Helicopter Society 58th Annual Forum, Montréal, Canada.

Wilkie, W. K. (1997). Anisotropic Piezoelectric Twist Actuation of Helicopter Rotor Blades: Aeroelastic Analysis and Design Optimization. Department of Aerospace Engineering Sciences, University of Colorado. **Doctor of Philosophy**.

Wilkie, W. K., R. G. Bryant, J. W. High, R. L. Fox, R. F. Hellbaum, J. Antony Jalink, B. D. Little and P. H. Mirick (2000). Low-Cost Piezocomposite Actuator for Structural Control Applications. SPIE's 7th Annual International Symposium on Smart Structures and Materials, Newport Beach, CA,.

Wilkie, W. K., M. L. Wilbur, P. H. Mirick, C. E. S. Cesnik and S. J. Shin (1999). Aeroelastic Analysis of the Nasa/Army/Mit Active Twist Rotor. American Helicopter Society 55th Annual Forum, Montreal, Canada.

Williams, R. B., D. J. Inman and W. K. Wilkie (2004). "Temperature-Dependent Thermoelastic Properties for Macro Fiber Composite Actuators." Journal of Thermal Stresses **27**(10): 903-915.

Williams, R. B., D. J. Inman and W. K. Wilkie (2006). "Nonlinear Response of the Macro Fiber Composite Actuator to Monotonically Increasing Excitation Voltage." Journal of Intelligent Material Systems and Structures **17**(7): 601-608.

Young, D. K. and F. J. Tarzanin (1993). "Structural Optimization and Mach Scale Test Validation of a Low Vibration Rotor." Journal of the American Helicopter Society **38**(3): 83-92.